Abrupt Changes in the Tunneling Levels for Mn$_{12}$-tBuAc

Eduardo H. da Silva Neto

Advisor: Jonathan R. Friedman
May 8, 2008

Submitted to the
Department of Physics
of Amherst College
in partial fulfillment of the requirements
for the degree of
Bachelor of Arts with Honors

Abstract

Abrupt Changes in the Tunneling Levels for Mn12-tBuAc Induced by a

Transverse Magnetic Field

Faculty Advisor: Professor Jonathan R. Friedman

This thesis investigates the magnetic dynamics of the high symmetry SMM Mn_{12}-tBuAc. The core of this molecule has an arrangement of twelve Manganese magnetic ions giving the molecule a total (giant) spin of 10. This SMM has a large uniaxial anisotropy between the $m = +10$ and $m = -10$ eigenstates of the S_z spin operator. The spin can reverse direction by rotating from up ($m = +10$) to down ($m = -10$) if it has enough thermal activation to "climb" over the anisotropy barrier. But at low enough temperatures this classical relaxation behavior will be suppressed in favor of a semi-classical phenomenon called thermally assisted tunneling of magnetization. In particular, this research investigates the longitudinal- and transverse-field dependences of the magnetic relaxation rate for Mn_{12}-tBuAc. We interpret our results as evidence that the dominant levels for thermally assisted resonant tunneling change abruptly as the applied transverse field is increased.

Acknowledgements

Thanks to Jonathan Friedman for always being available and willing to teach. When things in my life did not go the right way, I could always count on having something to do in the lab, or some physics to discuss with Professor Friedman. These things always cheered me up. Thanks for always trusting your students. It is this trust that leads to extra motivation in the lab. He is a great mentor and a friend for life. Jonathan will win all the big prizes one day[1].

I would like to thank the physics department at Amherst College. It has been a lot of fun to be in a department where faculty, staff and students interact not only academically, but outside the department as well. Amongst the students, I would especially like to thank Sarang Gopalakrishnan and Mike Foss-Feig who were "inspirational" figures to susceptible underclassmen like I once was. I would also like to thank Dan Guest, Alex Bridges and D.K. with whom I had many conversations about physics. A lot can be learned through interactions with other students. And thanks to Jagu for his good advice and warm friendship.

---

[1]I hear Stockholm is a beautiful place!

I feel like I have many advisors[2]. Additional thanks to Professors Larry Hunter, William Loinaz, Norton Starr, and Rob Benedetto for being great teachers and good friends.

I would also like to acknowledge the collaboration with George Christou's group at the Chemistry department in the University of Florida, especially Christos Lampropoulos who was always quick to provide us with the, always nicely grown, Mn_{12}-tBuAc crystals that we use in the experiments. And, also, Eli Zeldov, N. Avraham, Y. Myasoedov, H. Shtrikman at Weizmann Institute of Science in Israel, for providing us the Hall sensors, which are the essential magnetometers used in this research.

A lot of experiments required the always prompt and willing assistance of staff members. Most notably Bob Bartos, who keeps everything running and our liquid nitrogen always available. Thanks to Dan Krause and Bob Cann for all the help and insight in the machine shop, and Norman Page and Phil Grant for sharing their expertise in electronics.

I spent the last three years working in the Friedman laboratories, where I learned to enjoy experimental physics. It has been a great ride. Special thanks to Jim Atkinson, for helping out in the lab and for the company. I was also very fortunate to have worked with Dr. Mustafa Bal. It was always fun to have company when working overnight. Mustafa is very tenacious. I often tried to beat him by being the last one to leave the lab; good thing I did not keep scores.

Thanks to all my friends who were always very supportive, especially Ira Yeung who has been my writing buddy through the many nights it took to

―――――――――――――――――――――

[2]Officially I've had five.

finish this thesis. And thanks to Patricia and Ben Schneider for living so close to Amherst, Maria Emília for the emotional support, and my parents, Eduardo and Zélia, who have always pushed me forward in my academic endeavors.

I have enjoyed working with Molecular Magnets for the past three years. As with many problems in physics, a complete of understanding of the relaxation dynamics has not been achieved. However, trying to understand dynamical processes where the interplay between *Quantum Mechanics* and *Statistical Mechanics* is crucial, can sometimes be very rewarding; I hope the reader will agree.

Contents

Chapter 1

Introduction

Some of the predictions of Quantum Mechanics are often presented to the general public as counterintuitive, strange and sometimes philosophically unsound. However, any doubts about the validity of the theory are overpowered by the immense body of experiments that confirm it, such as tests of Bell's inequalities. Although most problems are rarely solved analytically, perturbation theory and other approximation methods give a quantitative explanation of most phenomena in the microscopic scale.

In the *Schröndinger Cat* paradox the animal is found in a superposition of macroscopic states. The cat is a macroscopic *object* that contains a macroscopic *degree of freedom* (its own life) and this degree of freedom can be in a quantum mechanical superposition of *macroscopically distinct states* (dead or alive). In the spirit of the original intentions of Schröndinger we must remark that we do not observe macroscopic objects in a superposition of macroscopically distinct states. This is frustrating since it should be expected that, if macroscopic objects are just a large collection of microscopic particles, a theory that explains microscopic phenomena should fully explain the macroscopic.

As a self assessment I would ask the reader to categorize the phenomena of alpha particle emissions by heavy nuclei and the mechanics of a heat engine. These two should clearly fall under the microscopic and macroscopic labels respectively. But our understanding of phenomena that occur, not when a single particle shows quantum behavior, but instead a large ensemble of them do, still requires further investigation.

There has been a large commitment by physicists over the past few decades to experiment with systems that show both quantum mechanical and macroscopic characteristics. There are many approaches to produce these kinds of systems, but in essence most of them will fall under two categories, as explained by Friedman in [2]. One way is to start with a macroscopic system and shrink it to smaller scales until the system behaves quantum mechanically (in a *top-down* fashion). Another way is to start with a microscopic system displaying quantum behavior and then either enlarge the system until macroscopic degrees of freedom can be measured or to put together an ensemble of these microscopic systems until the whole ensemble displays macroscopic degrees of freedom (in a *bottom-up* approach). Molecular Magnets fall under this latter category, where the magnetization represents the macroscopic degree of freedom.

In this thesis I will describe the experiments we have performed on the Molecular Magnet Mn_{12}-tBuAc. In particular, we have studied the magnetic field dependence of its relaxation rate of magnetization. Most of the data that will be discussed in later chapters was collected during the summer and fall of 2007. After this productive period we have encountered several technical problems that prevented further measurements. Although we had a qualitative understanding of the main features of the data, it became clear that we needed

a more detailed understanding of the dynamics that controls the relaxation of the magnetization for Mn$_{12}$-tBuAc. This ignited a new phase of this project, where we performed detailed simulations of the relaxation dynamics.

The primary motivation for the experiments, and later theoretical calculations, has been to understand how the phenomenon of transverse-field-induced barrier reduction can change the relaxation dynamics of magnetization in a single-molecule magnet. In this first chapter I will give a brief introduction of molecular magnets, citing key experimental results that attracted attention to the field since the mid-nineties. And, I will also present the Hamiltonian for Mn$_{12}$-tBuAc in a constructive approach, where I will explain the physical interpretation of the terms in the Hamiltonian that will be relevant to this thesis. Since the Schröndinger equation dictates the time evolution of any system in quantum mechanics, understanding the Hamiltonian is a key step toward a better comprehension of the dynamics of the system of interest.

1.1   Molecular Magnets

Molecular magnets are, as the name suggests, molecules that have a nonzero magnetic moment. If these molecules are constructed out of magnetic ions, then the entire molecule should behave as a little magnetic domain or as a single *nanometer* size magnet. The term single-molecule magnet (SMM) has become the canonical term to describe molecules that fall under the description in the last sentence. In this thesis I will discuss experiments and results that were done on the SMM $[Mn_{12}O_{12}(O_2CCH_2Bu^t)_{16}(CH_3OH)_4] \cdot CH_3OH$, Mn$_{12}$-tBuAc for short [3, 4]. This SMM is a variant of the more well known $[Mn_{12}O_{12}(O_2CCH_3)_{16}(H_2O)_4] \cdot 2CH_3CO_2H \cdot 4H_2O$, Mn$_{12}$-Ac for short, molec-

ular magnet (see Fig. 1.1) which is the most studied SMM of the last fifteen years. Because both SMMs share most of their characteristics, it is only natural to begin a discussion of Mn_{12}-Ac. In the next section I will address these shared characteristics and for simplicity, I will, at some points, refer to both Mn_{12}-Ac and Mn_{12}-tBuAc as Mn_{12}, while keeping the distinction when appropriate.
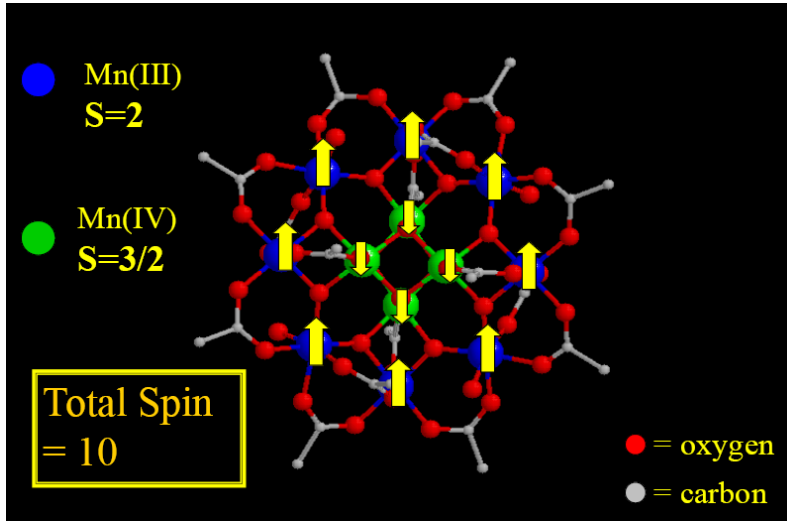
Figure 1.1: The Mn_{12}-Ac Molecule. Reproduced by permission of R. Sessoli.

1.1.1 The Mn_{12} SMM

The compound Mn_{12}-Ac was first synthesized by Lis [5] in 1980. The ionic core of Mn_{12} is composed of four Mn^{4+} ions with spin S= 3/2 in a tetrahedron surrounded by eight Mn^{3+} ions with spin S= 2 in a non-coplanar ring. At low enough temperatures, the coupling between the Mn ions is strong enough to preserve the molecular structure, therefore giving rise to a *giant spin*[1] $S = 10$

_____

[1]For Mn_{12} g is approximately 2. It will be left to the reader to decide if a magnetic moment of $2 \times 10\mu_B = 20\mu_B$ is macroscopic enough for the *giant spin* term to be applicable.

system. This spin allows for 21 quantized orientations of the projection of the spin along the z-axis ($-10 \leq m \leq +10$). In the absence of any external magnetic fields the system is characterized by a large anisotropy between the $m = -10$ and $m = +10$ states, which, by convention, will be referred to as the *down* and *up* orientations. So the simplest Hamiltonian for the system would be given by:

$$\mathcal{H}_A = -DS_z^2, \tag{1.1}$$

where $D \approx 0.548K$ [6]. This results in a anisotropy barrier between the $m = \pm 10$ states of approximately $(S^2 - 0^2) \times 0.548 \approx 55\ K$. A potential diagram versus the polar angle (angle between the spin and the z-axis) yields a double-well structure and can be seen in Fig. 1.2, where the lines represent the possible energies for the m states.
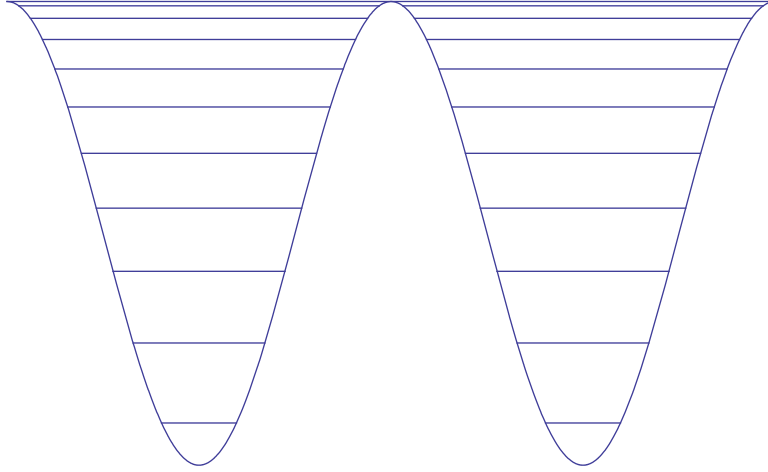

Figure 1.2: Double Well Potential - Schematic representation of the energy levels in Mn_{12} at zero applied magnetic field.

In the Bohr atom, the energy level spacing between adjacent levels decreases dramatically as we move to higher levels (away from the nucleus). The

energy level density is so high far from the nucleus, that the quantization effects of QM are washed away, giving preference to a quasi-continuous energy spectrum. It is, therefore, pertinent to ask under what regimes should the quantization of the energy levels in Mn_{12} be relevant. It is obviously not relevant at room temperature since the anisotropy barrier is of the order of 60 K. A back of the envelope calculation yields an energy spacing of $D \times (S^2 - (S-1)^2)0.55\ K \times (100 - 81) \approx 10.45\ K$ between the ground state and the first excited level. As a rough estimate, it can be said that the quantization of the system is relevant whenever the temperature is in the order of 10 K. Most of the experiments performed on this SMM, including the ones I will describe in this thesis, are performed at temperatures below 10 K.

Notice that, if the system was solely described by Eq. (1.1), then $\mathcal{H}_{\mathcal{A}}$ and S_z would commute and the $|m\rangle$ eigenstates of the S_z operator would be eigenstates of the Hamiltonian. The picture becomes a little more interesting if we add a symmetry breaking term to Eq. (1.1).

$$\mathcal{H}_{\mathcal{A},\mathcal{Z}} = -DS_z^2 - g\mu_B \vec{H} \cdot \vec{S} \tag{1.2}$$

$$= -DS_z^2 - g\mu_B(H_x S_x + H_z S_z) \tag{1.3}$$

In Eq. (1.2) the dot product on the RHS is the Zeeman coupling term. The constant μ_B is the Bohr magneton and $g \approx 2$ [7]. To make the effects of this applied magnetic field evident I have rewritten the RHS in (1.3) assuming that $\vec{H}$ is in the x-z plane. For nonzero H_x the $\mathcal{H}_{\mathcal{A},\mathcal{Z}}$ Hamiltonian does not commute with the S_z operator. Consequently the $|m\rangle$ states no longer form an energy eigenbasis of the system. More on this topic will be addressed in chapter 2.

Evidence for quantum resonant tunneling of the magnetization was first conclusively observed and interpreted by Friedman *et al.* [8] in the form of
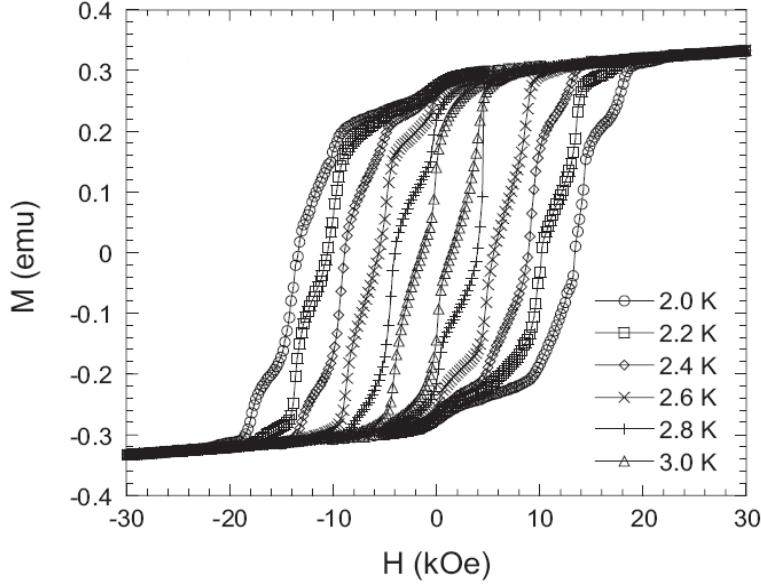
Figure 1.3: Hysteresis for Mn_{12}-Ac. The steps occur for field values (H_z) that are independent of temperature. As the temperature is increased the loops close in on themselves [2, 9]. Reproduced by permission of J.R. Friedman, © 1997 The American Physical Society.

steps in the hysteresis loops of magnetization versus an applied longitudinal-field H_z. The hysteresis curves for Mn_{12}-Ac can be seen in Figure 1.3. The steps in the magnetization occur at equally spaced values of H_z, which are independent of temperature. However, as the temperature is increased, the hysteresis loops close in on themselves. At high enough temperatures, the molecules have enough energy to reverse their spin orientation when the magnetic field changes direction, suggesting that the process of relaxation of magnetization is partially caused by thermal activation.

The steps were interpreted to appear at values of H_z where m levels on opposite wells align, which we will intuitively call the resonance condition; it can be seen schematically in Fig. 1.4. The condition for two levels m and m'

8

to be on resonance is[2]

$$-Dm^2 - g\mu_B H_z m = -Dm'^2 - g\mu_B H_z m'. \qquad (1.4)$$

After some algebraic manipulation, Eq. (1.4) yields

$$H_z = \frac{-D(m+m')}{g\mu_B} = -N\frac{D}{g\mu_B}, \qquad (1.5)$$

where $m + m' = N$ is the resonance. So, for example, the $N = 1$ resonance occurs when $m = \pm 10$ and $m' = \mp 9$ align on opposite wells. Figure 1.4 shows the $N = 4$ resonance. Given the value of D mentioned above, the resonance condition is $H_z \approx N \times 0.45T$, as the reader can verify in Fig. 1.3. I have dropped the minus sign since, for example, the $+9, -10$ resonance condition is analogous to the $-9, +10$ condition and will both be referred to as the $N = 1$ resonance.

For the sake of argument I have neglected an important term to the Hamiltonian of Mn_{12}. This term is a fourth order anisotropy $-BS_z^4$, where $B = 1.17 \times 10^{-3}\ K$ [6]. When resonance is achieved between the $m = -7$ and $m = +9$ levels, for example, other levels will not be on resonance because of the fourth order anisotropy (Fig. 1.5). The resonance condition has to be altered:

$$H_z = -\frac{D(m+m')}{g\mu_B}\left[1 + \frac{B}{D}(m^2 + m'^2)\right]. \qquad (1.6)$$

Where the resonance no longer depends on $N = m + m'$ only, instead, the term inside the square brackets depends on both m and m' independently. I will sometimes ambiguously use the N resonance terminology. Even though the N resonance is split into many resonances, the range of the N resonance

---

[2]The existence of a fourth order anisotropy term, as discussed in the end of this section, will alter this resonance condition. This is, however, a good approximation for understanding the existence of the steps in the hysteresis.
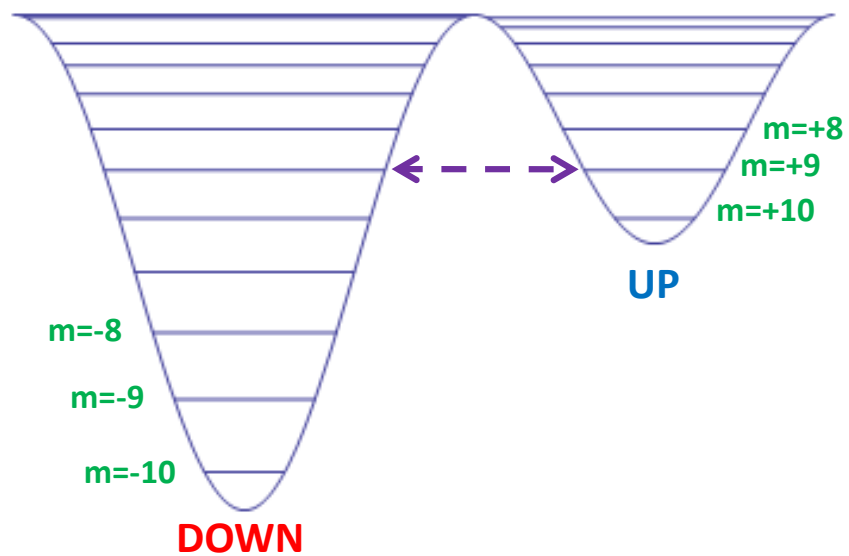
Figure 1.4: Resonance Condition — the $m = -6$ level is aligned with the $m = +10$ level. This is the $N = 4$ resonance.

does not overlap with the range of the $N \pm 1$ resonances, as long as N remains small.
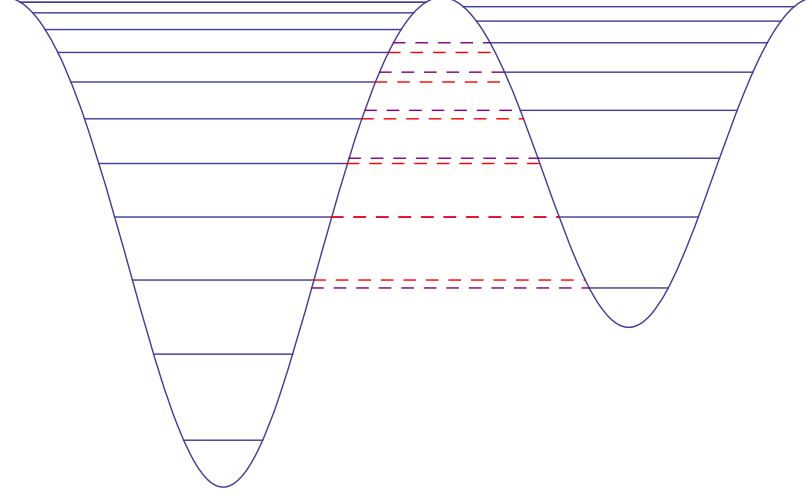
Figure 1.5: Double Well Potential — level $m = +9$ is on-resonance with $m = -7$ but the fourth order anisotropy $(-BS_z^4)$ does not allow more resonances (see dashed lines). Red lines represent energy of the levels on the left well and purple lines represent energy of the levels on the right well.

And, for completeness, I will also mention the existence of a transverse anisotropy term $E(S_x^2 - S_y^2)$ [10, 11, 12]. The full Hamiltonian reads:

$$\mathcal{H}_T = -DS_z^2 - BS_z^4 - g\mu_B\vec{H}\cdot\vec{S} + E(S_x^2 - S_y^2) \ . \tag{1.7}$$

Throughout most of the this thesis, however, I will not take into account effects due to the transverse anisotropy. We will primarily work with the reduced Hamiltonian:

$$\mathcal{H} = -DS_z^2 - BS_z^4 - g\mu_B\vec{H}\cdot\vec{S} \ . \tag{1.8}$$

1.1.2 Differences between Mn$_{12}$-Ac and Mn$_{12}$-tBuAc

The core molecular structure of Mn$_{12}$-tBuAc and Mn$_{12}$-Ac are identical, but the former has much less intermolecular interaction due to a larger separation between molecules. Furthermore, Mn$_{12}$-tBuAc has a a truly axial four-fold symmetry. Cornia *et al.* [13] found that although Mn$_{12}$-Ac has an average four-fold symmetry, it actually contains Mn$_{12}$ molecules in six different forms, depending on the form of its hydrogen bonds (Fig. 1.6 from [13]). Detailed EPR studies showed that Mn$_{12}$-tBuAc has less solvent disorder [3]. Ideally
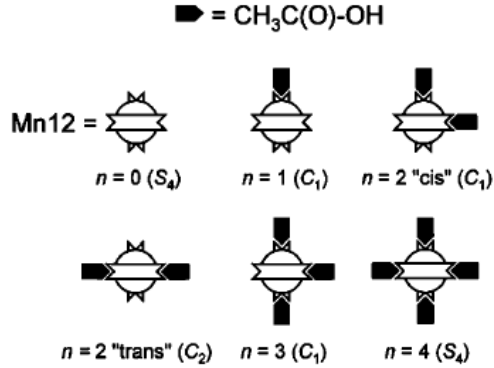
Figure 1.6: Six different isomers of Mn$_{12}$-Ac. Only two have four-fold axial symmetry ($n = 1$ and $n = 4$) [13].

we would like all molecules in a Mn$_{12}$ crystal to have no interaction with each other and, also, all the molecules to share the same z-axis (crystallographic axial symmetry).

In 2006 Wernsdorfer *et al.* [4] performed detailed studies of the hysteresis loops for Mn$_{12}$-tBuAc. At temperatures near the crossover between thermally assisted and pure quantum tunneling they observed a very clear fine structure to the hysteresis loops. A comparison between Mn$_{12}$-tBuAc and Mn$_{12}$-Ac can

be seen in Fig. 1.7[3]. The steps in the fine structure of the hysteresis loops are due to the fourth order anisotropy. Wernsdorfer *et al.* concluded that the increased level of detail they found in the Mn_{12}-tBuAc was only possible because of less disorder in its crystalline structure of Mn_{12}-tBuAc.
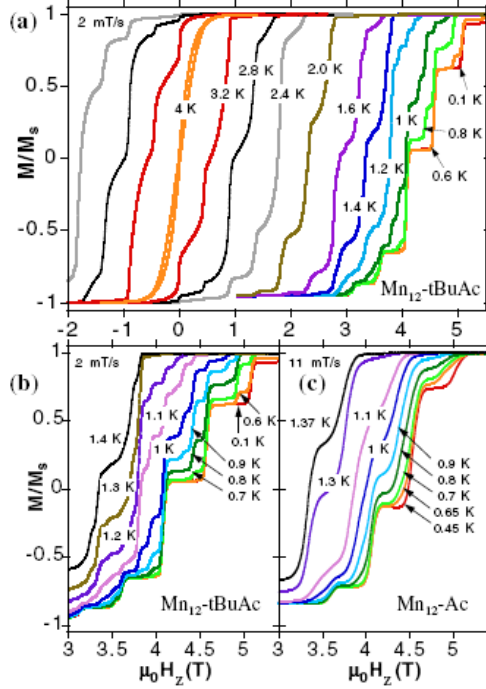
Figure 1.7: Hysteresis loops of single crystals of (a)(b) Mn_{12}-tBuAc and (c) Mn_{12}-Ac molecular clusters at different temperatures and a constant field sweep rate indicated in the figure. The data in (c) were taken from [14]. The loops display a series of steps, separated by plateaus. As the temperature is lowered, there is a decrease in the transition rate due to reduced thermally assisted tunneling. The hysteresis loops become temperature independent below 0.6 K, demonstrating quantum tunneling at the lowest energy levels. Reproduced from [4] by permission of W. Wernsdorfer, © 2006 The American Physical Society.

We also believe that the higher symmetry in the Mn_{12}-tBuAc crystal al-

---

[3]Figure's caption reproduced from [4]

lowed more detailed measurements of its longitudinal-field dependence of the relaxation rates of magnetization. Similar studies have been performed in Mn_{12}-Ac [15] but only with Mn_{12}-tBuAc have we been able to observe the level of detail necessary for a more accurate characterization of these processes.

1.2   Summary of Chapters

In chapter 2, I will first discuss the process of *spin* tunneling in a two-state system and introduce the concept of tunnel splitting. Then, I will briefly review some key theoretical results obtained by Friedman [16], Garanin, and Chudnovsky [17, 18], via perturbation theory, regarding the process of barrier reduction. So, the purpose of the first two chapters will be to give the reader enough background information to allow a clear understanding of the experimental and theoretical results in chapters 4 and 5.

In chapter 3, I will discuss the experimental techniques used to measure the relaxation rate of magnetization in Mn_{12}-tBuAc and its longitudinal- and transverse-field dependence. In chapter 4, I will discuss our experimental results and our preliminary interpretations of the data. We observe the measured transverse-field dependence of the relaxation rate for Mn_{12}-tBuAc to increase in a series of plateaus and steps. We interpret our results as evidence that the dominant levels for thermally assisted resonant tunneling change abruptly as the applied transverse-field is increased. Not all features of the experimental data could be understood, which pushed the research in a theoretical direction.

In chapter 5, I will describe how we use density matrix formalism, following the results by Chudnovsky and Garanin [17, 18], to gain a better understanding of the phonon-induced magnetic relaxation processes in Mn_{12}-tBuAc,

culminating in calculations that determine the dominant path for a molecule relaxing from one well to the other. We construct path diagrams for different transverse-fields and present them as video files that can be played in any computer. In chapter 6, I will summarize the key results in this thesis and discuss directions for future research.

Chapter 2

Theoretical Background

I will not fully develop a theoretical description of tunneling. In appendix A I sketch the textbook calculation that obtains *spatial* tunneling as a solution to Schröndinger Equation (SE) for single particles facing a potential barrier and without enough energy to overcome it. In this chapter I will show how to obtain *spin* tunneling in a two-state system by introducing a perturbation to a simple spin Hamiltonian. The objective of the first section is, therefore, to familiarize the reader with spin tunneling, and to introduce the concept of tunnel splitting.

2.1   Tunneling in a two-state system

Consider the Hamiltonian,

$$\hat{\mathcal{H}} = -\hat{\mathbf{S}}_z^2 + \hat{\mathcal{H}}', \tag{2.1}$$

where $\hat{\mathcal{H}}'$ is a perturbation to the unperturbed $\hat{\mathbf{S}}_z^2$ Hamiltonian. The attentive reader will notice the similarity of this Hamiltonian to the one in Eq. (1.8). In

the basis $|\pm z\rangle$ this Hamiltonian can be represented in matrix form by

$$\hat{\mathcal{H}} = \begin{pmatrix} \langle +z| \hat{\mathcal{H}} |+z\rangle & \langle +z| \hat{\mathcal{H}} |-z\rangle \\ \langle -z| \hat{\mathcal{H}} |+z\rangle & \langle -z| \hat{\mathcal{H}} |-z\rangle \end{pmatrix}. \tag{2.2}$$

If we let E be the eigenvalue of the unperturbed Hamiltonian ($\hat{\mathbf{S}}_z^2$) (notice the degeneracy of the eigenvalues due to the second order in the $\hat{\mathbf{S}}_z^2$ term) and $\langle -z| \hat{\mathcal{H}}' |+z\rangle = \langle +z| \hat{\mathcal{H}}' |-z\rangle = \Delta/2^1$ be the off diagonal elements, then Eq. (2.2) can be rewritten in a more friendly form:

$$\hat{\mathcal{H}} = \begin{pmatrix} E & \Delta/2 \\ \Delta/2 & E \end{pmatrix}. \tag{2.3}$$

This matrix can be easily diagonalized and we obtain two eigenstates of the Hamiltonian,

$$|\psi_1\rangle = \frac{1}{\sqrt{2}}(|+z\rangle + |-z\rangle)$$

$$|\psi_2\rangle = \frac{1}{\sqrt{2}}(|+z\rangle - |-z\rangle) , \tag{2.4}$$

with their respective eigenenergies $E_1 = E + \Delta/2$ and $E_2 = E - \Delta/2$. The time-dependent solution to the Hamiltonian is $|\Psi(t)\rangle = e^{-i\hat{\mathcal{H}}t/\hbar}|\Psi(0)\rangle$. If we set $|\Psi(0)\rangle = |+z\rangle$ we find the following solution:

$$\begin{aligned} |\Psi(t)\rangle &= \frac{e^{-i\hat{\mathcal{H}}t/\hbar}}{\sqrt{2}}(|\psi_1\rangle + |\psi_2\rangle) \\ &= \frac{1}{\sqrt{2}}(e^{-it(E+\Delta/2)/\hbar}|\psi_1\rangle + e^{-it(E-\Delta/2)/\hbar}|\psi_2\rangle) \\ &= \frac{e^{itE/\hbar}}{2}(e^{-it\Delta/2\hbar}(|+z\rangle + |-z\rangle) + e^{it\Delta/2\hbar}(|+z\rangle - |-z\rangle)) \\ &= \frac{e^{itE/\hbar}}{2}((e^{-it\Delta/2\hbar} + e^{it\Delta/2\hbar})|+z\rangle - (e^{it\Delta/2\hbar} - e^{-it\Delta/2\hbar})|-z\rangle) \\ &= e^{itE/\hbar}(\cos(\frac{t\Delta}{2\hbar})|+z\rangle - i\sin(\frac{t\Delta}{2\hbar})|-z\rangle). \end{aligned} \tag{2.5}$$

---

[1]Here we use the fact that the Hamiltonian is a hermitian operator to obtain $\langle -z| \hat{\mathcal{H}}' |+z\rangle = \langle +z| \hat{\mathcal{H}}' |-z\rangle$ and the orthogonality of the $|\pm z\rangle$ basis.

If $\hat{\mathcal{H}}' = 0$, then $\Delta = 0$, the oscillatory terms in Eq. (2.5) will be irrelevant and $|\Psi(t)\rangle = |+z\rangle$. This would mean that the states $|\pm z\rangle$ are localized and any transition is forbidden. For nonzero $\hat{\mathcal{H}}'$, however, the probability of transition to the $|-z\rangle$ state is $\sin^2(\frac{t\Delta}{2\hbar})$. If we plot the potential energy of the system versus the polar angle between the spin and the z-axis we will find that it has a *double-well* shape (see Fig. 1.2). The two wells represent the $|\pm z\rangle$ states. In our example the particle is initially trapped in the left well without enough energy to go over the barrier. The effect of $\hat{\mathcal{H}}' \neq 0$ is to allow tunneling. In the case of Mn$_{12}$-tBuAc the Hamiltonian operates in a 21 dimensional space and analytical solutions like the one we just found are not trivial [19]. We will see in the next section, however, that approximate solutions to the tunnel splitting can be found using perturbation theory.

2.2 Barrier Reduction and Thermally Assisted Quantum Tunneling

Consider the Hamiltonian in Eq. (2.6)

$$\mathcal{H} = -D\mathbf{S}_z^2 - g\mu_B H_x S_x, \tag{2.6}$$

where H_x is a small perturbation to the unperturbed $-D\mathbf{S}_z^2$ Hamiltonian. The potential diagram is represented by a *double-well* potential. A molecule that is initially localized in the $S = +10$ state and has enough energy to overcome the barrier, will do so according to an Arrhenius Law,

$$\Gamma = \omega_0 e^{-\frac{E}{T}}, \tag{2.7}$$

where Γ is the transition rate between the up and down orientations, and E is the height of the barrier[2]. The constant factor, ω_0, is the attempt frequency which represents the frequency of oscillations at the bottom of the inverted potential (i.e. the top of the barrier). I will not discuss the attempt frequency or its physical significance. The interested reader can find more information in [20].

The relaxation rate Γ depends on the temperature and on the barrier height. A lower barrier implies, according to Eq. (2.7), a larger value for Γ. How can we control the height of the barrier? Classically a transverse field (in the x-axis) would reduce the height of barrier. We can rewrite Eq. (2.6), taking it to be the total potential energy, in terms of a continuous classical variable: the polar angle the spin makes with the z-axis. The classical energy is

$$E = -DS^2 \cos^2(\theta) - h_x S \sin(\theta), \tag{2.8}$$

where $h_x = -g\mu_B H_x$, and we restrict the motion of the spin to the x-z plane. To find the top and bottom of the barrier we can find the values of θ for which the first derivative of E with respect to θ vanishes. We find the extrema to be:

$$E_{max} = -h_x S \text{ and} \tag{2.9}$$

$$E_{min} = -DS^2 \left(1 - \frac{h_x^2}{4D^2 S^2}\right) - \frac{h_x^2}{2D}. \tag{2.10}$$

The next equation gives the height of the barrier.

$$\Delta E = DS^2 \left(1 - \frac{h_x}{2DS}\right)^2 \tag{2.11}$$

This result implies that a nonzero transverse field will reduce the height of the barrier.

---

[2]The energy barrier is measured in Kelvins, since we are using units of $k = 1$ in the exponential factor in Eq. (2.7)

To reconcile the classical picture with quantum mechanics first note that, as we have seen in section 2.1, a nonzero transverse field acts as a symmetry breaking perturbation that allows tunneling between the eigenstates of the S_z operator. The tunnel splitting is, up to a factor of $\hbar$, just the frequency of oscillations between any two levels close to the resonance condition[3]. For small H_x, Garanin [21] was able to find an analytical solution to the tunnel splitting for the case $H_z = 0$ in $2|m|^{th}$ order perturbation theory. His result for the tunnel splitting is:

$$\Delta_m = \frac{2D}{[(2m-1)!]^2} \frac{(S+m)!}{(S-m)!} \left(\frac{h_x}{2D}\right)^{2S}. \tag{2.12}$$

And for $1 \ll |m| \ll S$ one can find an approximate expression[4],

$$\Delta_m \approx \frac{2D|m|}{\pi} \left(\frac{e^2 S h_x}{8Dm^2}\right)^{2|m|}. \tag{2.13}$$

The use of perturbation theory to solve for the tunnel splitting is valid for small Δ_m. From Eq. (2.13) we see that this condition no longer applies whenever $(e^2 S h_x / 8 D m^2) \geq 1$. So for $m^2 \leq e^2 S h_x / 8D$ the very large splitting implies transitions so large that the barrier above these m states becomes irrelevant to the relaxation process. One can then obtain an expression for the height of the barrier [16],

$$\Delta E_{eff} = DS^2 - D\frac{e^2 S h_x}{8D} \approx DS^2 \left[1 - \left(\frac{e^2}{8}\right)\frac{h_x}{2DS}\right]^2, \tag{2.14}$$

which differs from the classical expression in Eq. (2.11) only by a factor of $e^2/8 \approx .92$ which is of the order of 1.

What we learn from this exercise is that we can talk about a barrier reduction in the quantum mechanical picture by defining the top of the barrier

---

[3]See Eq. (2.5)

[4]Following the argument by Friedman [16] to find the effective barrier height.

to be where tunneling occurs sufficiently fast. But sufficiently fast compared to what? To answer this question we will have to account for the thermal processes that can excite a given molecule to the *effective* top of the barrier. To find the relaxation rate one must take into account all the processes that rotate the orientation of the spin. Suppose, for the sake of argument, that we apply a large longitudinal-field that populates the ground state, $m = +10$, for example. The potential diagram for this metastable state would be similar to Fig. 1.4. The magnetization, $\vec{\mathbf{M}}$, of an ensemble of Mn_{12} molecules is therefore saturated because all the spins point in only one direction. Any increase in H_z will not change the value of $\vec{\mathbf{M}}$. Suppose that we now turn off the longitudinal magnetic field, while keeping the transverse field H_x at a nonzero value in order to allow tunneling. The molecules will now try to reach equilibrium. The population of each well in equilibrium is determined by the Boltzmann factor $\exp\left[-(E_m - E_{-10})/T\right]$, which is just the ratio of the population of the m state to the population of $m = -10$ state. So, the probability that a spin initially in the metastable ground state will populate a level is exponentially dependent on m (since E_m depends on m). The tunneling rate from a given level also depends strongly on m (see exponent in Eq. (2.13)). Table 2.1 shows the tunneling rates between any two quasi-degenerate levels at $H_z = 0$ and $H_x = 100$ Oe. The values for the relaxation rate are computed using Eq. (2.12) divided by $\hbar$. The tunneling rate changes by several orders of magnitude between matching levels. For $m = \pm 3$ the relaxation time is in the order of ten seconds, while for $m = \pm 7$ the relaxation time is about ten thousand times the age of the universe.

Because the tunneling rate for a given matching pair changes so much, the chances are that the tunneling will be too fast or too slow compared to the rate of thermal activation given by the Arrhenius exponent. If for a particular level

m	Tunneling Rate (Hz)
± 1	2.4×10^9
± 2	1.1×10^6
± 3	4.1×10^1
± 4	3.4×10^{-4}
± 5	8.8×10^{-10}
± 6	8.7×10^{-16}
± 7	3.6×10^{-22}
± 8	6.6×10^{-29}
± 9	5.1×10^{-36}
± 10	1.3×10^{-43}

Table 2.1: Tunneling Rates

(m^*) the tunneling is too large, any spin that is thermally excited to that level will tunnel immediately. If, however, the tunneling on the next lower level is too slow, then the spins are effectively forbidden to tunnel. This means that we can define the barrier to be $E_s - E_{m^*}$. So, this process of thermally assisted tunneling is essentially a competition between the probability of occupancy of a given level versus the probability of tunneling due to a perturbation of the Hamiltonian.

Using the same line of argument as Garanin [21], the tunnel splitting can be obtained using perturbation theory for the condition of small transverse field and $N \neq 0$ resonance. The result is similar and can be found in [16, 20, 22]. One would expect, however, that because the probability of tunneling off-resonance is so small, the relaxation under these conditions would be entirely of thermal nature. Because of the large (orders of magnitude) differences between the tunneling rates for different m, one should also expect the barrier height to change abruptly as a function of H_x. A comprehensive theory of the transition rate has been developed by Garanin and Chudnovsky [17, 18], using the formalism of density matrix theory. In this thesis I will present some

of our new experimental results and numerical simulations that challenge our expectation of purely thermal process for the off-resonance condition, and that at the same time confirm the existence of abrupt changes in the relaxation rate (consequently barrier height) as H_x is increased.

Chapter 3

Experimental Methods

In this chapter I will describe in detail the techniques used in this experiment. Basically, we measure the magnetization of our samples using a Hall magnetometer which, as the name suggests, makes use of nothing else but the Hall effect. The essential equipment is an off-the-shelf Quantum Design Physical Property Measurement System (PPMS): a liquid helium refrigerator that can go as low as $1.8\ K$. The PPMS (Fig. 3.1) also contains a 9T superconducting magnet, with the field fixed along the z-axis. Using the Horizontal Rotator (Fig. 3.2) option for the system we can rotate our experiment along the polar angle (on the z-x plane). The difficulty in performing the experiments comes from its size. The automation of the PPMS allows students who are not very familiar with cryogenics to cool down anything that will fit inside the system. Designing and building an experiment for the small dimensions is, however, a very interesting experimental challenge. I will try to describe all phases of the experiment in enough detail for the reader to understand how we obtained the results presented on the next chapter, but I will try to keep this chapter brief in an attempt to keep the non experimentalist interested.

Figure 3.1: Quantum Design Physical Property Measurement System (PPMS) - temperature range is 1.8 K to 400 K, and contains a 9 T Magnet.
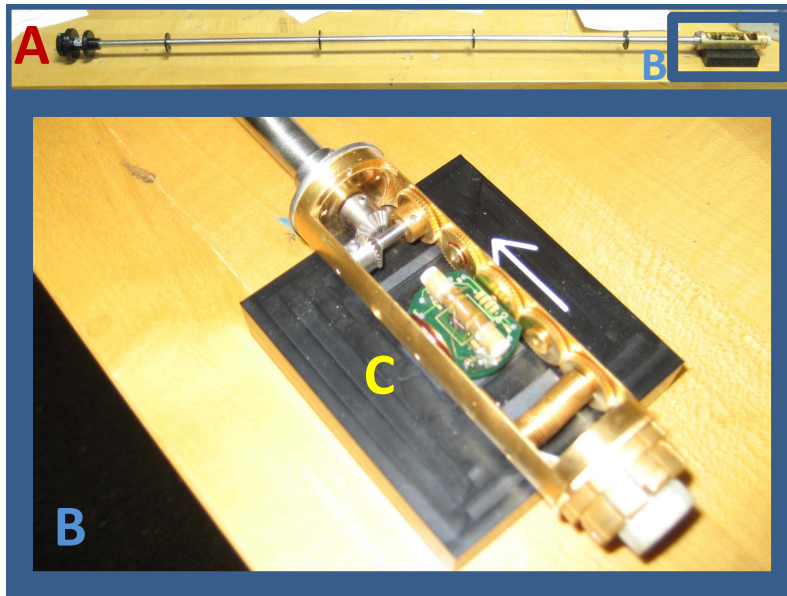

Figure 3.2: Horizontal Rotator - (A) full length of the probe, (B) enlarged view of the spring system, and (C) board with Hall sensor (not visible) and AC susceptibility coil.

3.1 Hall Sensor

The Hall sensors used in this experiment are provided by Prof. Eli Zeldov's group at the Weizmann Institute in Israel. The Hall sensor is a square semiconductor chip ($0.2''$ sides) with several contact pads on the outside (see Fig. 3.3). The Hall Bar is located at the center of the chip. The outside pads are electrically connected to several areas of the Hall bar. In essence, the Hall bar measures the normal component of incident magnetic fields. The classical Hall effect is applicable, as long as we are confined to fields below $1\ T$ ($10^4\ Oe$). We apply a current along the length of the Hall Bar and any magnetic fields perpendicular to the current will induce a voltage differential along the width of the sensor (Fig. 3.4).

Most experiments were realized using a Hall current of $50\ \mu A$, although sometimes we have pushed it to $100 \mu A$. A larger current could potentially warm up any crystals mounted on top of the Hall sensor. We have characterized the field response of the Hall sensors in this experiment and the result can be seen in Fig. 3.1. The straight line for fields below $1\ T$ is the classical Hall effect. Above $1\ T$ we see the Hall resistance increasing in a series of steps, which is nothing else but the *Quantum Hall Effect*. We perform our experiments away from the nonlinear region and we have found the sensitivity of the Hall sensor to be independent of temperature between $2\ K$ and $10\ K$.

To prepare the Hall sensor for experiment we first have to fix it, using varnish, on top an insulating board (see Fig. 3.6) that fits on the Horizontal Rotator (Fig. 3.2(C)). We connect the pads on the Hall sensor to the pads on the board using a Kulicke and Soffa Model 4124 Thermosonic Gold Ball
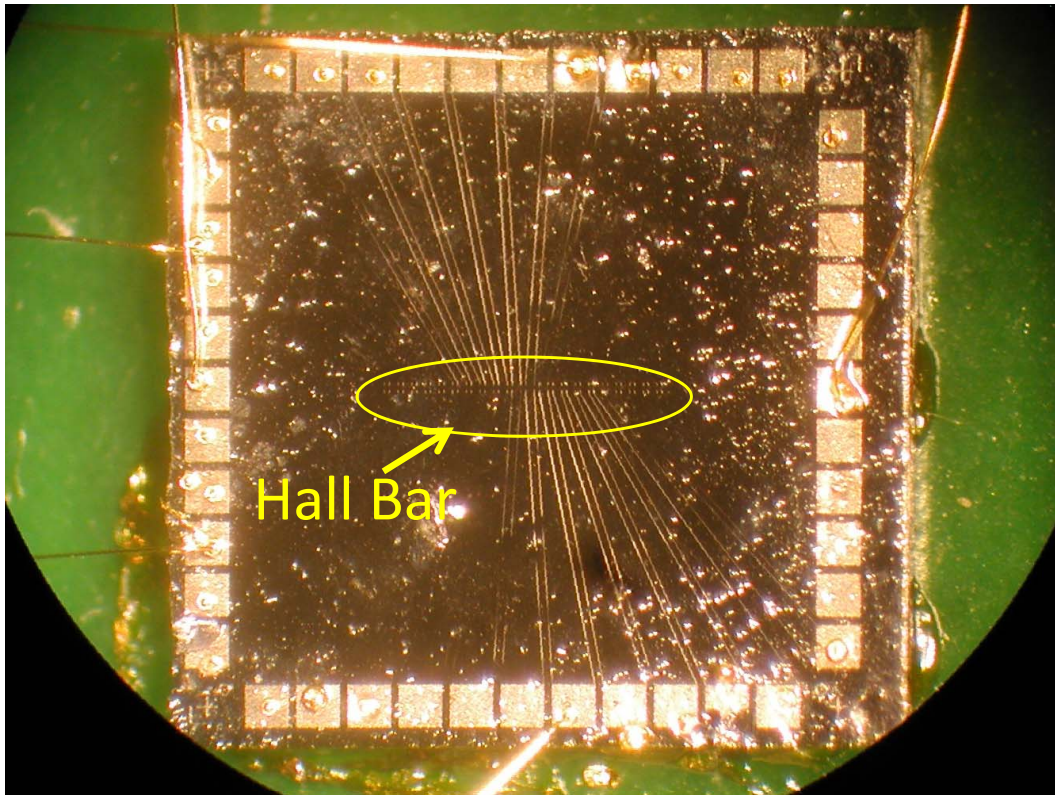
Figure 3.3: Hall Sensor — the Hall bar is located at the center. The current is along the horizontal coordinate and the voltage is measured across the width of the Hall bar. Some leads between the outside pads and the Hall bar are visible.
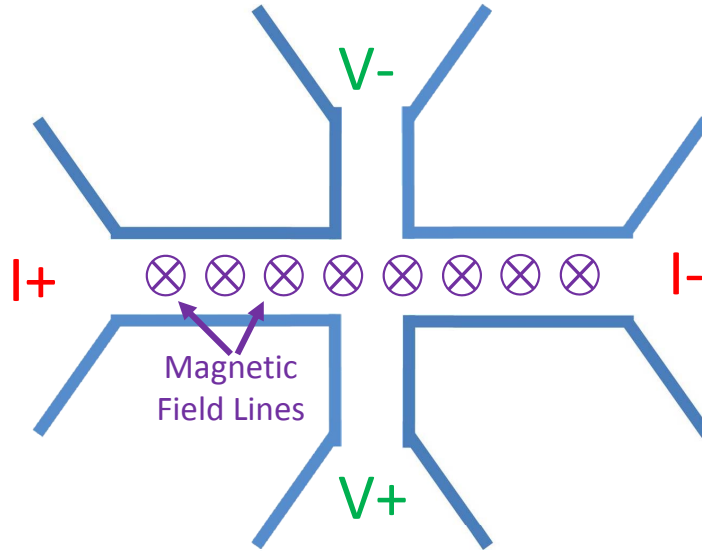
Figure 3.4: Hall Effect – Current is applied along the horizontal axis. The magnetic field (into the page) induces a voltage difference across (vertical axis) the width of the Hall bar.
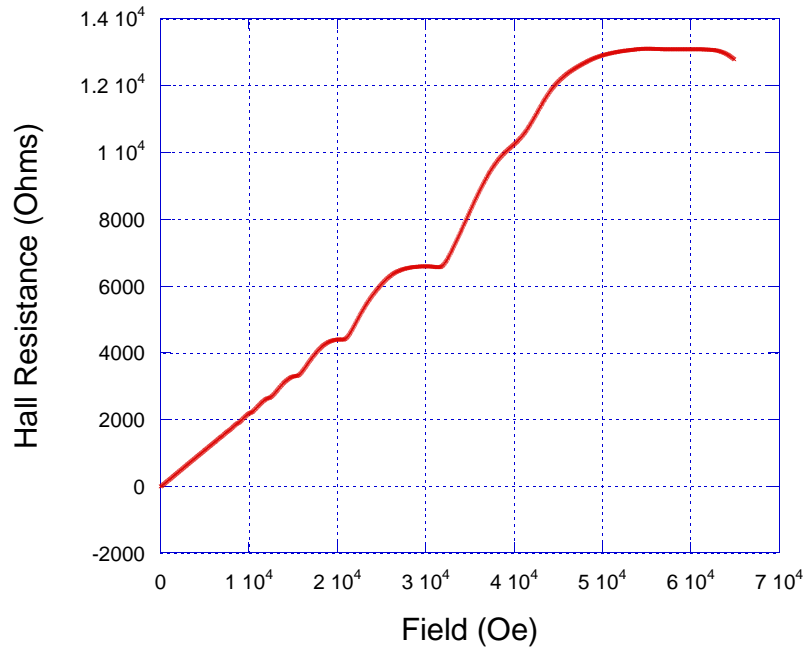
Figure 3.5: Hall resistance versus applied magnetic field at $3.21(1)$ $K-$ below 1 T the Hall resistance increases linearly with field.

28

Bonder[1]. The Hall sensor, now fixed on the insulating board, is clamped to
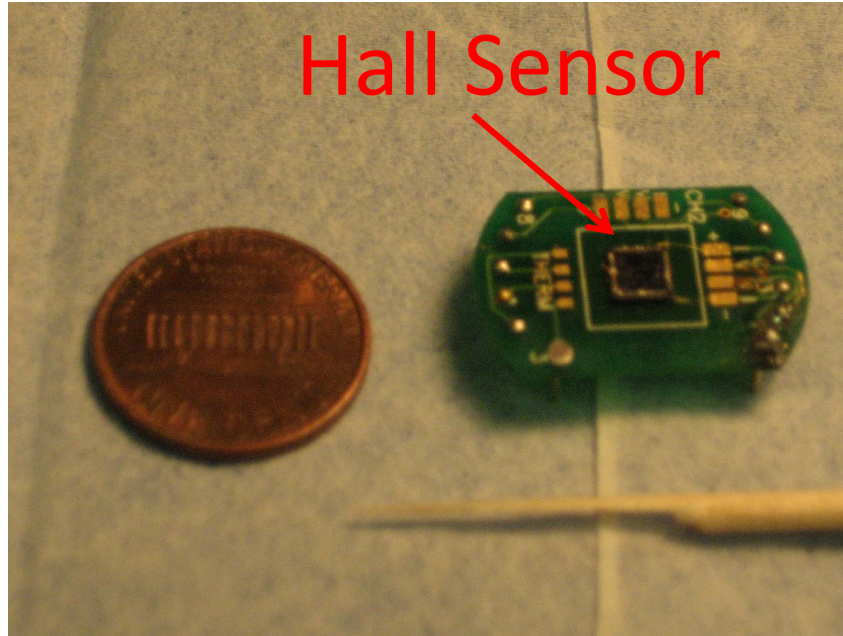
Figure 3.6: Hall sensor fixed on top of the insulating board.

the workholder and heated to approximately 120 ℃. A golden wire, 1 mil in diameter, is fed through a capilary. In the end of the capilary, a high voltage is applied to the wire, initiating a spark that cuts it and leaves a ball in the end of the hanging piece. The ball is slightly pressed against one of the Hall sensor pads (too much force could damage the pad) followed by an ultrasound pulse that forces the surfaces together. The next bond is made onto the board and it is accomplished essentially in the same way as the first bond, except that it has no ball in the end. After the second bond, a wire connecting the Hall sensor to the board is left behind, a new ball is created and the bonder

[1]Before briefly describing its operation, I cannot resist mentioning that going through the experience of using this machine requires a lot of patience. Although we would like to believe otherwise, the calibration of this machine is not sensible and putting it to work can be regarded as an art. Once it is operational, however, this machine is an essential part of the lab.

is ready for work again.

In our setup we have to make six bonds: two leads to measure the voltage across the Hall Bar at the position where our Mn_{12}-tBuAc crystal will be mounted. Another pair is necessary to measure the voltage across the Hall bar at a position far from the first pair; this is our control pair. In this manner, we can electronically subtract this *background* voltage from the signal collected by the first pair, in order to isolate the signal coming purely from the Mn_{12}-tBuAc crystal. A third pair is connected to ends of the Hall bar and is used to feed the current through the Hall Bar.

The bonds are very delicate and must be tested. Sometimes a visually good bond can present a *Schottky Effect*. The Schottky barrier is a term usually linked to the energy barrier a charge must overcome in the interface of two semiconductors. In our case, we use this term to refer to the energy barrier on the interface of a semiconductor (the pad on the Hall sensor) and a conductor (the gold ball in the end of the wire). We measure the resistance of the bond in the dark and under room lighting. A bad bond exhibits a large resistance in the dark (in the order of 1 $M\Omega$) and a smaller resistance under the light (in the order of 100 $k\Omega$) due to photoexcited electrons having more energy to overcome the Schottky barrier. It is hard to say what causes this kind of anomalous behavior but my guess would be that, in ninety percent of the cases, the Hall sensor's pad was damaged by excessive force during the wire bonding process. If this is indeed the case, it becomes quite possible that the connection pads and adjacent pads are forever damaged. There are two more ways in which I have observed bad bonds. One happens when paratone-N oil, discussed in the next section, reaches the contact pads. The other way is the obvious one: breaking the wire.

3.2 Sample Manipulation

We receive our Mn_{12}-tBuAc samples from our colleagues in the Christou Group at the University of Florida. As soon as they are prepared they are sent to us via the fastest courier service available, at which time we immediately store them below 0℃. The samples have been grown as single crystals. They ideally have a needlelike shape which serves as an indicator of the z-axis orientation (the crystallographic easy-axis). They are kept inside their mother liquor because they are very sensitive to any contact with the air. Because Mn_{12}-tBuAc is much more sensitive to the environment than Mn_{12}-Ac, we had to develop a new way of handling these crystals. To prevent the crystal from having any contact with the air, we use a cryogenic oil commercially known as paratone-N[2]. The crystals are pulled out of the mother liquor using a spatula containing paratone-N on one of its tips. This way the samples become immersed in the oil and are not placed in contact with the environment. Then they are placed on a glass plate that contains some paratone-N oil. At this stage these samples are still protected from the environment. Under the microscope we look for some key characteristics. First, the sample should have the needlelike shape mentioned before. Second, it should have sharp edges and corners; ideally our sample looks like a parallelepiped (see Fig. 3.7). Third, we want a small sample (300 $\mu m \times 50 \mu m \times 50 \mu m$). One would initially think that a large sample (1.5 $mm \times 300 \mu m \times 300 \mu m$) would be preferable since it would allow an easier coupling to the Hall bar. Although true, in the summer of 2006 we found out that a large sample can be a huge liability. We were performing high transverse-field experiments on Mn_{12}-Ac using large samples. After loosing the signal a few times we realized that our samples were break-

---

[2]Sold by Hampton Research.

ing apart after applying the transverse-field. In the presence of such a field, the sample tends to torque around it. In one control experiment we placed a large sample, surrounded by an excessive amount of paratone-N oil, sitting horizontally on a test board. After cooling down the sample below 3 K, a transverse magnetic field of 2.5 T was applied. We then warmed up the sample to room temperature and found out that the sample had rotated to the vertical position. Half of its structure had been ripped out and could not be found anywhere in sight.
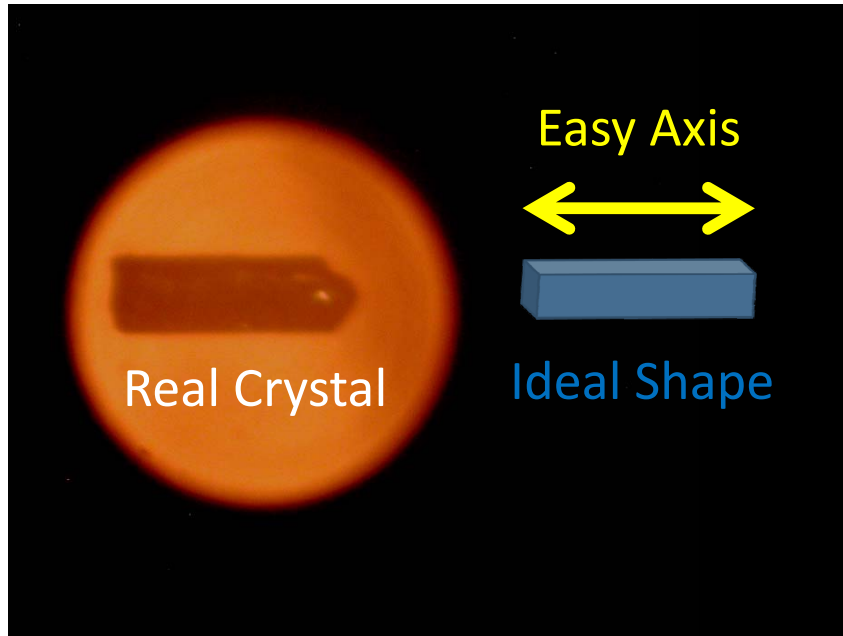
Figure 3.7: Real Mn$_{12}$-tBuAc single crystal (left) and its ideal shape (right).

On the glass board and inside the paratone-N oil it is necessary to move the sample around to inspect its geometry. I use a wooden stick applicator (Fig. 3.6) broken in half so that its tip is very sharp. The paratone-N oil has a very high viscosity, so any attempts to push the sample will not be successful. Touching or poking it could break it. Instead, it is preferable to pull the oil around the sample, creating, therefore, a track to be followed by the sample.

After identifying the correct sample, one must move it to an area on the glass plate that contains no oil. The sample will still be protected because it dragged some oil with. Then using the wooden tip with a very small droplet of oil we pick up the sample and move it to the top of the Hall Sensor. This next stage is very delicate and it must be realized as fast as possible. Because there is not much oil around the sample, it could come in contact with the environment. The least amount of oil is desired, because, as discussed in the end of the last section, paratone-N can damage the gold wire contacts on the Hall sensor.

Once the sample is on top of the Hall sensor, we move it into place. The best position is perpendicular to the Hall bar. Any field lines just exiting the crystal along the easy-axis will be maximally detected if the sample has one of its ends just next to the Hall bar (see Fig. 3.8). And we want the sample positioned right next to the part of the Hall bar that is connected to the desired voltage pair (see last section). It turns out that the coupling between the sample and the Hall bar is much more critical for a good signal-to-noise ratio than the size of the sample.
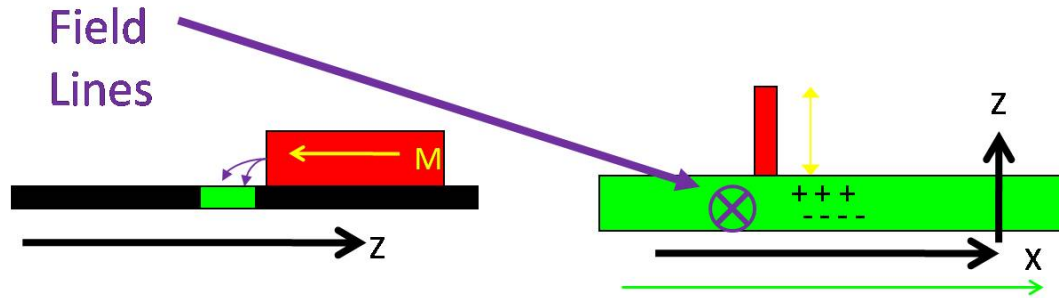
Figure 3.8: Different schematic views of the Mn_{12} crystal (red) on top of the Hall sensor – when the crystal is just next to the Hall bar (green) the field lines (purple) due to crystal's magnetization (yellow) induce a voltage across the width of the Hall bar.

3.3 Measuring the Magnetization

There are two ways in which we can measure the magnetization of Mn$_{12}$-tBuAc. One is to use the Hall sensor to measure the magnetization of the sample as a function of time. An alternating current (50 μA and 37 Hz) is applied to the current leads in the Hall bar. To achieve this current we just apply 5 V through a 100 $k\Omega$ resistor in series with the Hall bar. We then collect the voltage signals from the pair connected close to the sample (V_{sample}) and the one away ($V_{control}$), and amplify both signals by 100. After amplification, $V_{control}$ is subtracted from V_{sample} through an electronic subtraction circuit. The signal is then sent to a SRS SR830 DSP Lock-in Amplifier. The wiring can be seen in Fig. 3.9.

Figure 3.9: Schematic of electric signals as explained in the text – A = Amplifier, AC-SC = AC Current Source, S = Subtraction Circuit.

To measure the relaxation rate of the Mn$_{12}$-tBuAc sample, we set the temperature and then apply a magnetic field using the PPMS superconducting

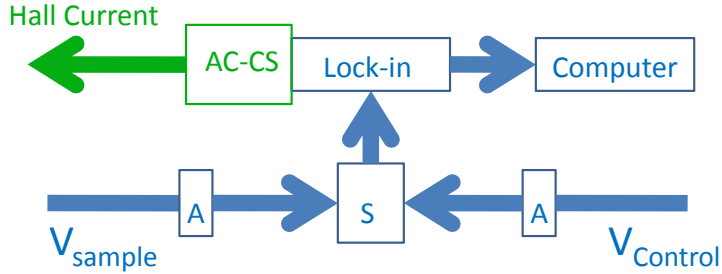magnet. We then rotate the sample to A (see Fig. 3.10), an angle where the the easy-axis is aligned with the field. This first step tilts the potential and populates the lower well. Then the sample is rotated to B, where there is a large component of the field transverse to the easy-axis and a very small component of the field along the easy-axis. For each measurement the total field, H_T, is adjusted to meet the desired components of H_x (transverse) and H_z (longitudinal). This requires nothing more than simple trigonometry: $tan(\theta - \theta_0) = H_z/H_x$ and $H_T^2 = H_z^2 + H_x^2$, where θ_0 is the angle at which $H_z = 0$. During the rotation, and just before arriving at the final angle, a voltage is sent to the trigger input of the lock-in. This signal initiates the data storage in the lock-in buffer. The data is then transfered to a text file in the computer. This entire process has been automated using the LabView control interface: it requires just the push of a button.
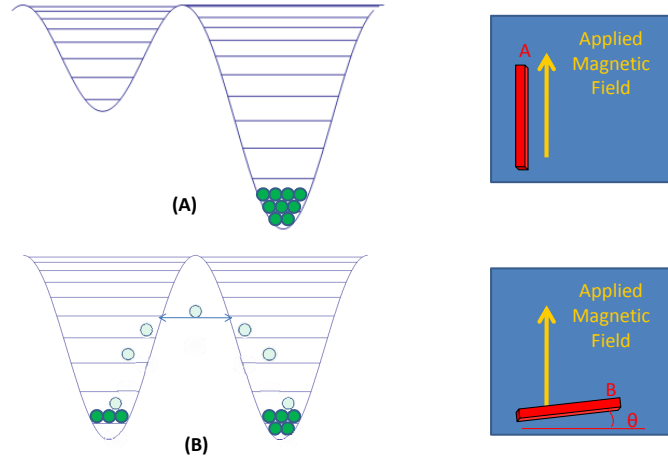

Figure 3.10: Measuring the relaxation rate – sample is rotated to position A, (populating the lower well) then rotated to B (allowing the relaxation process to occur).

This technique has its limitations. First, the relaxation rate must be slow

compared to the angular speed of the horizontal rotator (11.97 degrees per second). Second, the lock-in acquisition rate is bounded above by 512 Hz. This turns out not to be a problem because the rotator condition breaks down before a fast acquisition rate is required[3]. Our technique has worked remarkably well for temperatures between 2.87 K and 3.32 K. It could in principle work at lower temperatures as well, but the relaxation time increases dramatically. This is due to the exponential Arrhenius factor in Eq. (2.7). Taking the barrier height to be ≈ 70 K the Arrhenius exponent changes by two orders of magnitude between 2.5 K and 3.0 K.

One method to quantify the height of the barrier is to measure the relaxation for different temperatures and perform a linear regression using the equation

$$ln(\Gamma) = -\frac{E}{T} + ln(\omega_0), \tag{3.1}$$

and $1/T$ as the free variable. Equation (3.1) is just the Arrhenius Law (Eq. (2.7)) rewritten after algebraic manipulation. The problem is that, in the temperature range of this technique, $1/T$ only varies from .30 to .34. To overcome this problem we have to use the AC Susceptibility measurement technique as described in the next section.

3.4 AC Susceptibility

In essence, the AC Susceptibility (ACS) measurement is just a relaxation experiment where the variable has been changed from time to frequency. Assume

---

[3]In an earlier version of the experiment we did not use the lock-in for data storage, instead we triggered an oscilloscope (Tektronix TDS 210) to take a trace of the magnetization and then uploaded that trace to the computer. This presented problems because of a digitization effect that represented the relaxation in a series of decreasing steps as a function of time.

that all molecules are identical. This implies that the total magnetization of the system, M, is decaying exponentially. The dynamical equation describing this process is:

$$\tau \frac{dM}{dt} + M = 0. \tag{3.2}$$

If we now add an oscillating magnetic field the RHS of Eq. (3.2) will no longer be zero. This is equivalent to adding a driving force to a simple harmonic oscillator. The dynamical equation is

$$\tau \frac{dM}{dt} + M = \chi_0 H_0 cos(\omega t), \tag{3.3}$$

where χ_0 is the magnetic susceptibility in the presence of a nonoscillating magnetic field (i.e. $\vec{\mathbf{M}} = \chi_0 \vec{\mathbf{H}}$) and $H_0 cos(\omega t)$ is the oscillating field. One could guess that the solution for M is

$$M = \chi_R H_0 cos(\omega t) + \chi_I H_0 sin(\omega t), \tag{3.4}$$

where we now allow the susceptibility to have real (in-phase) and imaginary (out-of-phase) components, χ_R and χ_I, respectively. We expect that in the limit of slow oscillations the magnetization should be able to follow the oscillating field which means that $\chi_R = \chi_0$ and $\chi_I = 0$. We also expect that in the limit of large ω the average field seen by particles is zero and both χ_R and χ_I should be zero. We can plug Eq. (3.4) into Eq. (3.3). After some algebraic manipulations we obtain:

$$sin(\omega t)[\chi_I - (\omega\tau)\chi_R] + cos(\omega t)[\chi_R + (\omega\tau)\chi_I - \chi_0] = 0 \ .$$

For the last equation to be true, we require the cosine and sine terms to vanish for all ωt. These conditions give a system of two variables and two equations which can be easily solved to obtain expressions for χ_R and χ_I:

$$\chi_R = \chi_0 \frac{1}{1 + (\omega\tau)^2} \ , \tag{3.5}$$

$$\chi_I = \chi_0 \frac{\omega\tau}{1 + (\omega\tau)^2} \ . \tag{3.6}$$
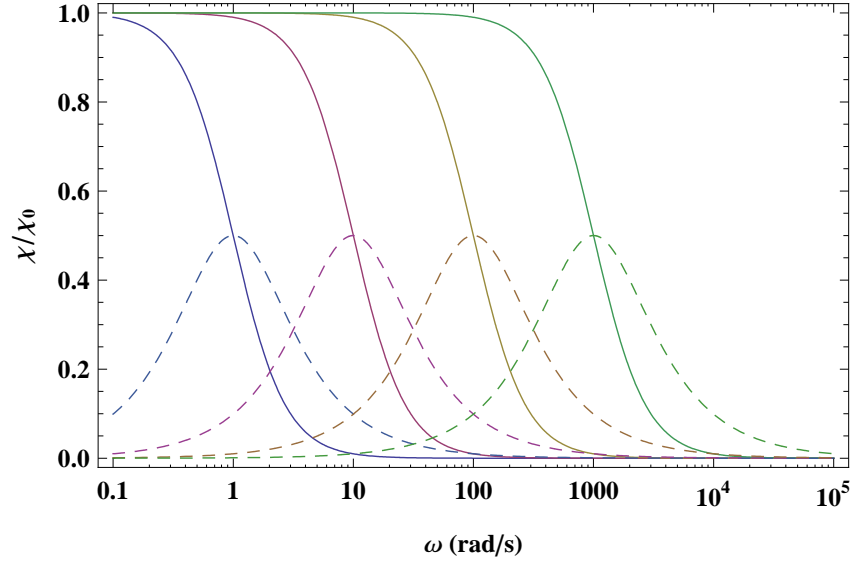
Figure 3.11: AC Susceptibility – real (solid) and imaginary (dashed) curves intersect at $\omega = 1/\tau$.

The solutions for $\tau = 1, 1/10, 1/100, 1/1000$ seconds are plotted in Fig. 3.11. The imaginary component peaks at the frequency value corresponding to $1/\tau$ which is the relaxation rate of the magnetization.

To perform ACS experimentally, we put a small coil on top of the Hall Sensor, and parallel to the sample. This way, the field lines emanating from the ends of the coil will wrap around themselves, and the magnetic field felt by the crystal will roughly be along the easy-axis (see Fig. 3.4). We can apply a DC current through the Hall bar and an alternating current through the coil. To measure the susceptibility, we use the relation $\vec{\mathbf{M}}(\omega) = \chi(\omega)\vec{\mathbf{H}}(\omega)$, where ω is the frequency. So, we can use the coil current as the lock-in reference and by measuring the in-phase (χ_R) and out-of-phase (χ_I) components of the Hall voltage we should obtain the susceptibility.

Since the coil is parallel to the sample, and we apply large magnetic fields
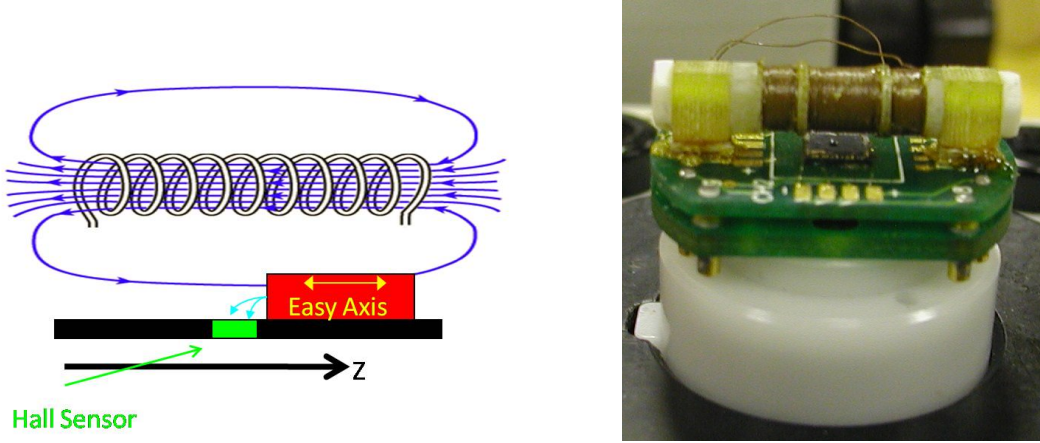
Figure 3.12: ACS – field outside the coil is roughly along the easy-axis of the single crystal.

(on the order of $1\ T$) perpendicular to the sample, the coil could torque around the field. Although the coil is firmly attached to the top of the insulating board, the board is on the horizontal rotator. So, a large transverse-field could possibly torque the board, and therefore the sample. To avoid these kinds of problems we constructed a gradient coil (Fig. 3.13). From top to bottom in the figure there are N turns counter-clockwise, $2N$ clockwise, and finally N turns counter-clockwise. Since the coil is confined to a region where the applied magnetic field (from the PPMS magnet) will be uniform, it will not torque since its dipole moment will be zero. In our design, the coil holder is made of G-10 and it can accommodate 7 layers and $N = 19$. At room temperature the field outside the coil (at the expected position of the sample) was measured to be $10\ Oe$.
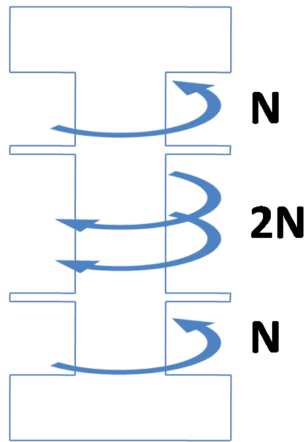
Figure 3.13: Gradient coil — top to bottom there are N turns counter-clockwise, $2N$ clockwise, and finally N turns counter-clockwise.

Chapter 4

Experimental Results

In this chapter I will present the results of several measurements done on a Mn_{12}-tBuAc crystal. We performed measurements from June of 2007 to December of 2007 on the same sample. The results will be presented in three parts. First, I will discuss the experiments done near the zero-field resonance using the real-time relaxation method to measure the relaxation rate of magnetization. We analyze both the longitudinal- and transverse-field dependences of the relaxation rate. From that data we are able to extract the off-resonance and on-resonance relaxation rates. The relaxation rates as a function of transverse-field suggest abrupt changes in the effective barrier height for Mn_{12}-tBuAc. Second, we do a similar analysis of the data from the ACS method. Third, I will present data for real-time relaxation measurements near the $N = 1$ resonance.

The first step to know if we have a working crystal, is to take a hysteresis loop. If the sample is a single crystal we should be able to observe the characteristic steps at temperature independent values of the field (Fig. 1.3 for Mn_{12}-Ac). The hysteresis loops for Mn_{12}-tBuAc are displayed in Fig. 4.1

for different temperatures. Unfortunately, in January of 2008, this sample
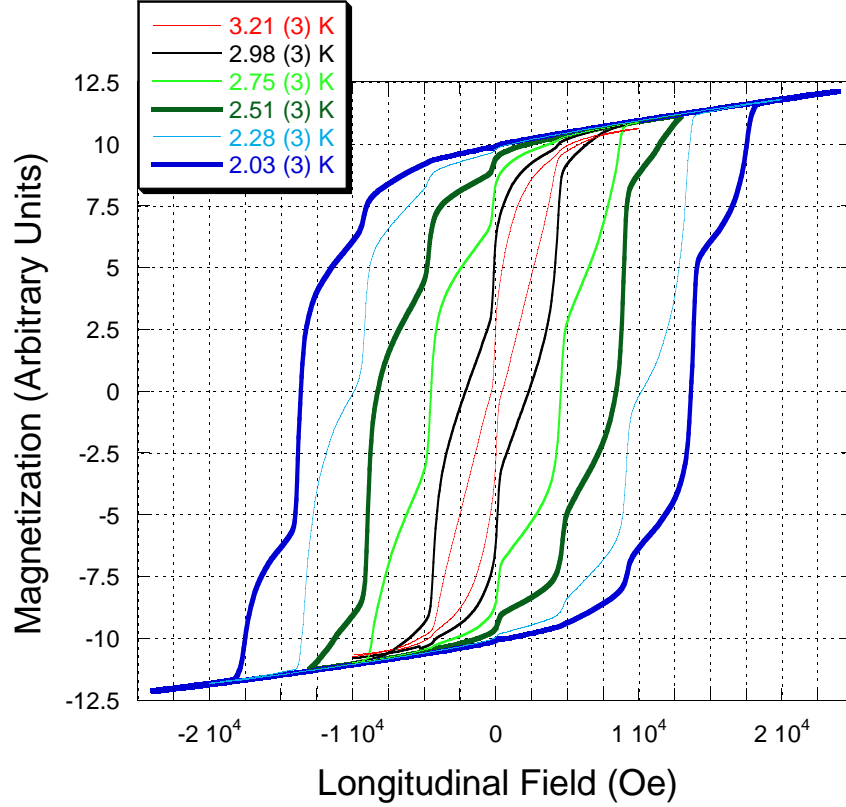
Figure 4.1: Hysteresis loops for different temperatures.

no longer presented these characteristics, prompting us to declare its death. Considering the high sensitivity to environment, present in Mn_{12}-tBuAc crystals, this sample performed well for a long period of time. During the following months, seven samples were mounted, but either they did not show the desired characteristics in the hysteresis loops, or the PPMS had temperature control issues. That is unfortunate, because we believe that the problems have now been partially fixed, and the automation of the experiment should allow for large sets of data to be taken uninterruptedly. These problems prevented more data to be taken from the ACS measurements and for the $N = 1$ experiments.

4.1 Relaxation Near the Zero-field Resonance — Real-time Relaxation Measurements

After setting the desired temperature, longitudinal- and transverse-fields, we observe the time-evolution of the magnetization. Figure 4.2 shows three decay curves, two of which are off-resonance and one which is on resonance. We
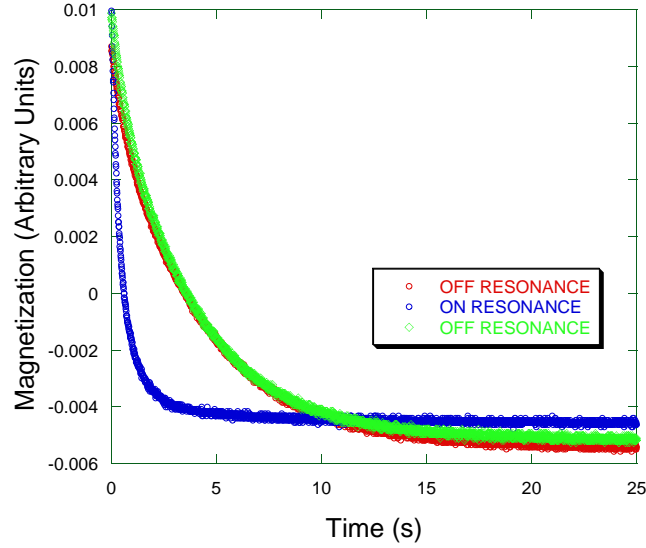
Figure 4.2: Relaxation of magnetization on- and off-resonance at a transverse-field of 4800 Oe and 3.21(3) K.

observe the decay rates to be smaller for the off-resonance curves. We fit these curves to exponential decay functions and extract the value of the decay rate, which we interpret to be the relaxation rate, Γ, of the magnetization. The numerical fits are very good, as it can be seen in Fig. 4.3. A detailed analysis of the residuals, however, indicates that the relaxation is not really a pure exponential, and an example of the residuals can be seen in Fig. 4.4. We find that the skewed residuals effect seen in Fig. 4.4 is much more pronounced at the near-resonance relaxations (Fig. 4.5). We tried to use more complicated functions for the fitting routine. Examples of these functions are stretched

43
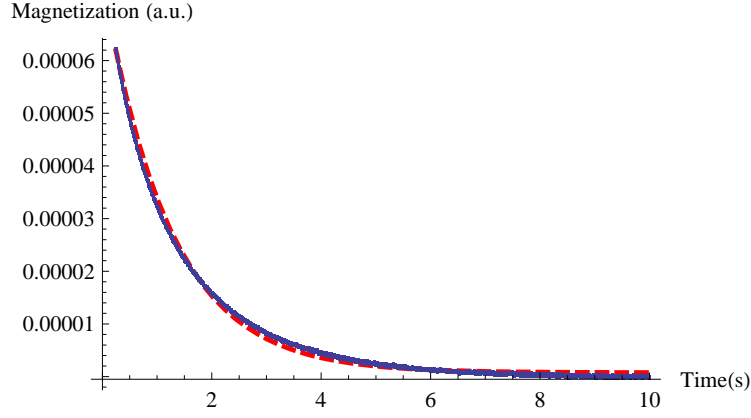
Figure 4.3: Exponential fit (dashed line) for relaxation of magnetization off-resonance ($H_z = 500\ Oe$) – 3 K, 6000 Oe transverse-field.
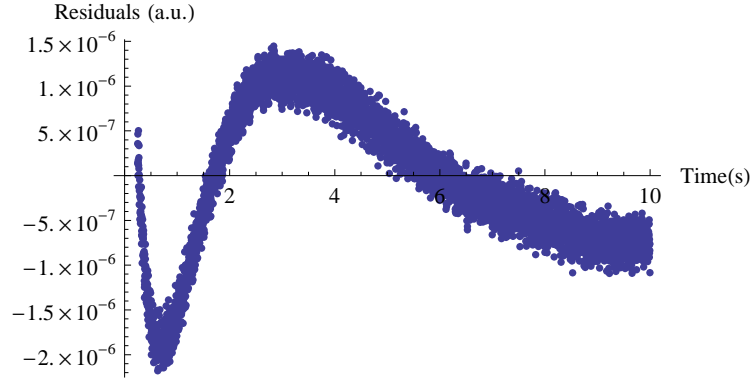
Figure 4.4: Residuals from best fit in Fig.4.3.
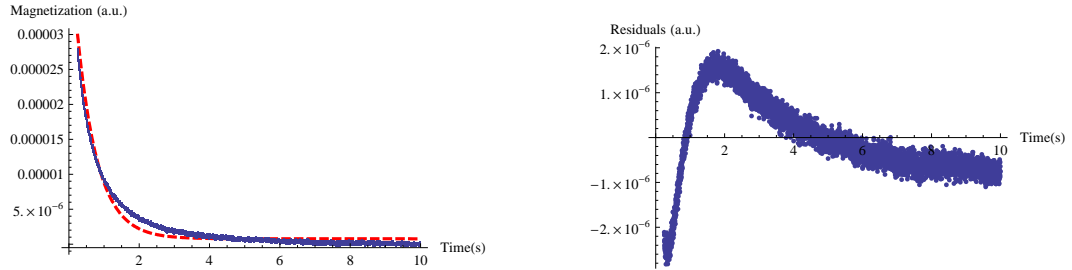
Figure 4.5: Exponential fit (dashed line) for relaxation of magnetization on-resonance ($H_z = 20\ Oe$left) and residuals(right) – 3 K, 6000 Oe transverse-field.

44

exponentials, double exponentials and a convolution of exponentials. The last two produced better fits, but that is probably because they have an extra fitting parameter. And, although the fits were better, the skewed residuals remained. A double exponential decay would occur if there two different relaxation mechanisms, one for the initial relaxation and one for the long-time time evolution. We don't have a physical picture that justifies the use of a double exponential. In appendix B, I discuss the reason why a convolution of integrals could be the correct fit and why we abandoned this model. In the end, however, an exponential seemed to be a better candidate to, at least, give a *measure* of the relaxation.

For a fixed transverse-field we take the relaxation curves for several values of longitudinal field (Fig. 4.6). We find the shape of the curve to fit well to a Lorentzian function but not well to a Gaussian function (Fig. 4.7).
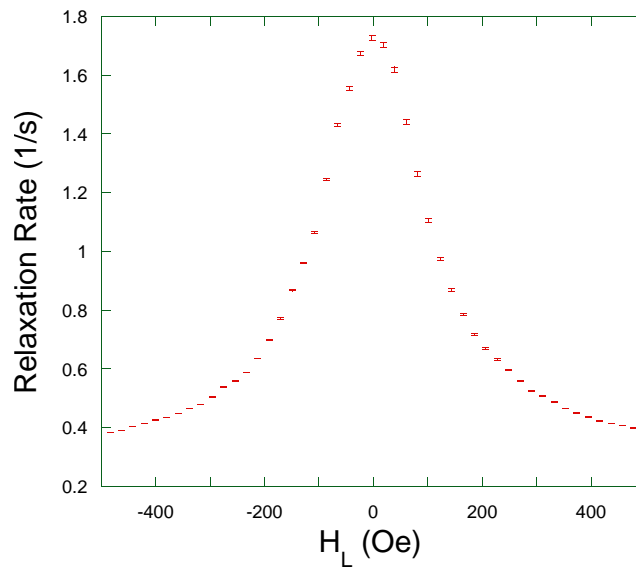
Figure 4.6: Longitudinal-field dependent relaxation rates at $3.21(3)$ K and 4600 Oe transverse-field.

This suggests that the peak in the relaxation rate curve is not due to some
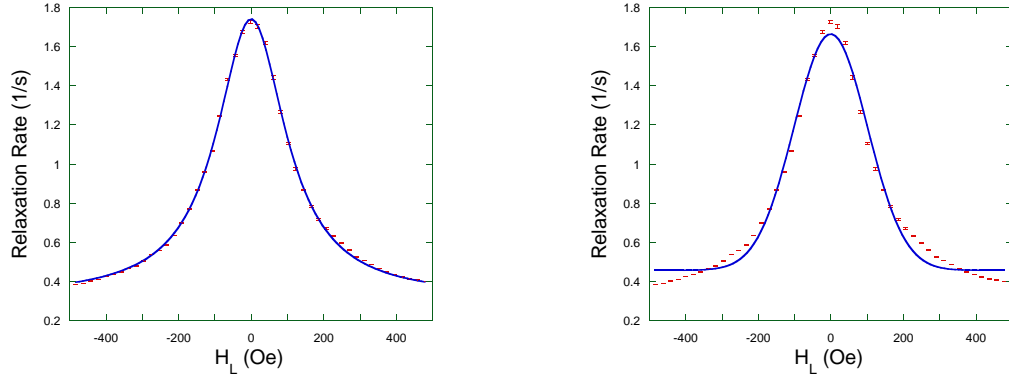
Figure 4.7: Longitudinal-field dependent relaxation rates at 3.21(3) K and 4600 Oe transverse-field. Lorentzian fit (left) and Gaussian fit (right).

kind of statistical distribution. The latter could happen, for example, due to crystalline disorder of the easy-axes of the spin in the lattice structure [13]. The Lorentzian fit is

$$\frac{(a-b)}{1+\left(\frac{H_z-d}{c}\right)^2} + b, \tag{4.1}$$

where there are four fitting parameters (a,b,c,d) and H_z is the free variable. From each Lorentzian fit, we extract the relaxation rates for $H_z = 0$ (on-resonance, a) and in the limit of very large $|H_z|$ (off-resonance, b), and the width of the distribution at half maximum (c). These values are presented in Figs. 4.8, 4.9 and 4.10 as a function of transverse field.

We can observe the existence of plateaus and steps on both the on-resonance and off-resonance relaxation curves. We also observe oscillations in the widths of the resonance. Let us first focus on the on-resonance data. There is a simple way in which we can interpret the existence of the plateaus and the steps. It was predicted by Friedman [16], and Garanin, and Chudnovsky [17, 18], that the effective height of the barrier should decrease as a function of transverse-field. In the absence of a magnetic field, a molecule will have to relax to the other well by climbing the entire anisotropy barrier (Fig. 4.11(a)). Suppose

46
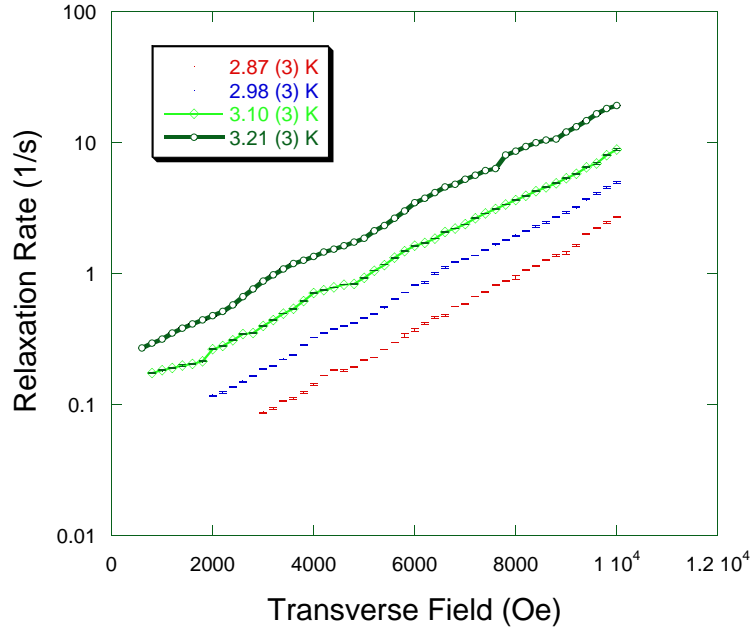
Figure 4.8: Relaxation rate on-resonance as a function transverse field for different temperatures.
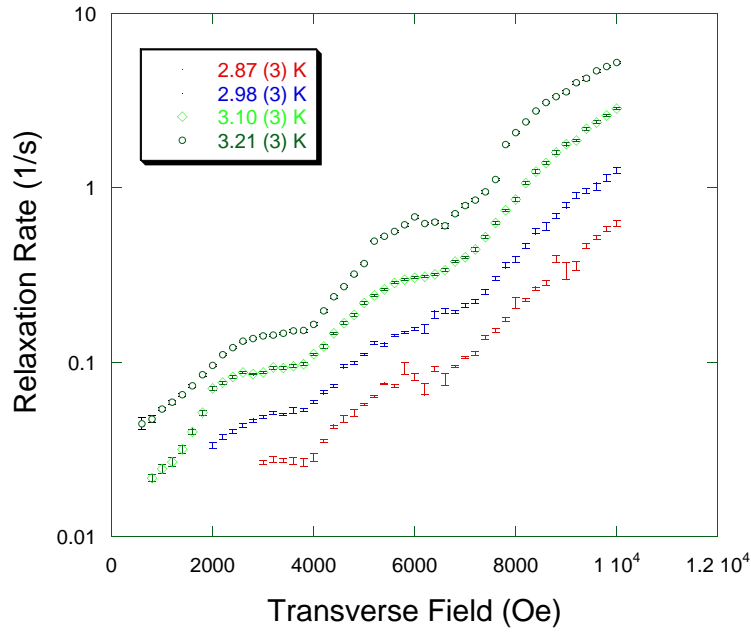
Figure 4.9: Relaxation rate off-resonance as a function transverse field for different temperatures.
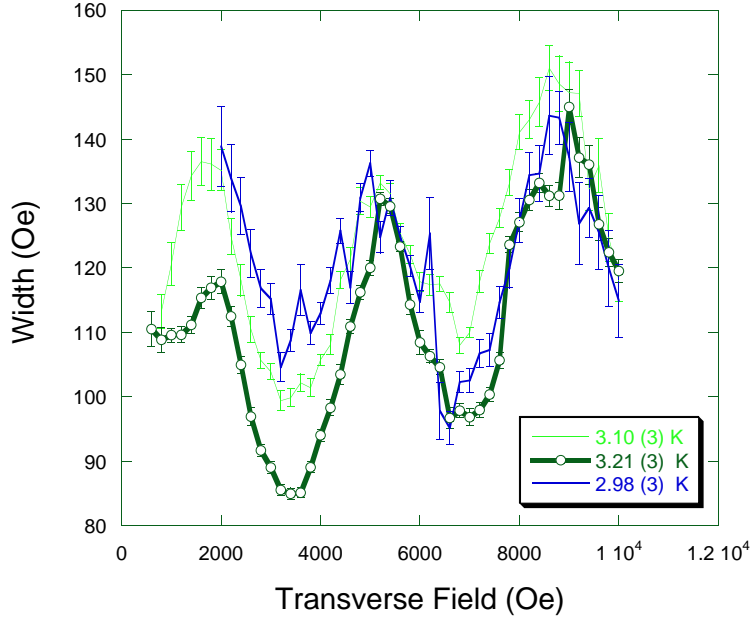
Figure 4.10: Lorentzian widths as a function transverse field for different temperatures.

that for a given value of transverse field, the spin has to climb the potential barrier to a given level, tunnel and then decay to the opposite ground state (Fig. 4.11(b)). Also note that the tunneling for a given pair of states on opposite sides of the barrier depends strongly on the perturbation to the Hamiltonian, in this case the transverse-field. If the transverse-field is increased, the tunneling between the next lower pair of states becomes relevant. That is when a step occurs in Fig. 4.8, and both pairs of resonant levels are used in the relaxation path of the spin (Fig. 4.11(c)). If we continue to increase the transverse-field, the next pair becomes the dominant resonant pair and we observe another plateau (Fig. 4.11(d)).

The oscillations in the width also agree with this interpretation. In Fig. 4.12 we plot the longitudinal-field dependent curves for several transverse-fields. We interpret the oscillations to happen due to the simultaneous presence of
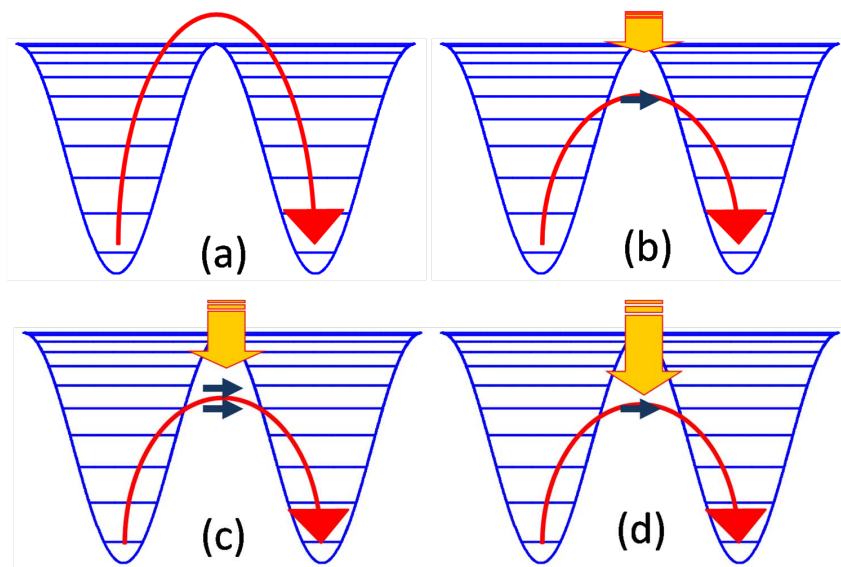
Figure 4.11: Barrier height for different transverse-field (yellow arrow). In the absence of field the molecule must overcome the entire anisotropy barrier (a). For a given transverse-field a dominant tunneling (blue arrow) resonance determines the height of the barrier (b). As the transverse-field is increased, a new tunneling resonant becomes relevant to the relaxation process (c). And for a higher transverse-field, the new tunneling resonance becomes the dominant tunneling pair (d).
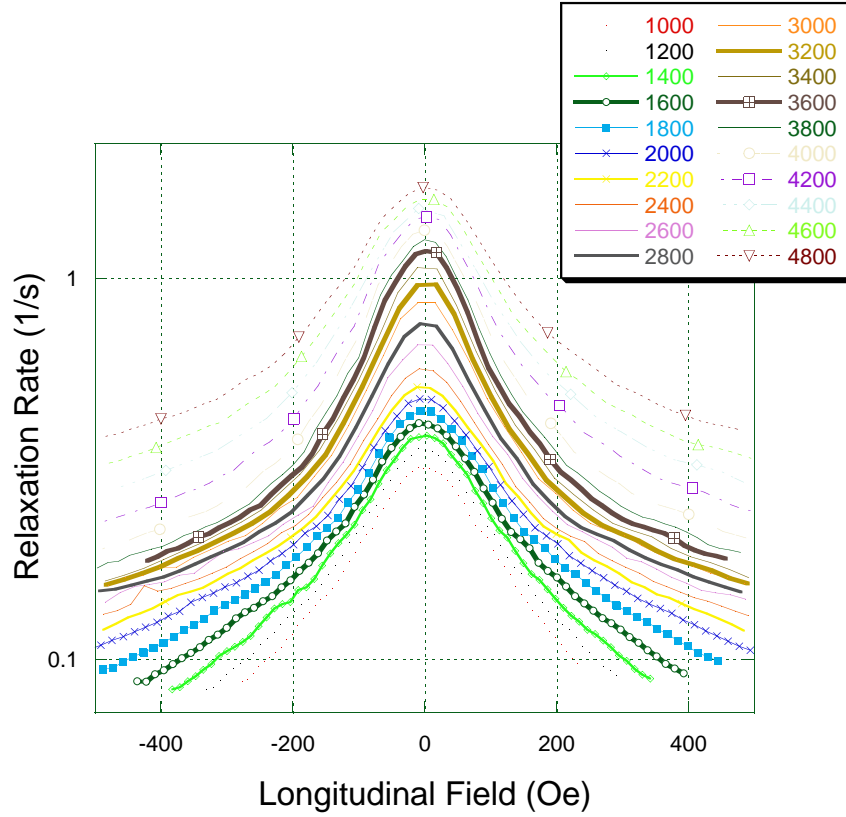
Figure 4.12: Longitudinal-field dependent relaxation rates for different transverse-fields (in Oe) at 3.21(3) K.

tunneling resonances. Suppose that at a certain transverse-field there exists a dominant tunneling resonance. In Figs. 4.13, 4.14 and 4.15, we make the connection between Fig. 4.12 and Fig. 4.11. As the transverse-field is increased, a new resonance becomes relevant to the dynamics, superimposing, therefore, a sharp Lorentzian on top of the old one (Fig. 4.14). But once the new resonance becomes the dominant resonance, a further increase of the transverse-field will also increase the slightly off-resonance transitions, which will, consequently, broaden the distribution and increase the width (Fig. 4.15). In chapter 5 we will present numerical calculations that support this interpretation. Although we do not observe the appearance of a new superimposed peak in our data,

we interpret the decrease of the width of the Lorentzian to be evidence of a new tunneling resonance becoming relevant to the dynamical process at hand. We speculate that a double Lorentzian is not observed due to inhomogeneous broadening caused, for example, by crystalline disorder [13].

Figure 4.13: We link the first group of Lorentzians (red circle) to a dominant tunneling resonant pair of levels. See text for further explanation.

However, in this simple picture of a transverse-field dependent relaxation process, it should be expected that, since tunneling is much less probable off-resonance, the relaxation rates should not depend so strongly, if at all, on the transverse-field. Following this interpretation one would predict that the steps should not occur in the off-resonance data. This puzzle was the primary incentive for some numerical and theoretical explorations, described in the next chapter, in which we produce a more in-depth analysis of the relaxation process. In the analysis, we observe off-resonance steps that occur for values of longitudinal-field that are similar to the the steps in the off-resonance data in Fig. 4.9.
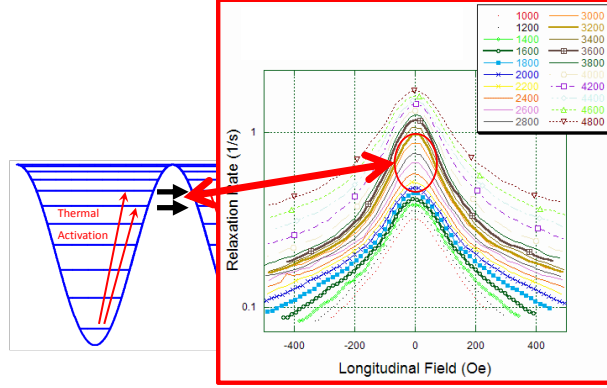
Figure 4.14: We link the second group of Lorentzians (red circle) to the appearance of a second dominant tunneling resonant pair of levels. See text for further explanation.

4.2 ACS Measurements

As explained in the previous chapter, one could use, in principle, the Arrhenius law (Eq. (3.1)) to determine the effective height of the barrier. In an attempt to achieve a higher temperature range, we performed ACS measurements at $4\ K$. We point out that the data presented in this section is, by no means, complete. Further measurements are required in order to better understand the differences between the ACS and real-time measurements.

For a fixed value of temperature, and transverse- and longitudinal-field we measure the frequency dependent magnetic susceptibility (Fig. 4.16). Fitting the imaginary and real Eqs. (3.5) components of the susceptibility, we can extract the value of the relaxation rates. As we did in the real-time relaxation experiments, we perform the ACS measurement for different longitudinal- and transverse-fields. For a fixed transverse-field we find that the longitudinal-field distribution fits well to a Lorentzian (Fig. 4.17). There are a few difficulties in
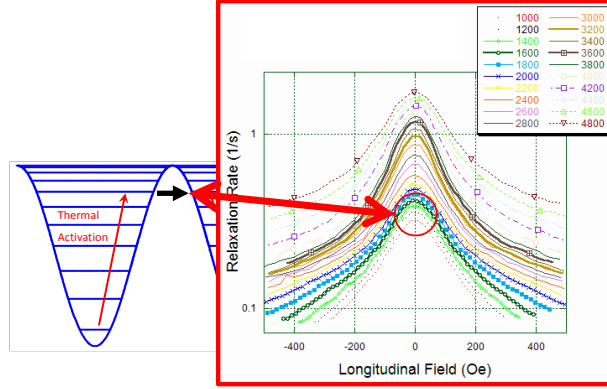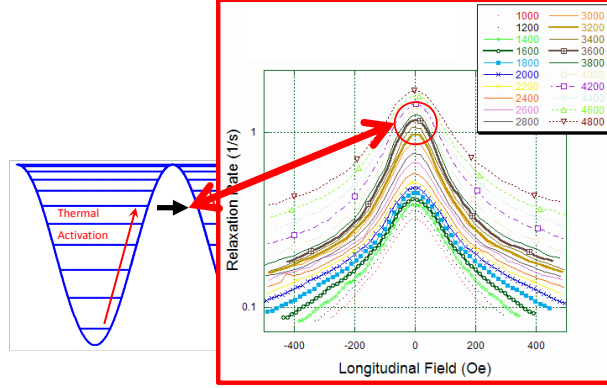
Figure 4.15: We link the third group of Lorentzians (red circle) to a new dominant resonant pair of tunneling levels. See text for further explanation.

performing ACS. The biggest problem is time. To capture the relaxation rate for an exponential in the real-time measurement, all we need to do is monitor the magnetization as a function of time. So, the time it takes to acquire that data point is, minimally, four to seven times the relaxation rate. To acquire the same data point using ACS, we have to map the entire frequency dependence. Plus, to measure each point in Fig. 4.16, we first apply the hall current one way, measure the susceptibility signal, reverse the current, measure the susceptibility again, and finally subtract both signals. Furthermore, we have to use a large integration time in the lock-in, usually in the order of 1 second, which requires at least 7 seconds to stabilize the signal. In practice, however, we have to wait an extra 30 seconds for the signal to stabilize. Considering the time it takes for each phase of the measurement to take place, the ACS method takes much longer than the real-time method. It does, however, allow us to measure faster relaxation rates over a wider range of temperatures.

The on-resonance data for the ACS method is plotted in Fig. 4.18. The
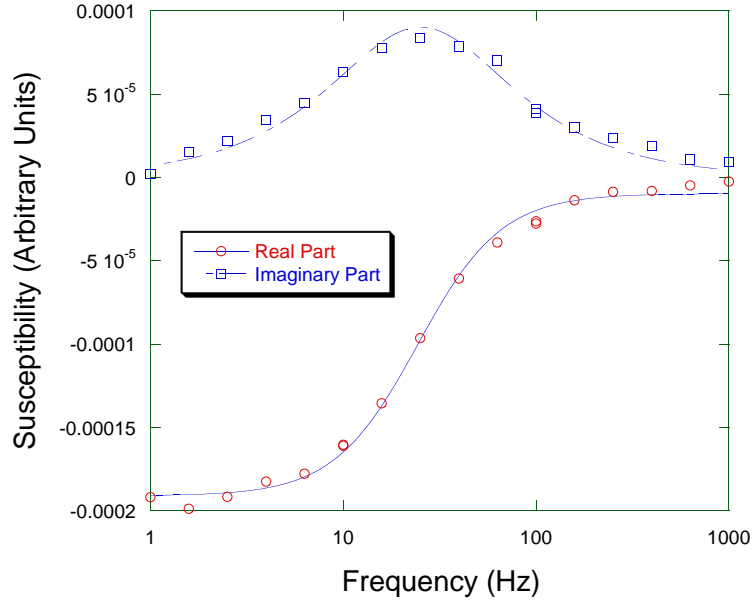
Figure 4.16: ACS measurement at 4.32(3) K, 3600 Oe transverse-field and zero longitudinal-field. Solid lines are best fit curves.
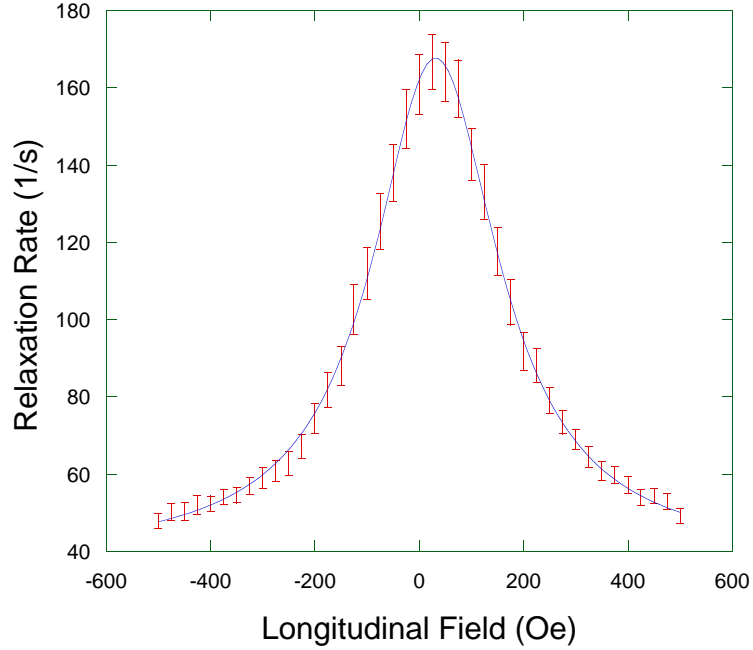
Figure 4.17: Longitudinal-field dependence of the relaxation rate for 3600 Oe transverse-field and 4.32(3) K.

steps that were present in Fig. 4.8 seem to have been washed out, perhaps by the higher temperatures. However, another hypothesis is that the ACS method measures an average of the relaxation rate for all molecules in a crystal. Suppose, for example, that there is a distribution of molecules, some which relax faster than others. If so, it is plausible that in the real-time measurements, we would observe a fast relaxation period, followed by a slower relaxation period. If there are more molecules relaxing fast than molecules relaxing slowly, for example, fitting the data to a single exponential will yield a faster relaxation rate, which is one possibility for the non-exponential behavior in Fig. 4.5. In the ACS method, we measure how the *total* magnetization follows the oscillating magnetic field and we look for the frequency at which $Im(\chi)$ and $dRe(\chi)/d\omega$ are both maximum. We would like to perform more ACS measurements to
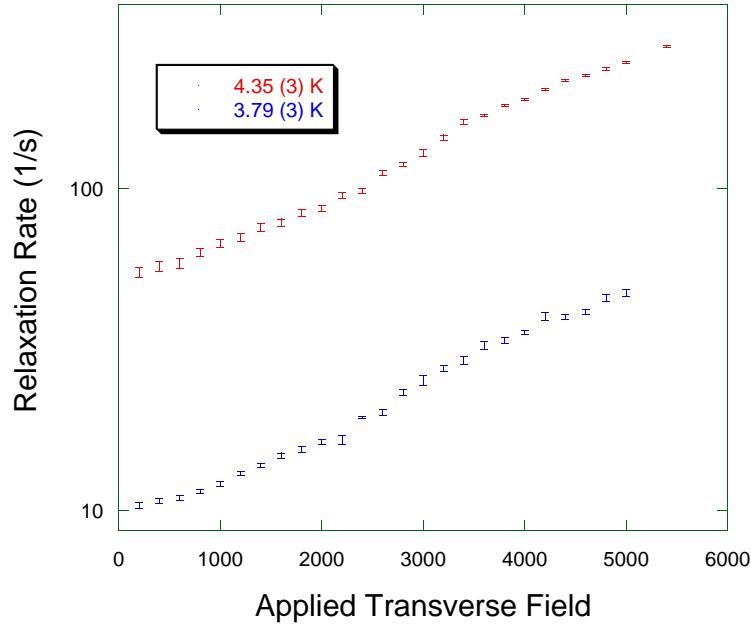
Figure 4.18: Transverse-field dependent on-resonance relaxation rates extracted via ACS measurements.

find out if we would be able to observe the same steps that can be seen in the real-time measurements.

4.3 $N = 1$ Resonance Experiments

The key to the $N = 1$ experiments, is the existence of the fourth order anisotropy term. As discussed in chapter 1, the fourth order anisotropy changes the resonance condition for different levels (see Fig. 1.5). If the height of the barrier is dominated by a pair of resonant levels, and if the longitudinal-field value for resonance varies from one pair of levels to the other, it is expected that an abrupt change in the height of the barrier should translate into an abrupt change of the longitudinal-field value for which a peak in the relaxation rate appears. Table 4.1 shows the possible $N = 1$ resonances with their respective longitudinal-field values. We performed real-time relaxation measurements and some of the Lorentzian distributions can be seen in Fig. 4.19.

As usual, we plot the relaxation rates on-resonance and off-resonance, as

m, n	Resonant Longitudinal-Field (Oe)
$2, -1$	4272
$3, -2$	4344
$4, -3$	4452
$5, -4$	4597
$6, -5$	4777
$7, -6$	4994
$8, -7$	5246
$9, -8$	5535
$10, -9$	5860

Table 4.1: $N = 1$ resonances with their respective longitudinal-field values.

well as the widths, all as a function of transverse-field in Figs. 4.20, 4.21 and 4.22. The extra information that the $N = 1$ resonance can supply us is the longitudinal-field value of the center peak. The transverse-field dependent values of the center of the Lorentzians can be seen in Fig. 4.23. Although the longitudinal-field value for the central peak increases, no abrupt changes
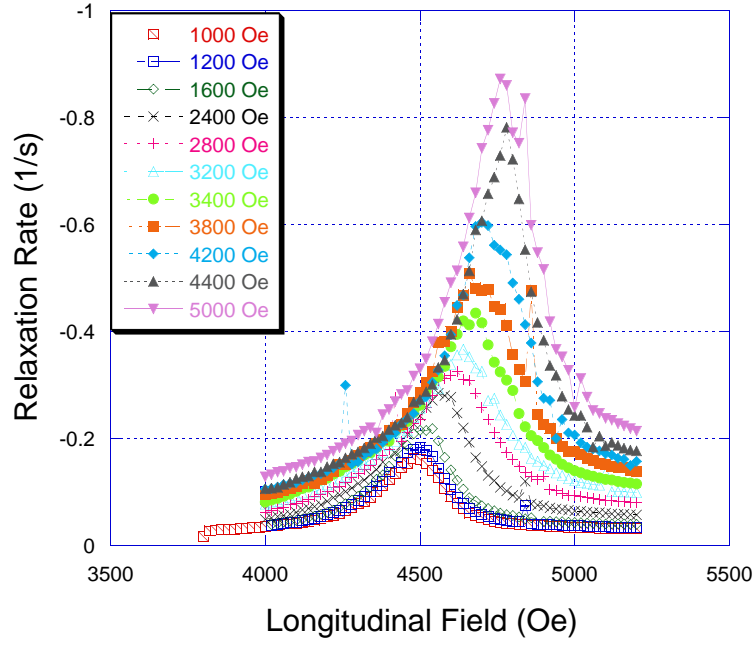
Figure 4.19: Longitudinal-field dependent relaxation rates for different transverse-fields at 2.87(3) K.
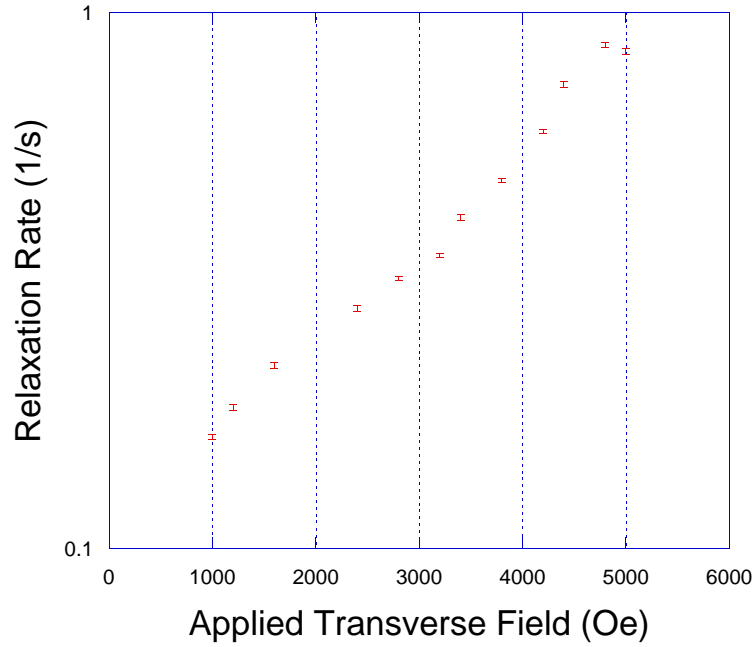
Figure 4.20: On-resonance relaxation rates as a function of transverse-field for the $N = 1$ resonance at 2.87(3) K.

57
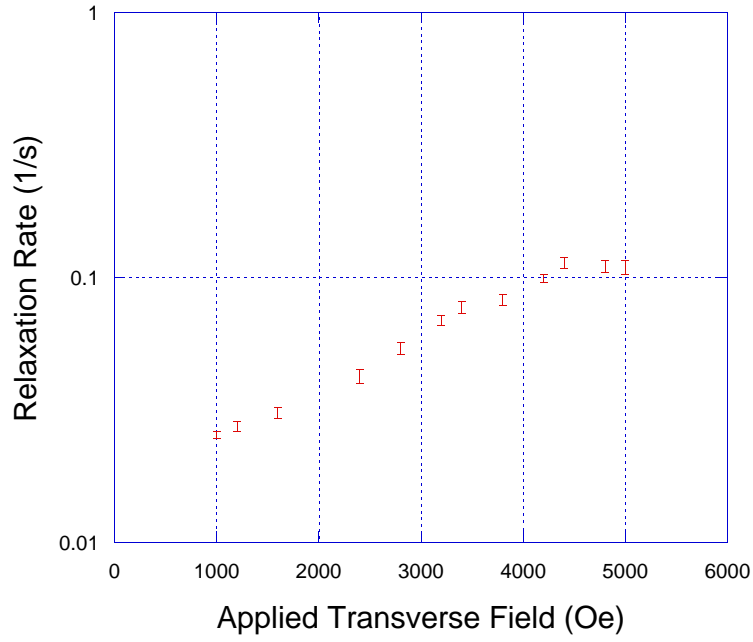
Figure 4.21: Off-resonance relaxation rates as a function of transverse-field for the $N = 1$ resonance at $2.87(3)$ K.
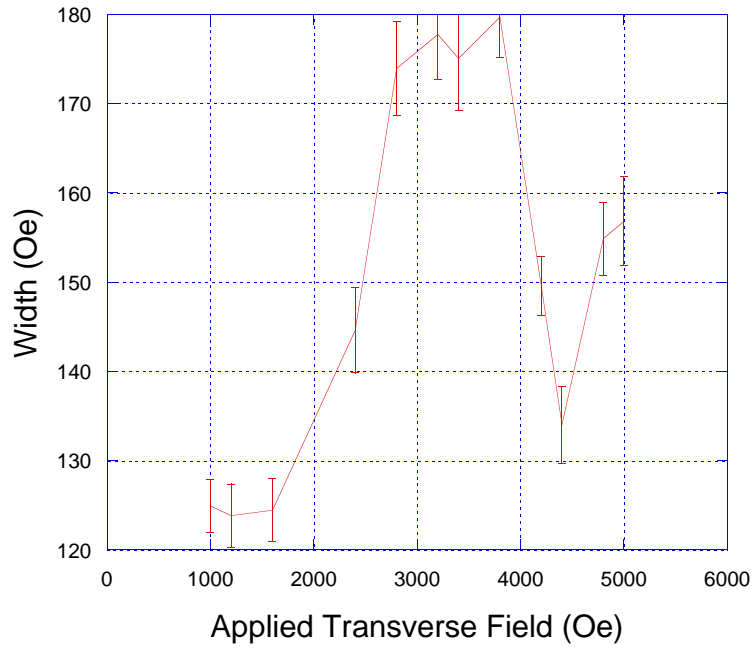
Figure 4.22: Lorentzian widths as a function of transverse-field for the $N = 1$ resonance at $2.87(3)$ K.
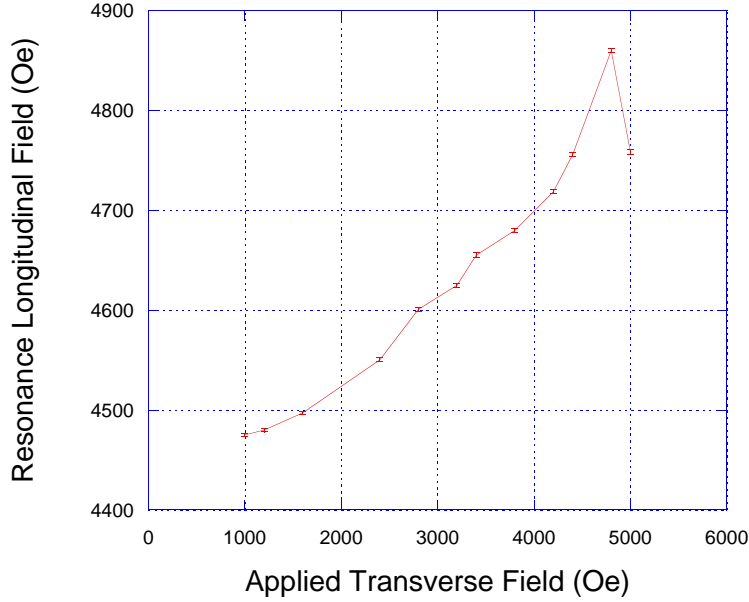
Figure 4.23: Transverse-field dependent values of the center of the Lorentzians at $2.87(3)$ K.

can be seen. The reliability of these data points is also questionable since we performed systematic tests that indicate that the rotator angle, for which the zero-resonance occurs, changes over different data acquisition runs. There is one obvious way to make sure the longitudinal-field is set correctly. For each sweep of the longitudinal-field near the $N = 1$ resonance, one could first calibrate the rotator by identifying the peak in the zero-field resonance.

4.4 Summary of Experimental Data

The most important experimental result of this section is, undoubtably, the appearance of steps in both the on-resonance and off-resonance transverse-field-dependent relaxation measurements. We interpret the steps to be due to abrupt changes in the dominant tunneling resonances for Mn_{12}-tBuAc.

Our interpretation is corroborated by the oscillations in the widths of the longitudinal-field-dependent relaxation rate distributions. We emphasize, however, that a better understanding of the off-resonance relaxation dynamics is necessary.

In chapter 5 we hope to answer some key questions. Do we have a theory that explains the appearance of the steps, both on- and off-resonance? Does the theory agree with our interpretation of the data? And, why are the steps sharper for the off-resonance relaxation rates than for the on-resonance rates? While, in the next chapter, we answer "yes" to the first two, we have not yet reached a solution to the third question.

Chapter 5

Theoretical Results

The motivation for the calculations presented in this chapter was the difficulty in understanding the appearances of plateaus and steps in the off-resonance relaxation data (Fig. 4.9). One semi-intuitive view of the barrier reduction process implies that, on-resonance, the height of the barrier can be defined as the energy difference between the ground state and where tunneling is occurring sufficiently fast[1]. Because the tunneling rate between any two resonant levels changes abruptly, one would expect resonant tunneling to be necessary for the observed transverse-field dependence of relaxation rates. This intuition does not, however, make sense in the off-resonance case, where *resonant* tunneling is much decreased and almost nonexistent. In order to gain a better understanding of the dynamical processes that would take the spins from one side of the barrier to the other, we follow a density matrix formalism approach, similar to the one employed by Garanin and Chudnovsky [17, 18], and, later on, Leuenberger and Loss [23, 24] with a few caveats. We use the energy eigenbasis instead of the m basis. This makes the application of Garanin's for-

---

[1]See section 2.2 and Eq. (2.14).

mula (Eq. (2.12)) for the near resonance tunnel splitting more difficult. This is not, however, an impediment for the off-resonance calculations since we don't expect *resonant* tunneling to occur. Notice that I am being careful about referring to the kind of tunneling caused by the oscillatory solutions due to the tunnel splitting as *resonant* tunneling. The reason for this distinction is that, as we will see in this chapter, defining what tunneling is can be hard and ambiguous. So, another instance where we differ from the aforementioned studies, is that we do not insert the *resonant* tunneling rate from m to m', induced by the tunnel splitting, in our calculations.

I will first introduce the density operator (sometimes called the statistical operator) and some of its key properties but I will, by no means, fully develop density matrix theory[2].

5.1 Density Matrix Theory [1]

5.1.1 The Density Operator and the Density Matrix

In quantum mechanics a given system is represented as a state vector $|\psi\rangle$ which can be written as a linear superposition of eigenstates $|\phi_n\rangle$ of a given operator Q (or a set of operators Q_i):

$$|\psi\rangle = \sum_n a_n |\phi_n\rangle.$$ (5.1)

---

[2]Since most results in the next section are from Blum's book on Density Matrix Theory, it seemed more appropriate to reference the entire section instead of particular results.

We will also assume the eigenstates to be orthonormal and complete:

$$\langle\phi_n|\phi_m\rangle = \delta_{mn} \ , \tag{5.2}$$

$$\sum_n |\phi_n\rangle \langle\phi_n| = 1 \ . \tag{5.3}$$

Consequently, the a_n coefficients are given by $a_n = \langle\phi_n|\psi\rangle$. And we can also normalize the states by

$$\sum_n |a_n|^2 = 1 \ . \tag{5.4}$$

In this representation, $|a_n|^2$ gives the probability of finding the system in the nth state.

Suppose the observable Q for which $|\psi\rangle$ is not an eigenstate. A measurement of Q can collapse the state into any of its eigenstates $|\phi_n\rangle$. If we performed the measurement on a large ensemble of particles, all prepared in the $|\psi\rangle$ state, and then averaged over the values, we would obtain the expectation value $\langle Q\rangle$ for the observable:

$$\langle Q\rangle = \langle\psi|Q|\psi\rangle \ . \tag{5.5}$$

The statistical nature of this expectation value is a prediction of quantum mechanics[3]. There is another way statistics can come into play when considering an ensemble of particles. Suppose that each particle can be in a different $|\psi_n\rangle$ with *classical* probability W_n. To obtain $\langle Q\rangle$ for a mixture of particles in different quantum states, we will have to properly treat *both* statistical natures of the system. The value of the expectation value is therefore:

$$\langle Q\rangle = \sum_n W_n\langle\psi_n|Q|\psi_n\rangle \ . \tag{5.6}$$

---

[3]It may be due to perturbation of the system caused by a measurement, although this is part of the *measurement problem*, and is open for debate.

This second type of averaging is the kind that is done in statistical mechanics and it leads to the density matrix operator (sometimes called the statistical operator), defined by:

$$\rho = \sum_n W_n |\psi_n\rangle \langle\psi_n| \ . \tag{5.7}$$

It is much more convenient to express the operator in matrix form. Using an appropriate basis $|\phi_m\rangle$, we can write each element of the mixture as:

$$|\psi_n\rangle = \sum_{m'} a_{m'}^{(n)} |\phi_{m'}\rangle \tag{5.8}$$

$$\langle\psi_n| = \sum_m a_m^{(n)*} \langle\phi_m| . \tag{5.9}$$

The next step is to insert Eqs. (5.8) and (5.9) into Eq. (5.7) to get

$$\rho = \sum_{nm'm} W_n a_m^{(n)*} a_{m'}^{(n)} |\phi_{m'}\rangle \langle\phi_m| , \tag{5.10}$$

and then take the matrix elements, making use of the orthonormality conditions, to obtain

$$\langle\phi_i|\rho|\phi_j\rangle = \sum_n W_n a_j^{(n)*} a_i^{(n)} . \tag{5.11}$$

This is the density matrix, and it operates on the space spanned by the $|\phi_n\rangle$ basis.

Since the probability of finding the state in $|\psi_n\rangle$ is given by W_n *and* the probability of finding $|\psi_n\rangle$ in the basis-state $|\phi_m\rangle$ is $|a_m^{(n)}|^2$, we find that

$$\rho_{mm} = \sum_n W_n |a_m^{(n)}|^2 \tag{5.12}$$

gives the probability of finding the system in state $|\phi_m\rangle$.

The density matrix has several other properties but I will only mention them if necessary. The interested reader is encouraged to seek a more detailed approach elsewhere [1, 25].

64

5.1.2 Time Evolution of the Density Matrix

The time evolution of a quantum state is described by the Schröndinger equation (SE):

$$i\hbar \frac{\partial |\psi(t)\rangle}{\partial t} = \mathcal{H} |\psi(t)\rangle .$$ (5.13)

And it is a standard textbook result that if $\mathcal{H}$ is *time independent*, the state will evolve according to

$$|\psi(t)\rangle = e^{-(i/\hbar)\mathcal{H}t} |\psi(0)\rangle ,$$ (5.14)

where the exponential operator is well defined by its Taylor expansion:

$$e^{-(i/\hbar)\mathcal{H}t} = 1 - \frac{i}{\hbar}\mathcal{H}t - \frac{1}{2\hbar^2}\mathcal{H}^2 t^2 - \cdots .$$ (5.15)

The SE equation is not sufficient to describe the time evolution of a mixture. Suppose that at $t = 0$ the density operator is

$$\rho(0) = \sum_n W_n |\psi(0)_n\rangle \langle\psi(0)_n| .$$ (5.16)

We know that the states $|\psi(t)_n\rangle$ vary according to the SE (Eq. (5.13)), which implies that the density operator is also time dependent:

$$
\begin{aligned}
\rho(t) &= \sum_n W_n |\psi(t)_n\rangle \langle\psi(t)_n| \\
&= \sum_n W_n U(t) |\psi(0)_n\rangle \langle\psi(0)_n| U(t)^\dagger \\
&= U(t)\rho(0)U(t)^\dagger.
\end{aligned}
$$ (5.17)

Here, $U(t)$ is the time evolution operator $(|\psi(t)\rangle = U(t) |\psi(0)\rangle)$, and if we plug this last expression back in Eq. (5.13) we obtain

$$i\hbar \frac{\partial U(t)}{\partial t} = \mathcal{H}(t)U(t) \text{ and}$$ (5.18)

$$-i\hbar \frac{\partial U(t)^\dagger}{\partial t} = U(t)^\dagger \mathcal{H}(t).$$ (5.19)

Differentiation of Eq. (5.17), together with Eqs. (5.18) and (5.19), yields

$$i\hbar\frac{\partial\rho(t)}{\partial(t)} = i\hbar\frac{\partial U(t)}{\partial t}\rho(0)U(t)^\dagger + i\hbar U(t)\rho(0)\frac{\partial U(t)^\dagger}{\partial t}$$
$$= \mathcal{H}(t)U(t)\rho(0)U(t)^\dagger - U(t)\rho(0)U(t)^\dagger\mathcal{H}(t)$$
$$= [\mathcal{H}(t), \rho(t)], \tag{5.20}$$

where in the last step we made use of Eq. (5.17) to obtain the so called *Liouville equation* (Eq. (5.20)). The dynamic equations for the observables are found as simultaneous solutions to Eqs. (5.13) and (5.20).

5.1.3   Master (Rate) Equations

In the last two sections I have tried to develop the basic properties of the density matrix. Hopefully this brief treatment will give the reader who is not familiar with the subject, an intuition of the basic theory. The key ideas I hope the reader will keep in mind are, one, that the density matrix is a *statistical* operator, and, two, it operates on the basis of the system of interest, decoupled from the thermal bath. Keeping these properties in mind, I will now make a large leap in reasoning and discuss one of the most useful results of the theory: the *Pauli master equation.*

If the system is not closed, but, instead, in contact with a large reservoir, with which it exchanges energy, then, we must consider the Hamiltonian of the system, plus the Hamiltonian of the reservoir, and also the interaction Hamiltonian. We want to be able to determine the dynamics of a system that starts in a nonequilibrium state and then evolves, via an *irreversible* process, into an equilibrium state that is defined by external conditions. This is a very general behavior of a system, and is called a *relaxation process*. The problem with the fundamental dynamical equations (Eqs. (5.13) and (5.20)) is that

they are *reversible* and would not be able to describe a relaxation process which is inherently *irreversible*.

In order to obtain irreversible dynamic equations we will have to impose two restrictions. First, we will assume that the reservoir (R) has so many degrees of freedom that any interactions with the system (S) will not have any effects on it (R), and will therefore not act back on the system (S). We assume the transformation

$$\rho(t)_{S+R} \longrightarrow \rho(t)_S \rho(0)_R, \tag{5.21}$$

in which we have factored out the density matrix of the reservoir, and assumed it to be time independent. This is the basic condition for irreversibility. Secondly, we will assume that the past history of the system's dynamics is destroyed by damping caused through its contact with the reservoir[4].

With these two assumptions and the necessary Markoff approximation[5], we find the very useful rate equation

$$\dot{\rho}(t)_{mm} = \sum_{n \neq m} \rho(t)_{nn} W_{mn} - \rho(t)_{mm} \sum_{n \neq m} W_{nm}. \tag{5.22}$$

This is the *Pauli master equation*. From our previous discussion (see Eq. (5.12)), we know that $\rho(t)_{mm}$ gives the probability of measuring the system in a given basis state $|\phi_m\rangle$. We can interpret this equation as follows. The first term on the RHS of Eq. (5.22) gives all the transitions that will increase the population of the $|\phi_m\rangle$ state. It is obtained by the product of the population of another

---

[4]Damping is usually related to loss of information. Think of a particle undergoing free fall under the influence of viscous friction. It will achieve a final velocity that does not depend on the initial conditions of the system. It is therefore impossible to trace the particle's motion back to its initial state: information has been lost.

[5]The Markoff Approximation and details are discussed by Blum [1]. It basically consists of a "coarse-grained" derivative taken over time intervals Δt long compared to the time of free oscillations of the system.

level, n, with the rate W_{mn} for the transition from $|\phi_n\rangle$ to $|\phi_m\rangle$, summed over all n. The second term is due to all the processes that will decrease the population of the $|\phi_m\rangle$ state: it is just the population of the $|\phi_m\rangle$ state times the rates (W_{nm}) for transitions taking particles from the $|\phi_m\rangle$ to $|\phi_n\rangle$, summed over all n. Thus, the key to understand the dynamics of the system is to find the parameters W_{mn}, which represent the probability per unit time that a transition between the basis states will occur due to the interactions with the reservoir. Notice that Eq. (5.22) is a matrix equation:

$$\dot{\vec{\rho}} = \widetilde{W} \vec{\rho}(t), \tag{5.23}$$

where $\vec{\rho}$ is a column vector representing the relative populations of a given state, and $\widetilde{W}$ is called the rate matrix.

5.2   Numerical Simulations

We have performed several numerical calculations to better understand the relaxation dynamics of Mn$_{12}$-tBuAc. I will separate the calculations under three sections. First, I will describe the calculations to find the relaxation rate of magnetization as a function of transverse field. Secondly, I will address the longitudinal field (H_z) dependence on the relaxation rate. Thirdly, I will show calculations that determine the height of the anisotropy barrier by finding the path of highest probability for a molecule starting at the left well and relaxing to the ground state in the right well.

Because of the lack of time, we were not able to fit our numerical calculations to the experimental data. Furthermore, we have only done these calculations for $T = 3\ K$, and it shall be assumed that all results shown from now on have been calculated for $3\ K$.

5.2.1   The Transition Coefficients

The key to all these calculations is the rate matrix in Eq. (5.23). We calculate the W_{mn} transition coefficients using the expressions obtained by Garanin and Chudnovsky [17] (given in the m basis):

$$W_{m\pm 1,m} = \frac{D^2 s_{\pm 1}}{12\pi\rho c^5 \hbar^4} \frac{(\epsilon_{m\pm 1} - \epsilon_m)^3}{e^{\beta(\epsilon_{m\pm 1} - \epsilon_m)} - 1}, \tag{5.24}$$

where $s_{\pm 1} = (s \mp m)(s \pm m + 1)(2m \pm 1)^2$, $\rho = 1.93 \times 10^3 \ kg/m^3$ [5] is the mass density for Mn_{12}, ϵ_m is the energy of the $|m\rangle$ state, and $c = 1.40 \times 10^3 \ m/s$ [23] is the speed of sound in Mn_{12}. This result is for the $|m\rangle$ basis[6]. To perform our calculations we have to change Eq. (5.24) from the $|m\rangle$ basis to the energy basis, $|E_i\rangle$.

To adapt Eq. (5.24) to the energy basis, $|E_i\rangle$, we can follow the derivation presented by Leuenberger and Loss [23][7] and identify where the $s_{m-1,m}$ terms come from. We find that

$$s_{\pm 1} = |\langle s, m \pm 1|(S_+ S_z + S_z S_+ + S_- S_z + S_z S_-)|s, m\rangle|^2 , \tag{5.25}$$

which the reader can check and see that it agrees with the result in the $|m\rangle$ basis. The action of the raising and lowering operators is

$$S_\pm |s, m\rangle = \sqrt{(s \mp m)(s \pm m + 1)} \, |s, m \pm 1\rangle . \tag{5.26}$$

The ϵ_i terms are replaced by the eigenenergies and are easily computed in the energy basis by $\langle E_i|\mathcal{H}|E_i\rangle$.

---

[6]Leuenberger and Loss [23] also calculated a $\Delta m = 2$ transition rate, but an error in their calculations was pointed out by Chudnovsky and Garanin [26]. The topic has been under debate [27], but there have been experimental results [28] against the existence of this $\Delta m = 2$ phonon transition. In all our calculations we have discarded the use of $W_{m\pm 2,m}$.

[7]Although, as mentioned before, Eq. (5.24) and its derivation was first presented by Garanin and Chudnovsky in [17].

The Hamiltonian in Eq. (1.8) is

$$\mathcal{H} = -DS_z^2 - BS_z^4 - g\mu_B \vec{H} \cdot \vec{S} \,. \qquad (5.27)$$

For $H_x \neq 0$, $\mathcal{H}$ and S_z will not commute and the energy basis will differ from the m basis. But that does not prevent us from writing the elements of the energy basis in terms of the m basis:

$$|E_n\rangle = \sum_m a_{nm} |m\rangle \,. \qquad (5.28)$$

This freedom to choose a basis allows us to freely operate $S_\pm$ on the $|E_n\rangle$ states.

We have all the information we need to write the $\tilde{W}$ rate matrix. The transition coefficients W_{ij}[8] are

$$W_{ij} = \frac{D^2 \left| \langle E_i | (S_+ S_z + S_z S_+ + S_- S_z + S_z S_-) | E_j \rangle \right|^2}{12\pi\rho c^5 \hbar^4} \frac{(E_i - E_j)^3}{e^{\beta(E_i - E_j)} - 1}, \qquad (5.29)$$

where E_i is the energy of the $|E_i\rangle$ state.

In our Mathematica code, we construct the matrix representation of the Hamiltonian and find its eigenvalues and eigenstates, which we use as our basis. The Hamiltonian (Eq. (1.8)) is dependent on the magnetic field $\vec{H}$ and we therefore have to construct a basis set for each value of field for which we want to do the calculation. We then construct the $\widetilde{W}$ rate matrix according to Eq. (5.29).

---

[8]The W_{ij} coefficients are not the elements of the rate matrix, but from those it becomes trivial to write $\tilde{W}$ using Eq. (5.22).

5.2.2 Relaxation Rates

To find the dominant relaxation rate, we diagonalize the rate matrix $\widetilde{W}$ and identify the lowest nonzero eigenvalue. We find it to be far removed from the other eigenvalues by several orders of magnitude. Considering that, for Mn$_{12}$-tBuAc, $\widetilde{W}$ operates on a 21 dimensional space, this is not a very hard computational problem. The general solution to the system of equations is a sum of exponentials. In all solutions we find one of the eigenvalues to be zero. This is because one of the eigenvectors of $\widetilde{W}$ is a vector $\vec{\rho}^{(*)}$ representing the sum of the populations of all states. But since the total population is a conserved quantity, $0 = \dot{\vec{\rho}}^{(*)} = \widetilde{W}\vec{\rho}^{(*)}$, yielding the existence of the zero eigenvalue. All other decays occur at their characteristic rates and one is much slower than the others, leading to an exponential decay after some initial fast dynamics. Figure 5.1 shows the relaxation rate as a function of transverse-field at $H_z = 5\ Oe$, close to resonance and at $H_z = 1000\ Oe$ and $H_z = 500\ Oe$, off-resonance. A nonzero value for H_z is necessary when calculating the elements of $\widetilde{W}$, otherwise the matrix element Mathematica numerically evaluates, between two near degenerate states would blow up. For $H_z = 0$, and levels near degeneracy, the denominator in Eq. (5.29) is $\exp(\varepsilon/\beta) - 1 \approx \varepsilon/\beta$, where we let the energy difference between the two states be ε. So the dependence of Eq. (5.29) becomes $\varepsilon^3/\varepsilon = \varepsilon^2$. But when we do this calculations, Mathematica numerically evaluates a vanishing denominator and the matrix element blows up (although we know it should converge).

On-resonance, we interpret the plateaus to occur for transverse fields where the height of the barrier is well defined by resonant levels in opposite wells. As mentioned in the beginning of this chapter, this interpretation does not seem to be valid for the off-resonance measurements. However, we do observe the
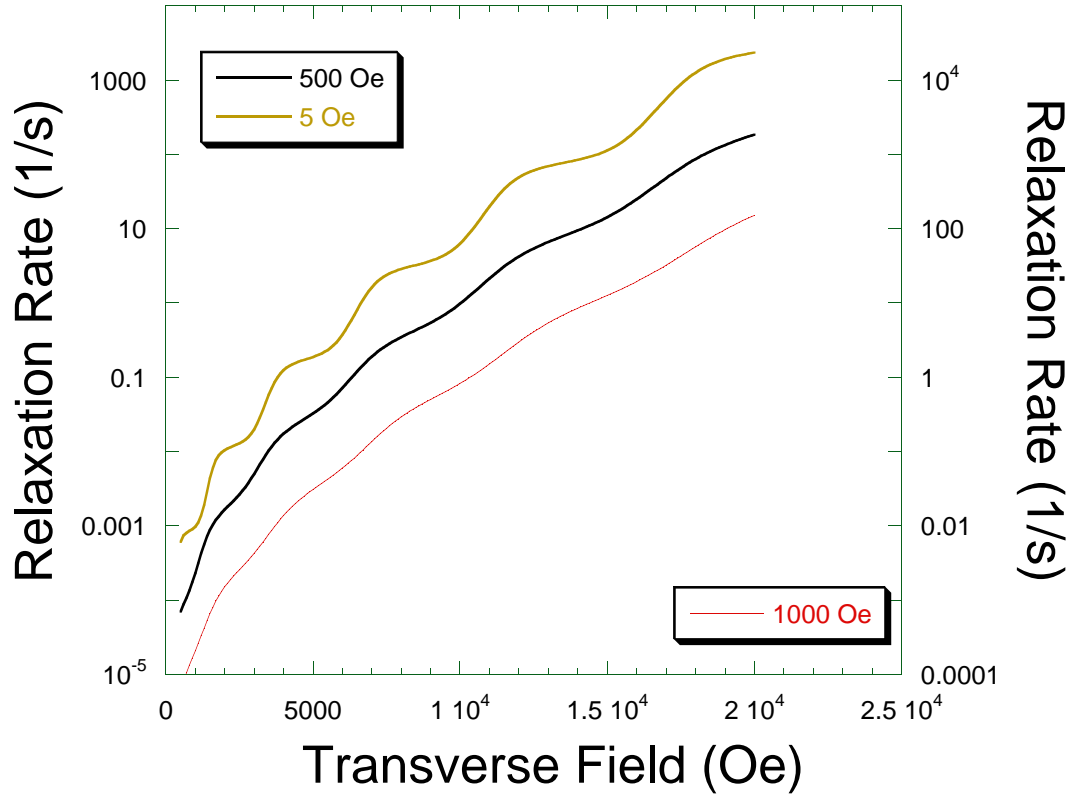
Figure 5.1: Transverse-field dependent relaxation rate for different longitudinal-fields — on-resonance (5 Oe) and off-resonance (500 Oe and 1000 Oe). The 1000 Oe is plotted on a separate scale (right) for clarity.

72

plateaus and steps on the off-resonance numerical curves in Fig. 5.1, where we note that the features are very weak in the 1000 Oe data.

Through these calculations we can also observe the longitudinal field (H_z) dependence of the relaxation rates. Figure 5.2 shows the longitudinal-field dependent distributions of relaxation rates for different transverse fields. In
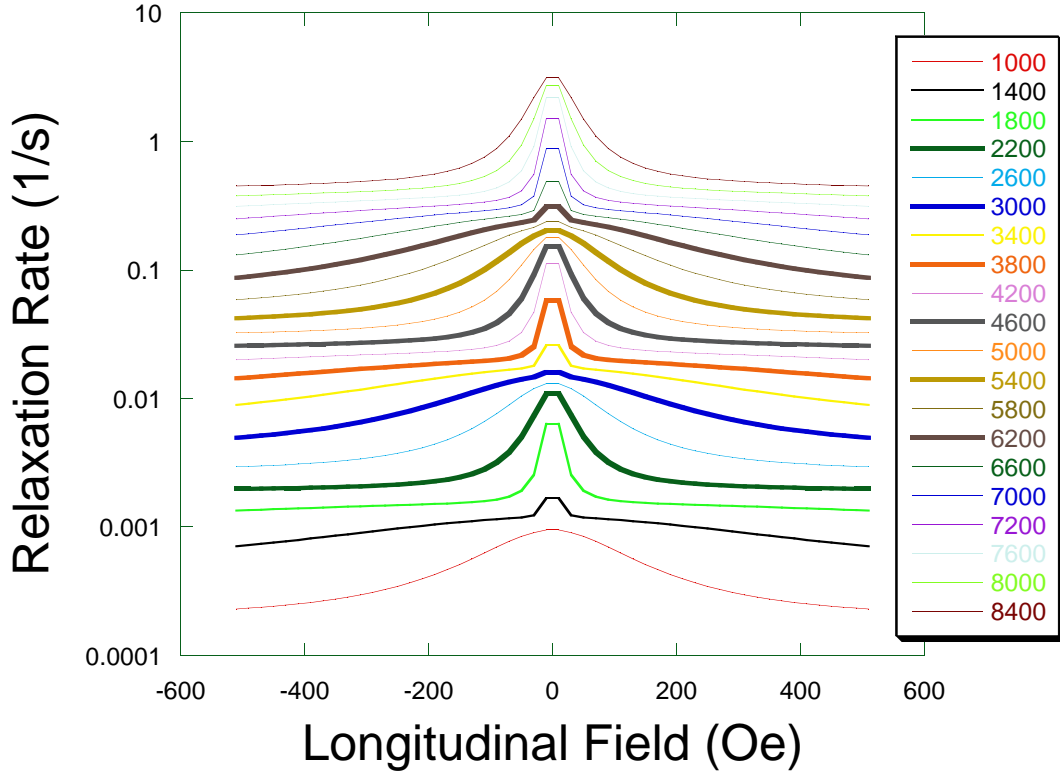
Figure 5.2: Longitudinal-field dependent relaxation rates for different transverse-fields (Oe).

Fig. 5.1 we can see the same behavior presented in our data (Fig. 4.12). The steps on-resonance (Fig. 5.1) can be associated with the superposition of Lorentzians as the transverse field is varied (Fig. 5.2). Figure 5.3 shows the transverse-field dependent relaxation rates, on-resonance, for a smaller range and the Lorentzian curves (inset). The appearance of steps at $H_T =$

1400, 3400, and 6200 *Oe* coincides with the appearance of a sharp superimposed peak on top of the next lower Lorentzian.
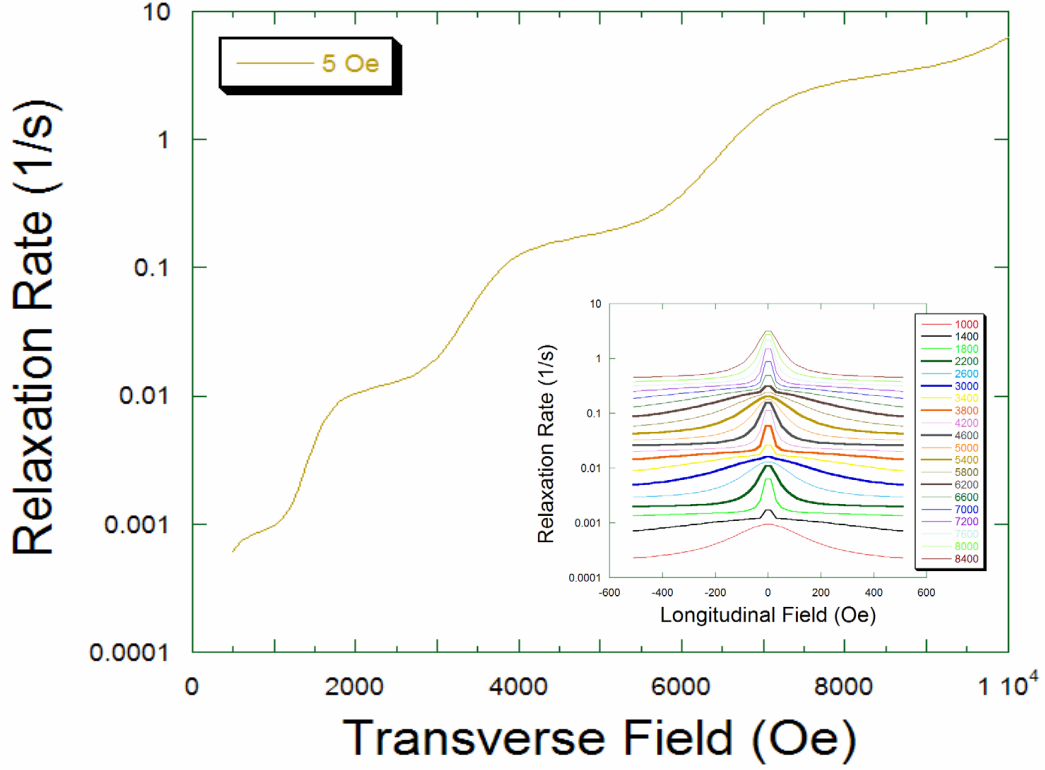
Figure 5.3: Transverse-field dependent relaxation rate on-resonance, and longitudinal-field dependent relaxation rates for different transverse-fields (Oe) (inset).

These results qualitatively agree with our measurements but it is worth noting that as we go off-resonance in the simulations, the steps become less sharp. The opposite behavior is seen in the experimental data.

5.2.3 Dominant Relaxation Paths

To determine the dominant relaxation path a spin can take to rotate its orientation from up to down, we need a way to quantify how probable a given transition is. So, we construct the probability currents [29] for transitions between $|E_i\rangle$ and $|E_j\rangle$:

$$J_{i,j} = P_j W_{ij} - P_i W_{ji}, \tag{5.30}$$

where P_i is the population of the $|E_i\rangle$ state. This equation can be interpreted as the gain in P_i due to transitions *from* $|E_j\rangle$ minus the loss in P_i due to transitions *to* $|E_j\rangle$. We already know how to calculate the elements of the rate matrix; to find the populations we can use the Pauli Master equation (Eq. (5.22)), which determines the relative population of each state. For Mn_{12}-tBuAc, this vector equation consists of a system of 21 first order linear differential equations, which is not a hard task for Mathematica to solve. Our simple set of initial conditions is to have the lower ground state fully populated (i.e. $P_1 = 1$) and all the other levels depopulated ($P_j = 0 \; \forall j : 2 \leq j \leq 21$). Numerical solutions for the time dependent populations are calculated using the NDSolve routine in Mathematica. In principle, this set of 21 differential equations could be solved analytically, but the analytical solutions would not add any insight to the problem at hand, and would demand more computational power[9]. From the population, not only can we construct the probability currents, but we can also find the magnetization (M) and the rate of change in magnetization ($\dot{M}$) as follows:

$$M = \sum_n P_n \langle E_n | S_z | E_n \rangle \tag{5.31}$$

$$\dot{M} = \sum_n \dot{P}_n \langle E_n | S_z | E_n \rangle. \tag{5.32}$$

---

[9]Or manpower!

We observe the magnetization to decay exponentially (Fig. 5.4), in accordance with experiments.
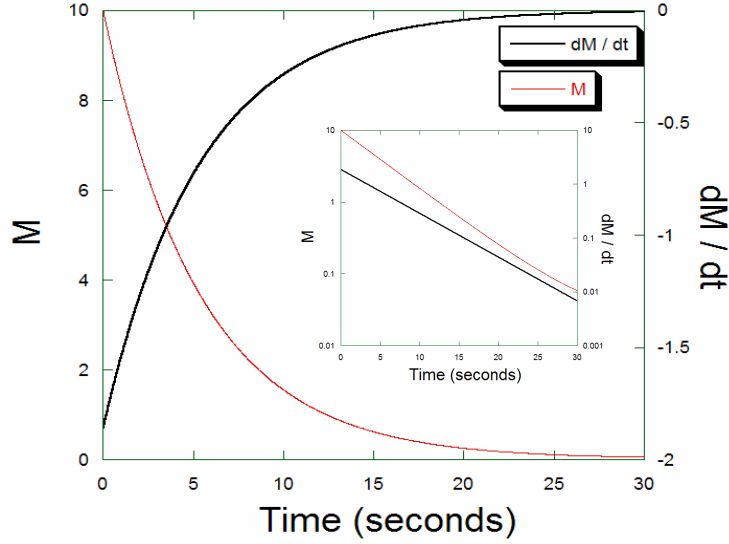
Figure 5.4: Decay of M and $\dot{M}$. M and $|\dot{M}|$ appear as straight lines on a log scale (inset), which suggests exponential decay.

We have all the information we need to calculate the probability currents, but what properties do they have? Suppose we have a simple four state system, two ground states ($|E_1\rangle$ and $|E_2\rangle$) and two excited states ($|E_3\rangle$ and $|E_4\rangle$). Figure 5.5 shows two possible transition paths. The first path (1) is a direct transition path between the ground states. The second path (2) consists of a particle on the first level being excited to $|E_3\rangle$ and then transitioning to the other ground state. Other possible paths are not shown in the figure. There is one simple rule these probability currents must follow. In the steady state, the sum of all incoming currents must equal the sum of all outgoing currents for a given level. This rule [23] is analogous to Kirchoff's current law and it is
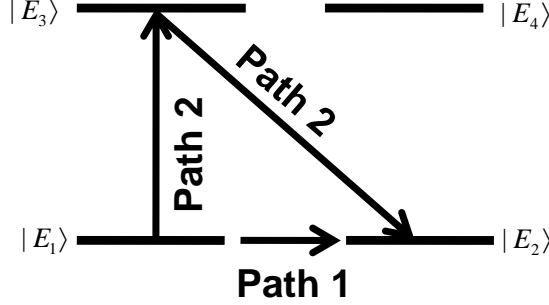
Figure 5.5: Two possible transition paths for a simple four-state system.

summarized in the following equation:

$$\sum_m J_{n,m} = 0. \tag{5.33}$$

The initial dynamics of the system is fairly complicated, since the entire population starts at the lowest energy level in the left well, and then it takes some initial time to spread out to other levels. We dismiss the initial dynamics and analyze the probability currents in the long-time domain. We numerically find the time τ_M for which the magnetization, M, has decayed by a factor of e. And we then define the long time domain to be $7\tau_M$.

We divide the currents by $\dot{M}$ in the long-time domain, since they both have units of $1/[time]$. We find that the *range* of values that $J_{m,n}/\dot{M}$ takes is independent of transverse-field. This means that a fast probability current for a given transverse-field is also a fast current for a different transverse-field, which makes their comparison easy. We construct a long-time domain,

time-independent, probability current

$$\bar{J}_{m,n} = \frac{J_{m,n}(\tau_M)}{\dot{M}(\tau_M)}, \tag{5.34}$$

and, from now on, whenever I refer to probability currents, it shall be assumed that I mean $\bar{J}_{m,n}$.

Once all these calculations are done, our Mathematica code draws a diagram with all the energy levels and relevant currents (see Fig. 5.6). A lower bound for the probability currents that are allowed to be drawn in the diagrams has been chosen empirically. In the diagrams, the color of the arrows represents the relative value of the probability current. The intensity of the transition can be translated from the logarithmic scale (see Fig. 5.7)[10] on the right bottom corner.

The levels are chosen to be displayed on the left if they have expectation value $\langle E_i | S_z | E_i \rangle \geq 0.2$, on the right if $\langle E_i | S_z | E_i \rangle \leq 0.2$, or in the middle otherwise. The expectation values for each energy level are displayed on the diagrams. For some energy levels, the expectation values are still pretty close to the m eigenvalues of the S_z operator. If the transverse field H_x is zero, then $\mathcal{H}$ and S_z commute and the energy basis is the $|m\rangle$ basis. We can imagine that in the limit of $H_x \ggg H_z$, the $H_x S_x$ Zeeman coupling term will dominate the dynamics and the eigenstates of S_x will form a basis that commutes with $\mathcal{H}$: the "good" basis. In this case $\langle E_i | S_z | E_i \rangle \approx \langle m^x | S_z | m^x \rangle = 0$, where $|m^x\rangle$ are the eigenstates of the S_x operator. Because of the second and fourth order anisotropy terms, the Zeeman coupling term will dominate the dynamics for levels close to the top of the barrier (small m^2 and m^4) before it dominates

---

[10]Despite new improvements in version 6, Mathematica is not an ideal software for generating graphics, and plotting the numerical scale with the legend (and all the arrows) on the same graph turned out to be a hard task.
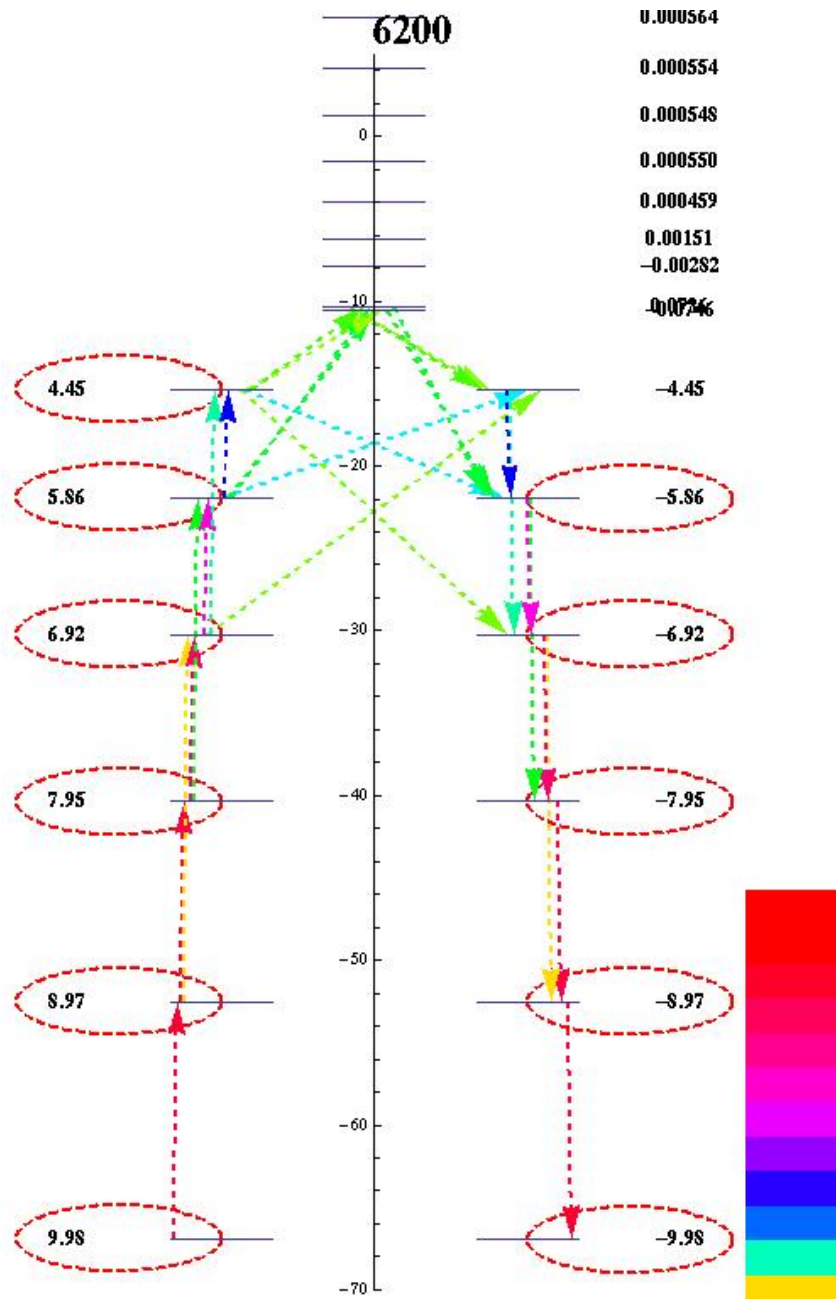
Figure 5.6: Probability currents for $H_z = 5 \; Oe$ and $T = 3K$. $H_T = 6200 \; Oe$ as indicated on the top of the diagram. The color of the arrows represent the relative intensity of the currents, according to the legend on the bottom right corner. The central vertical axis gives the energy, in kelvins, relative to the top of the anisotropy barrier.

5.5×10^{-2}
4.975×10^{-2}
4.45×10^{-2}
3.925×10^{-2}
3.4×10^{-2}
2.875×10^{-2}
2.35×10^{-2}
1.825×10^{-2}
1.3×10^{-2}
7.75×10^{-3}
2.5×10^{-3}
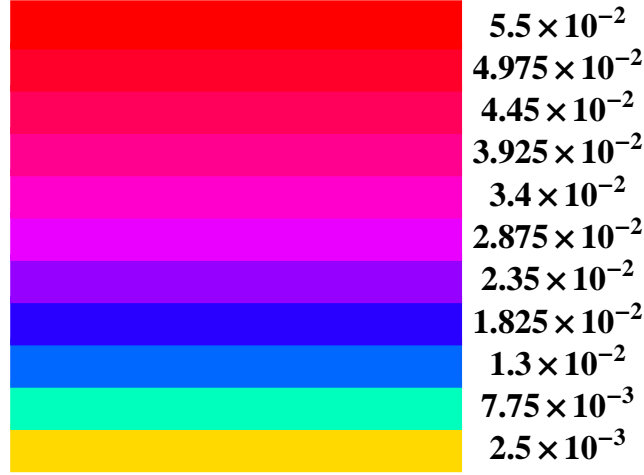
Figure 5.7: Color scale for the intensity of the currents for all diagrams to appear in thesis.

levels close to the ground state.

The expectation values of S_z give valuable information about the eigenstates of $\mathcal{H}$. It gives the degree to which a level is mixed. If $\langle E_i | S_z | E_i \rangle \approx m$, then $|E_i\rangle$ is also well described as an eigenstate of S_z. But if not, then the $|E_i\rangle$ state is better described as a superposition of $|m\rangle$ states. When the expectation value is zero, the $|E_i\rangle$ state is in a superposition of $|\pm m\rangle$ for $0 \leq m \leq 10$ (i.e. $|E_i\rangle$ is well described by an eigenstate of S_x). We say that a given level is delocalized when its expectation value becomes close to zero, and localized when $\langle E_i | S_z | E_i \rangle \approx m$. Accordingly, if a level is delocalized, its corresponding energy level is drawn in the middle of the diagram, since it cannot be identified with either well.

In Fig. 5.6 we observe some transitions that seem to have $\Delta m \neq 1$. This can be a little troublesome, especially because when we constructed the rate matrix, we only allowed the $\Delta m = 1$ transitions. But the values displayed in the diagrams are just average values of $\langle S_z \rangle$. Since we are working in the

energy basis, $|E_i\rangle$ is a superposition of $|m\rangle$ states. A transition from $|E_i\rangle$ to $|E_j\rangle$ on opposite sides of the barrier does not actually violate conservation of angular momentum. What happens is a transition from one $|m \pm 1\rangle$ state to a $|m\rangle$ state, but we only see the transitions between the energy basis states. We can see why the matrix element between different energy eigenstates can be nonzero by writing $|E_i\rangle = \sum_{n=-10}^{10} a_n^{(i)} |i\rangle$ (i.e. a superposition of $|m\rangle$ states) and inspection of the matrix element in Eq. (5.29):

$$\langle E_i | S^* | E_j \rangle = \left(\sum_{n=-10}^{10} a_n^{(i)} \langle n| \right) S^* \left(\sum_{m=-10}^{10} a_m^{(j)} |m\rangle \right), \qquad (5.35)$$

where $S^* = S_+ S_z + S_z S_+ + S_- S_z + S_z S_-$. Since all terms in S^* contain raising and lowering operators, only products between $\langle m|$ and $S^* |m \pm 1\rangle$ will survive (using the orthogonality of the basis). But as long as $a_n^{(i)}$ and $a_{n\pm1}^{(j)}$ are nonzero, the $\langle E_i | S^* | E_j \rangle$ matrix element should also be nonzero.

As an example look at Fig. 5.6, notice the transitions that go from a localized state ($\langle S_Z \rangle = 5.86$) to a slightly delocalized state ($\langle S_Z \rangle = -4.45$). In this case we will assume, for the sake of argument, that the initial state has $m = 6$, which is a very likely scenario since 5.86 is close to 6. Then, the spin can transition to the $|m = 5\rangle$ state, for example, via a phonon transition. But notice that the $|E^*\rangle$ state, identified by $\langle S_Z \rangle = -4.45$, must be in a superposition of $|m\rangle$ states, one of which is $|m = 5\rangle$. In turn, $|m = 5\rangle$ must be in a superposition of $|E_i\rangle$ states, one of which must be the $|E^*\rangle$ state on the opposite side of the barrier. Notice that this is a transition that takes the spin to the opposite side of the barrier, even though it does not have enough energy to overcome the potential barrier. We will call this tunneling.

This kind of tunneling transition is caused by the mixing of states due to a perturbation induced by a transverse-field. This is a sort of instantaneous

tunneling: once the spin transitions to a $|E_i\rangle$ state that is in a superposition of $|m\rangle$ states, it has tunneled instantaneously between the $|m\rangle$ states. Imagine a four-state system with two ground states $|\pm 2\rangle$. Suppose that, near resonance, a transition takes the spin to an excited state that is in a superposition of $|m = 1\rangle$ and $|m = -1\rangle$ states. This will be similar to the two state problem described in chapter 2. Recall that the perturbation splits the degenerate levels into (Eq. (2.4))

$$|+\rangle = \frac{1}{\sqrt{2}}(|+1\rangle + |-1\rangle)$$
$$|-\rangle = \frac{1}{\sqrt{2}}(|+1\rangle - |-1\rangle) \, ,$$

which are eigenstates of the Hamiltonian, with their respective energies $E_+ = E + \Delta/2$ and $E_- = E - \Delta/2$. Suppose a phonon transition from $|+2\rangle$ to $|-\rangle$ occurs, followed by a transition from $|-\rangle$ to $|-2\rangle$. The missing step, which is not taken into account in the rate matrix, is the tunneling between $|+1\rangle$ and $|-1\rangle$. This is schematically represented in Fig. 5.8. We know that the probability of tunneling between the $|\pm 1\rangle$ states goes as $\sin^2(\frac{t\Delta}{2\hbar})$. If the splitting between the $|+\rangle$ and $|-\rangle$ states is very large, then the oscillations occur too fast in comparison to the phonon transitions. Therefore, not adding the *resonant* tunneling terms to the master equation (Eq. (5.22)) is a valid approximation off-resonance. This is not, however, a correct way of analyzing the on-resonance case (Fig. 5.8), in which the splitting is small and the oscillatory tunneling transitions may happen slowly in comparison to the phonon transitions. This is a defect of the Pauli formalism in Eq. (5.22). The master equations do not take into account the off-diagonal elements of the density matrix. One way to deal with this problem, is to add, by hand, correction terms to Eq. (5.22), like a tunneling term between quasi-degenerate states. This is much easier to be done in the $|m\rangle$ basis, as explained earlier in the beginning of this chapter. But, presumably, the off-diagonal elements would account for
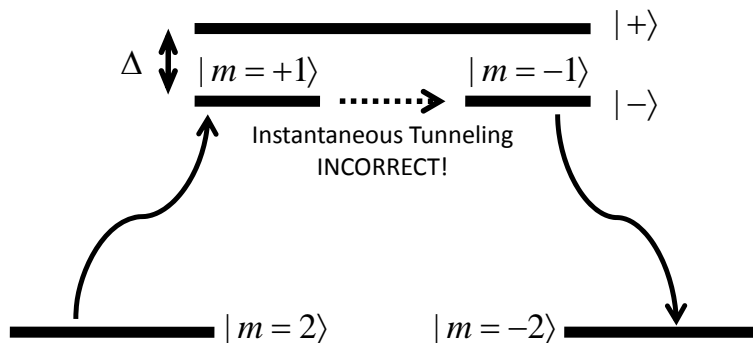
Figure 5.8: Thought experiment on a four-state system on-resonance. See text for explanation.

transitions where a phonon took a molecule to a superposition of $|E_i\rangle$ states. In our four-state system example, the off-diagonal elements would recognize transitions that took the molecule from $|m = 2\rangle$ to a superposition of $|+\rangle$ and $|-\rangle$. This would, presumably, take *resonant* tunneling into consideration.

Determining the most probable path is a more intense computational problem than drawing the diagrams. One way to do it would be to construct all the possible paths starting at one ground state and ending in the other. Then, one could, in principle, test all these paths and find the one of highest probability. The number of all possible paths increases exponentially with the number of nodes. It goes as 2^{n-2}, where n is the number of nodes. A simple proof by *strong* induction is provided in appendix C. One can see that for $n = 21$ there will be 2^{19} possible paths and computing all of them would be a very difficult computational problem. To decrease the number of paths to be checked, we

can first identify the lowest levels on the left and right wells for which a tunneling transition appears on the diagrams. Then we can focus on the levels that are above these two, identifying all such ones that have transitions shown in the diagram. Essentially, we identify all the levels that have arrows and are above the lowest levels involving tunneling transitions (see Fig. 5.9). These are usually no more than ten, and $2^8 = 256$ cases is within the computational power of most personal computers.
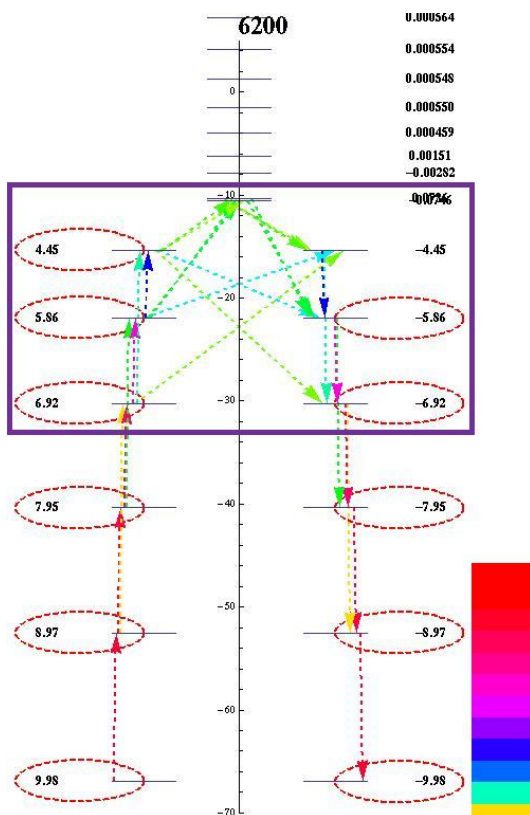
Figure 5.9: Inside purple box are the levels that have arrows and are above the highest levels not involving tunneling transitions.

But how does a molecule decide which path to take, and with what probability? At a given level, we normalize the probability currents. Suppose for example, that there are two outgoing currents from a given E_i level (see

Fig. 5.10). The probability that it will take path 1 is $p_1 = \bar{J}_1/(\bar{J}_1 + \bar{J}_2)$, and
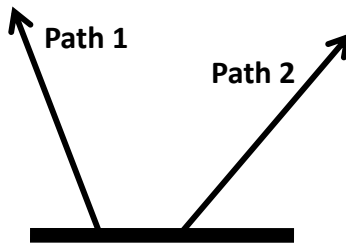
Figure 5.10: Two possible paths a molecule at E_i can take.

$p_2 = \bar{J}_2/(\bar{J}_1 + \bar{J}_2)$ that it will take path 2. We can generalize, and define the probability of choosing a given path to be

$$p_{i,j} = \bar{J}_{i,j} \left(\sum_{j, for \, \bar{J}_{i,j} > 0} \bar{J}_{i,j} \right)^{-1}. \tag{5.36}$$

The probability that a molecule will take the $(-10, a_1, a_2, \ldots, a_n, 10)$ path is

$$p_{(-10,a_1,a_2,\ldots,a_n,10)} = p_{-10,a_1} \left(\prod_{k=1}^{n-1} p_{a_k,a_{k+1}} \right) p_{a_n,10}. \tag{5.37}$$

In the diagrams (see Fig. 5.6) the levels involved in the most probable path are circled.

5.2.4 Transverse-field Dependence of the Most Probable Relaxation Path

This thesis is accompanied by a CD that can be found in the inside of the back cover. It contains video simulations of the path diagrams as the transverse-field is increased. To access the information on the CD, you will have to use

a computer. The video files in the CD are in the standard AVI format and should be easily accessed by most personal computers today. At this point I would ask the reader to have the videos ready to be played[11]. Because the diagrams contain a lot information you may want to go back and observe parts of the videos in slow motion or frame by frame. As I point out characteristics of a given diagram or of a given transition, particular frames will be displayed in this document.

On-resonance

Although we mentioned that the on-resonance transitions are not accurate, we can still gain information about the relaxation process. Notice, for example, the steps in Fig. 5.3. I ask the reader to play the "ON-RESONANCE" video. The first key observation is that as the transverse-field is increased, the inter-well transitions present in the most probable relaxation path moves to lower levels. We can identify the transitions with the steps we observe in Fig. 5.1.

For the sake of brevity and simplicity I will identify each diagram by its corresponding transverse-field and I will omit the units, which are Oersteds for all cases. And, I will identify the levels by their $\langle S_z \rangle$ expectation value. The first transition should happen around $H_T = 1400$. If we look at the 1100 diagram (Fig. 5.11) we will see a small current (yellow) from 2.94 to -3.98. The dominant path goes through a delocalized state, in the middle-top of the diagram. As H_T is increased to 1200, the $(2.94 \rightarrow -3.98)$ arrow becomes green, and at 1300 it becomes light blue (Fig. 5.12). Notice that at 1300 the dominant path now includes the 2.81 to -3.98 transition and the *delocalized*

---

[11]If you are accessing an electronic version of this thesis on the internet, the video files should also be available. I will refer to the videos by their file names.

Figure 5.11: Probability currents for $H_z = 5$ Oe and $T = 3K$. $H_T = 1100$ Oe as indicated on the top of the diagram. Observe a small current (yellow) from 2.94 to -3.98. See text for further explanation.

Figure 5.12: Probability currents for $H_z = 5\ Oe$ and $T = 3K$. $H_T = 1300\ Oe$ as indicated on the top of the diagram. The $(2.94 \rightarrow -3.98)$ arrow becomes the dominant "top" path. See text for further explanation.

top of the barrier is no longer part of the path. In the absence of H_T these levels should be 3 and -4 respectively, which means that the new path includes a tunneling transition. Effectively, the height of the barrier has been reduced, since the spin does not have to climb as high as it did before.

Let us analyze another step in Fig. 5.1. Let us focus on the step from 3000 to 4000. At 2800 the dominant path is a typical *delocalized top-of-the-barrier* path which characterizes the plateau from 2000 to 3000. At 2900, a new transition appears (light green), from 3.84 to -4.95 (Fig. 5.13). Considering the expectation values, this looks like a tunneling transition. At 3000, it becomes the dominant path (dark green). Then, from 3000 to 4000 the intensity of the dominant current increases very fast, from dark green to almost purple at 4000. Let's stop for a second and rephrase what happened. A new tunneling transition became relevant and quickly overpowered the previous inter-well transition. But this is exactly what the Lorentzians in Fig. 5.2 suggest. Then, from 4000 to 5000 the diagrams don't change much. The top transition level becomes more and more delocalized and the intensity of the top transition does not change much.

Now look at the 5100 diagram (Fig. 5.14). At this point the dominant path changed from $(\cdots 5.91 \rightarrow 4.83 \rightarrow 0.36 \rightarrow -4.83 \rightarrow -5.91 \cdots)$, which we call path A, to $(\cdots 5.91 \rightarrow -0.311 \rightarrow -5.91 \cdots)$, which we call path B. But if we look in Fig. 5.1 we don't see anything happening at $H_T = 5100$. But we should not. During the transition from path A to path B, the relaxation rates for both paths must be roughly the same. This is what a crossover between paths means: at 5000 path A was more probable than path B, but at 5100 path B became more probable, which implies that for some field value $5000 < H_x < 5100$ the rate for path A was the same as the rate for path B.

89
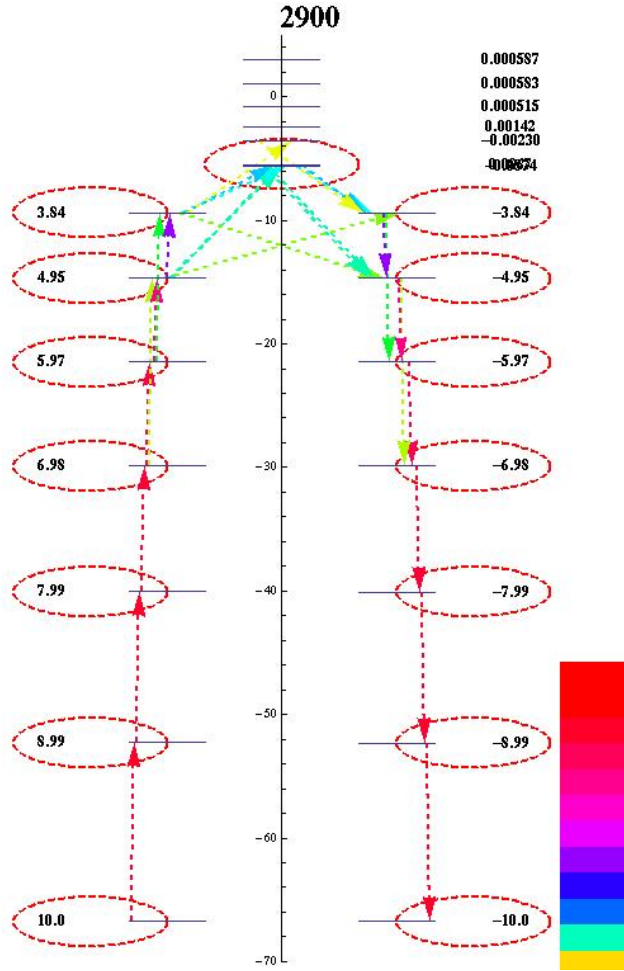
Figure 5.13: Probability currents for $H_z = 5$ Oe and $T = 3K$. $H_T = 2900$ Oe as indicated on the top of the diagram. A new transition appears (light green), from 3.84 to -4.95. See text for further explanation.
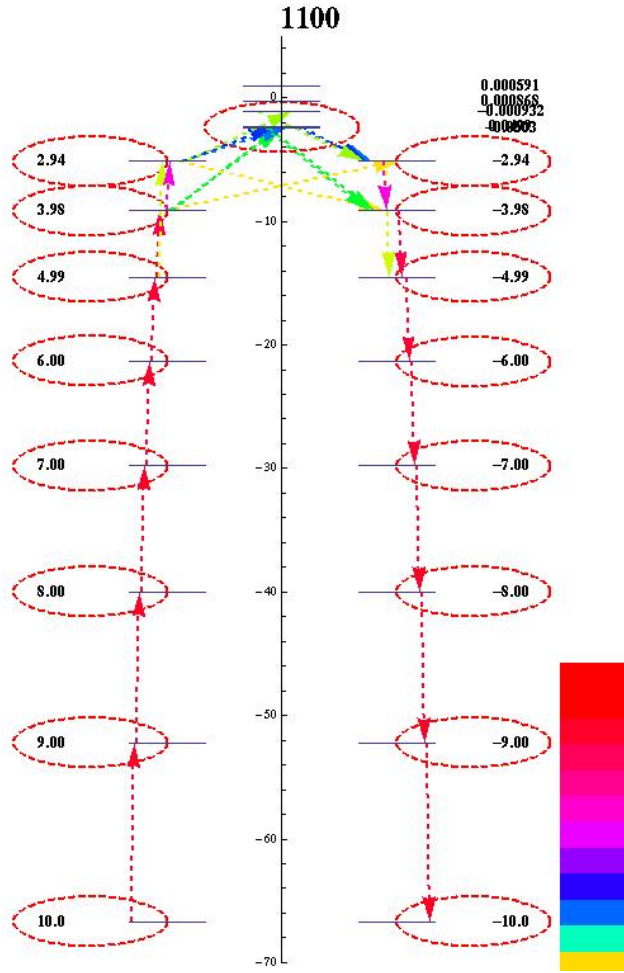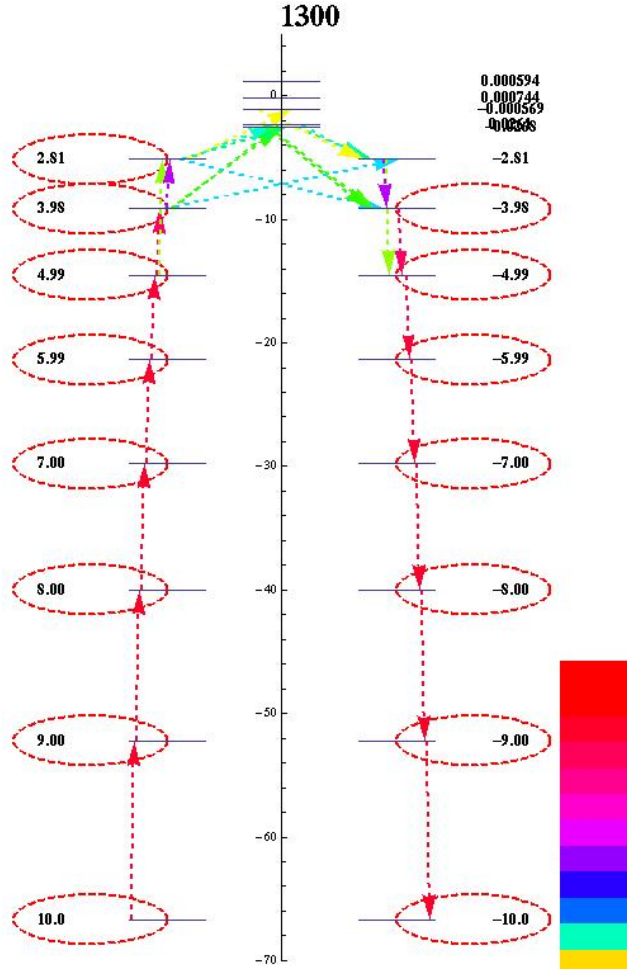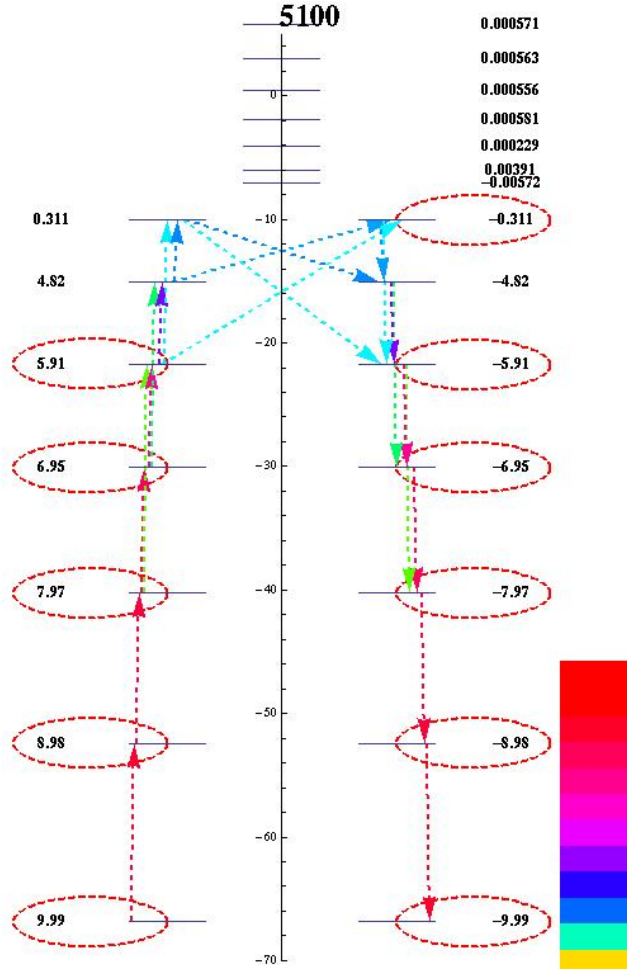
Figure 5.14: Probability currents for $H_z = 5\ Oe$ and $T = 3K$. $H_T = 5100\ Oe$ as indicated on the top of the diagram. $(\cdots 5.91 \to -0.311 \to -5.91 \cdots)$ is the new dominant transition. See text for further explanation.

Then, as H_x increases, the color of the top arrow $(5.91 \rightarrow -0.311)$ does not change much. We have to train our eyes to look, not for a transition between dominant paths, but for changes in the transverse-field dependence of path B compared to path A, which is exactly what we did when analyzing the 3000 transition.

Similar analysis can be done for other steps in Fig. 5.1 with the aid of the diagrams. By defining the barrier as the difference between the ground state and the energy of the highest level in the dominant path, we can calculate its transverse-field dependence (Fig. 5.15).
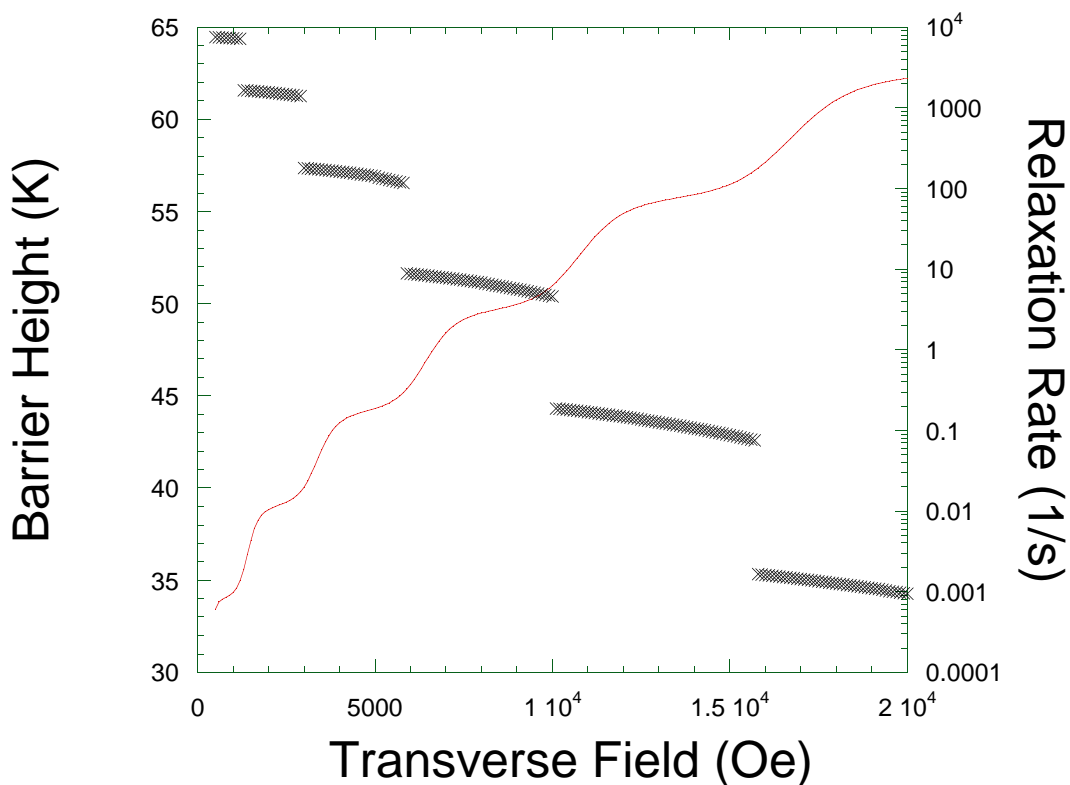
Figure 5.15: Transverse-field dependence of the barrier height for Mn$_{12}$-tBuAc on-resonance (black crosses) and transverse-field dependent relaxation rates on-resonance (red).

Another feature of the 5100 diagram (Fig. 5.14) that I would like to discuss is the double level transition between -0.311 and -5.91. Notice that there is another possible, but less probable, path: $(-0.311 \rightarrow -4.82 \rightarrow -5.91)$. From the expectation values, we know that -4.82 is mixed, but considering that $-4.82 \approx -5$ there is a very large chance that we would collapse this state to $|m = -5\rangle$ if we measured $\langle S_z \rangle$. Similarly, -5.91 is almost -6. Since only $\Delta m = 1$ transitions are allowed in the calculations, it would be intuitive to expect that the $(-4.82 \rightarrow -5.91)$ is so probable that the $(-0.311 \rightarrow -4.82 \rightarrow -5.91)$ would be the dominant path. In the diagram we see that the $(-0.311 \rightarrow -5.91)$ is light blue (weak), while the $(-0.311 \rightarrow -4.82)$ is blue (strong) and the $(-4.82 \rightarrow -5.91)$ is purple (very strong). The reason why this light blue transition dominates, goes back to the $(E_i - E_j)^3$ coefficients in the rate matrix elements (Eq. 5.24), which represents a strong dependence on the energy difference between any two levels, and the $1/(e^{\beta(E_i - E_j)} - 1)$ term in Eq. 5.24, which is the occupation number for Bose-Einstein statistics. The combination of both terms is the phonon energy density [30]:

$$\frac{\omega^3}{e^{\beta \omega} - 1},$$
(5.38)

where ω is the phonon energy.

To see how this affects the possible transitions I will sketch a brief example of the two-phonon Orbach process as illustrated in [30]. Let us analyze the three level system in Fig. 5.16.

State $|a\rangle$ and state $|b\rangle$ are very very close together, energetically, and $|c\rangle$ is at a much greater separation. In the two-phonon Orbach process, the indirect relaxation of the population in $|b\rangle$ to the population in $|a\rangle$, via $|c\rangle$, gives a much faster relaxation path than the direct $|b\rangle \rightarrow |a\rangle$ transition. The reason
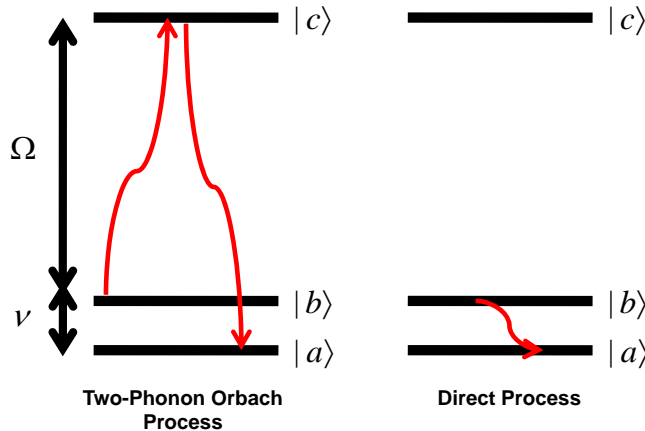
Figure 5.16: Possible relaxation processes from $|b\rangle$ to $|a\rangle$. Two-phonon Orbach process (left) and direct process (right).

is the higher phonon density at transition energies close to Ω than close to ν. Figure 5.17 shows the phonon energy density for $3\ K$. Notice from Fig. 5.17 that the number of phonons is largest for energies around $10\ K$. But that is roughly the energy separation between -0.311 and -4.82. This explains why $p_{-0.311,-5.91}$ beats the product of $p_{-0.311,-4.82}$ and $p_{-4.82,-5.91}$, even though $p_{-0.311,-5.91} < p_{-0.311,-4.82}$ and $p_{-0.311,-5.91} < p_{-4.82,-5.91}$.

The phonon energy distribution is also the reason why we do not see any cross-well phonon-induced transitions between quasi-degenerate levels. Instead, the molecule has to be excited to a higher level and then relax to the a level on the opposite well, in an analogous way to the two-phonon Orbach process. This is where a proper treatment of *resonant* tunneling could change the dominant relaxation paths. Having a full density matrix formalism, where the off-diagonal elements are included in the calculations, could lead to oscillations between nearly degenerate energy levels. And the decay of these oscillations

94
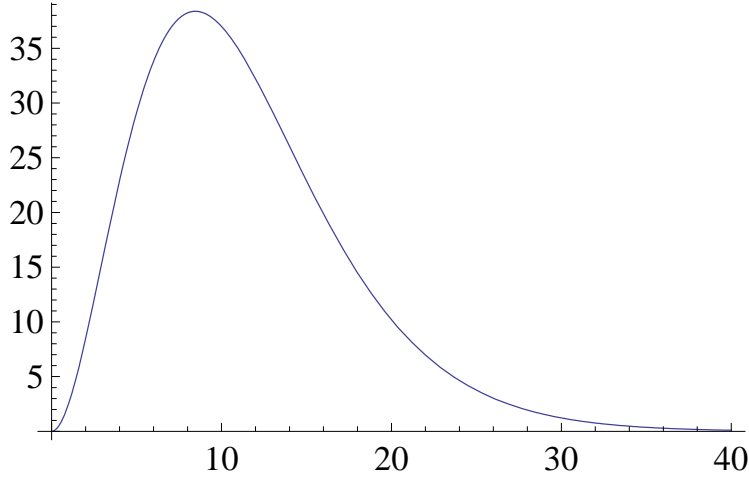
Figure 5.17: Phonon energy distribution (arbitrary units) at 3 K as a function of energy (in K).

would, presumably, lead to a population transfer between wells. This kind of tunneling could be, maybe, slow enough that it would decrease the relaxation rates. It is hard to say what effects this could have in our results. It could, for example, decrease the transverse-field dependence of some transitions and consequently smooth out the on-resonance steps in Fig. 5.1.

Having observed the main features of the relaxation on-resonance, and keeping in mind that these diagrams do not take into account *resonant* tunneling, I will now discuss the dynamics off-resonance.

Off-resonance

For the off-resonance discussion, there are two videos. *OFF-RESONANCE 1000* ($H_z = 1000\ Oe$) is the one we will discuss in this section, but I also included *OFF-RESONANCE 500* ($H_z = 500\ Oe$) for the interested reader. They both show similar behavior. So, I ask the reader to have the *OFF-*

95

RESONANCE 1000 file ready for visualization.

The transverse-field dependent relaxation rate for $H_z = 1000\ Oe$ (Fig. 5.1) is reproduced in Fig. 5.18 for a narrower range of H_T. Because, off-resonance,
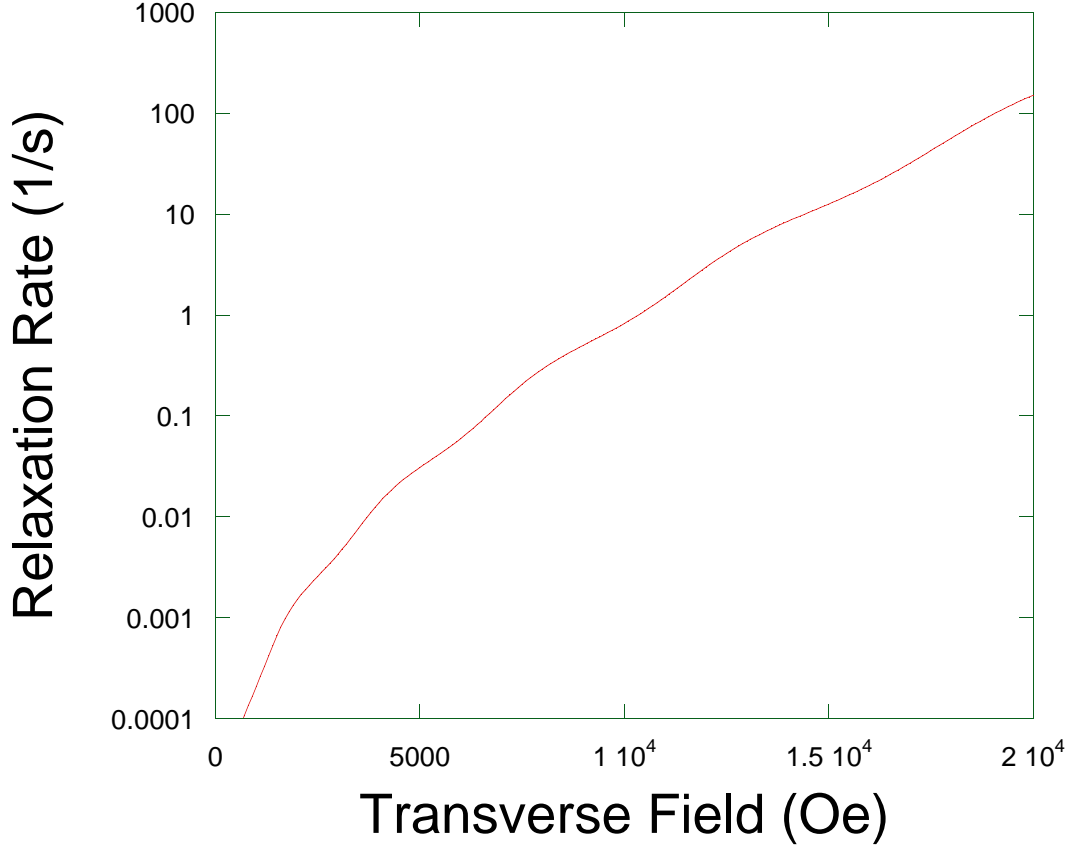
Figure 5.18: Transverse-field dependent relaxation rate for $H_z = 1000\ Oe$.

the sharpness of the steps is much decreased, it becomes harder to define where they begin and where they end. We produce a similar kind of analysis as the one we did for the on-resonance diagrams.

In the 3600 diagram we observe the transition $(3.80 \rightarrow -0.197 \rightarrow -3.84)$, which defines the top of the barrier. Then at 3700 we observe a crossover to a new dominant path $(4.91 \rightarrow 1.95 \rightarrow -3.83)$. This last path does not last long,

and at 3800 (Fig. 5.19) the dominant transition becomes $(4.90 \rightarrow 1.85 \rightarrow -4.91)$. Notice that the $(1.85 \rightarrow -4.91)$ transition looks like a tunneling
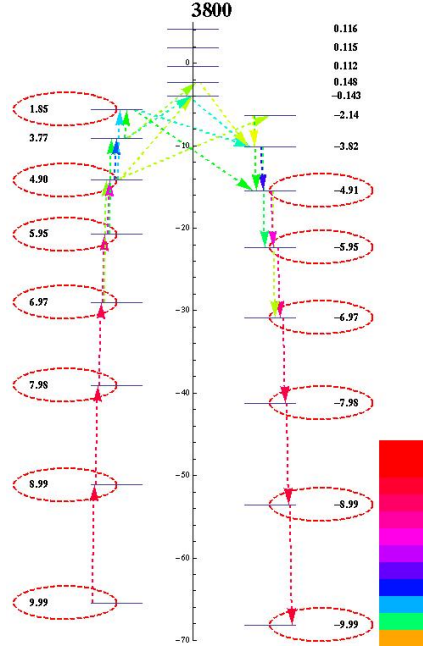
Figure 5.19: Probability currents for $H_z = 1000\ Oe$ and $T = 3K$. $H_T = 3800$ Oe as indicated on the top of the diagram. The dominant transition becomes $(4.90 \rightarrow 1.85 \rightarrow -4.91)$. See text for further explanation.

transition: -4.91 is close to -5 and 1.85 is not entirely delocalized. Furthermore, the intensity of this transition increases quickly as H_x is increased. This characterizes a step in Fig 5.18. The transverse-field dependence of the $(1.85 \rightarrow -4.91)$ transition is not as high as the ones that defined a step in the on-resonance cases. And, this last fact is completely consistent with the on-resonance steps being sharper than the off-resonance steps in Fig. 5.1.

At 4700 we observe a slight drop in barrier height. The highest state in the most probable path changes from being 1.03 at 4600 to -1.31 at 4700. Notice, however, that there is not much change in the intensity of the highest transition. And we, therefore, do not observe a step in Fig. 5.18. At 4600
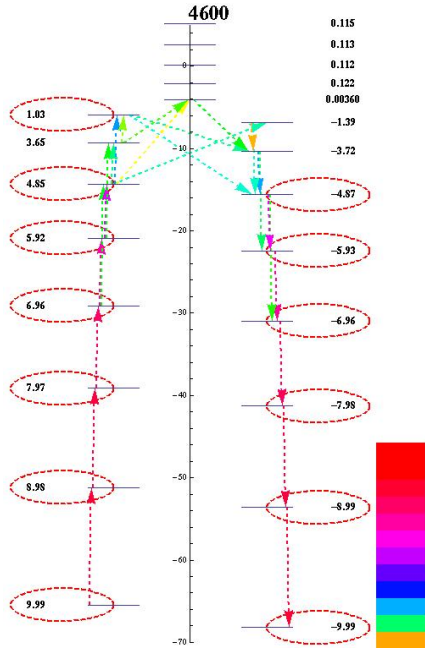
Figure 5.20: Probability currents for $H_z = 1000\ Oe$ and $T = 3K$. $H_T = 4600\ Oe$ as indicated on the top of the diagram. The $(1.03 \rightarrow -4.87)$ transition is light blue. See text for further explanation.
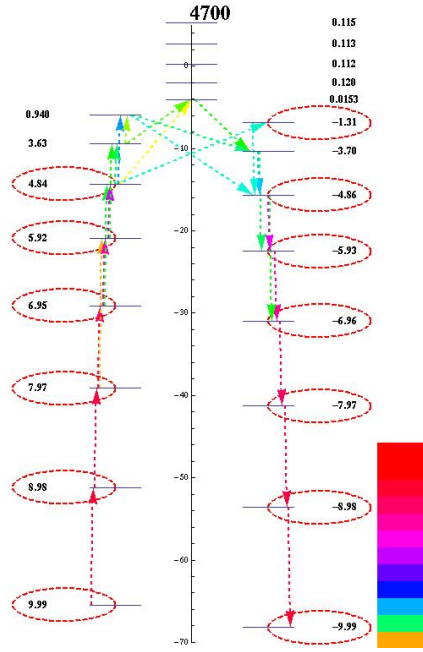
Figure 5.21: Probability currents for $H_z = 1000\ Oe$ and $T = 3K$. $H_T = 4700\ Oe$ as indicated on the top of the diagram. The $(4.84 \rightarrow -1.31)$ transition is light blue. See text for further explanation.

98

(Fig. 5.20), $(1.03 \rightarrow -4.87)$ was light blue, and, at 4700 (Fig. 5.21), $(4.84 \rightarrow -1.31)$ is also light blue, remaining this way until 6500. At 6600 the dominant path becomes $(5.84 \rightarrow 2.87 \rightarrow -5.85)$. This is quite a change from the previous dominant path, which was $(4.69 \rightarrow -0.441 \rightarrow -4.73)$ at 6500. And this crossover corresponds to a step in Fig. 5.18. The new "top" transition becomes $(2.87 \rightarrow -5.85)$. As we increase the transverse field, the color of the transition increases quickly from light green at 6600 to light blue at 7500. If we count, starting at the bottom, the states on the left well, one would expect that in the absence of a transverse-field the 2.87 state would have $\langle S_z \rangle = +4$. Although, this state is not really localized, it is not quite delocalized either. We conclude that the steps in Fig. 5.18 are associated with the appearance of a tunneling transition (notice that -5.85 is pretty close to 6.) that quickly overpowers the previous dominant path, and shows a strong transverse-field dependence from then on.

We can, as was done for the on-resonance case, determine the height of the barrier as the highest energy level in the most probable path (Fig. 5.22). Although the off-resonance case shows more abrupt changes in the barrier height than the on-resonance case, the number of steps in the relaxation rate does not increase. Both cases, however, show the same behavior: a crossover between dominant paths, where a "tunneling" transition (strongly dependent on H_x) appears in the new path. Whether or not this transition should be called tunneling is up for discussion. But we do reemphasize that we call it tunneling becuase it is a transition that takes a molecule, without enough energy to overcome the anisotropy barrier, to the opposite well.
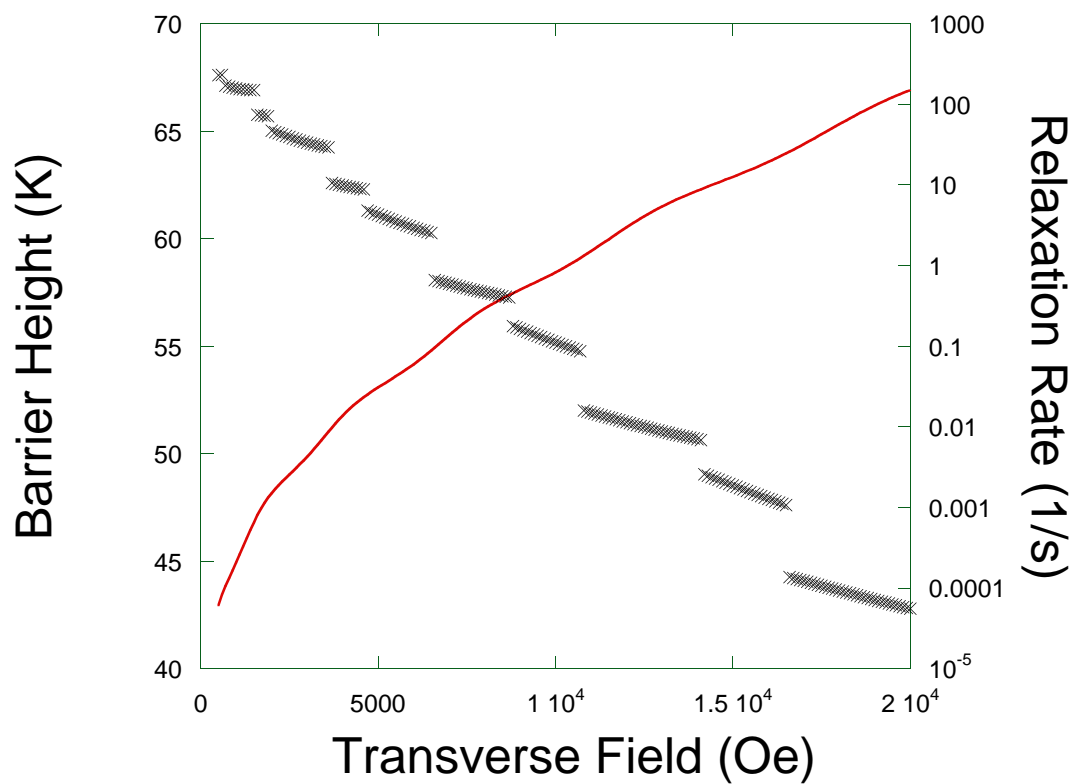
Figure 5.22: Transverse-field dependence of the barrier height for Mn$_{12}$-tBuAc off-resonance (black crosses) and transverse-field dependent relaxation rates off resonance (red).

5.3   Summary of Theoretical Results

We conclude this section by reaffirming that the current theory reproduces the appearance of steps in the transverse-field relaxation rates, both on-resonance and off-resonance. The interpretation that the steps in the relaxation rates is directly related to barrier reduction seems to be correct. Although, one should be careful in formulating this correlation. We observe a reduction in the effective barrier height, due to a crossover between dominant relaxation paths. It should not be thought, however, that a decrease in barrier height, caused by a transverse-field, automatically implies a step in the relaxation rate. It is the transverse-field dependence of the new dominant path that will determine whether a step appears in the relaxation rate versus transverse-field data.

The diagrams produced in the videos contain a lot of information about the relaxation processes, and we feel that they have much more to teach us than we have presented in this chapter. It seems that when tunneling transitions become part of the dominant relaxation path, the relaxation rates quickly increase with the transverse-field.

One task in which we were not successful, was to understand why the experiments show sharper steps off-resonance than on-resonance. Also, in the Pauli formalism, *resonant* tunneling is not properly treated. It is possible that the effects of the non-diagonal terms of the density matrix could have strong results in the on-resonance relaxation processes.

Chapter 6

Conclusions and Directions for Future Research

First, it is important to give Mn_{12}-tBuAc its due credit. Its true axial symmetry seems to have contributed a major role in producing some of our experimental results. Perhaps its symmetry is not perfect and some crystalline disorder may be responsible for inhomogeneous broadening. This could be a possible answer to why we do not observe sharp superimposed peaks in the longitudinal-field distributions of the relaxation rate. On the other hand, it is also possible that the reason why we observe the widths to oscillate, is the higher symmetry Mn_{12}-tBuAc has over the Mn_{12}-Ac SMM.

We also believe that the real-time relaxation technique has proved itself to be very successful. Looking at the time-evolution of the magnetization is a direct way of measuring it, and, quite possibly, a lot of information about the dynamics of the system is lost when doing ACS measurements, which measures how fast the magnetization can follow an oscillating field.

Experimentally, our strongest results are the series of plateaus and steps of

the transverse-field dependent magnetic relaxation rates, and the transverse-field induced oscillations of the widths of the longitudinal-field distribution of the the relaxation rates. These two effects seem to be well described by the current theory, which is based on the the Pauli rate equation (Eq. (5.22)). In this formalism, the off-diagonal elements of the density matrix are not taken into account, which leaves our rate calculations for the on-resonance case incomplete.

We also find that the path diagrams contain a lot of information that still needs to be extracted. Due to the lack of time, we have not yet been able to study the temperature dependence of the diagrams. Furthermore, it would be interesting to fit the theoretical curves to the experimental data, which is something we plan to do very soon.

There are still many measurements to be taken. The good news is that a lot of the measurements can be performed very soon and most of the data acquisition, and data analysis, has been automated. In particular, the $N = 1$ resonance experiments could potentially yield a lot of useful information. In Fig. 6.1 we show the theoretical calculations for the longitudinal-field dependence of the relaxation rates near the $N = 1$ resonance. Due to the fourth-order anisotropy, the appearance of the new peaks, presumably due to a new tunneling resonance, occurs off-center to the previous resonance. This may facilitate the detection of these peaks. And, the position of the peaks would give us enough information to determine what the pair of tunneling levels is. This would lead to a direct measure of the barrier height. The other way we could measure the barrier height would be by taking ACS measurements of the relaxation rates for different temperatures, and then using the Arrhenius law to extract the barrier height.
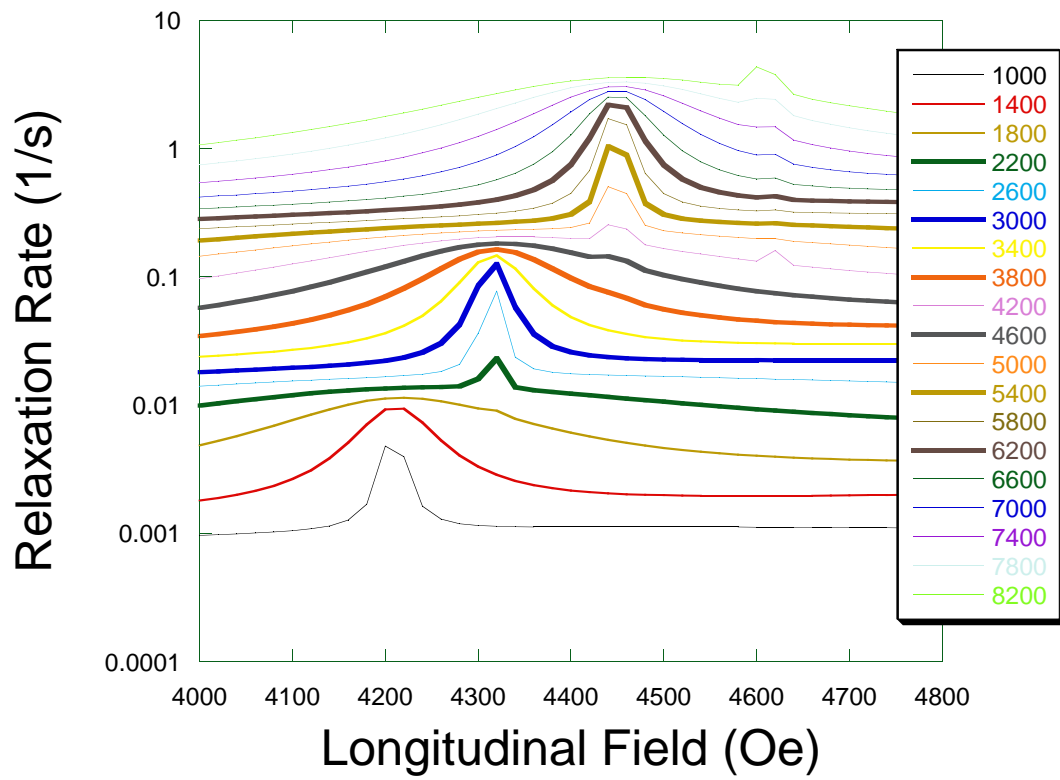
Figure 6.1: Longitudinal field dependence of the relaxation rate of magnetization for different transverse-fields (in Oe) and at $3\ K$.

One puzzle is left unsolved. Why are the transverse-field dependent steps of the relaxation rate sharper off-resonance than on-resonance? This last observation is in direct contradiction with our simulations. We believe that the answer to this puzzle could lead to a better understanding of the physics behind the thermally-assisted relaxation processes in SMMs.

Appendix A

Spatial Tunneling and Barrier Penetration

Let us assume the potential in equation (A.1), which represents an energy barrier between $x = 0$ and $x = a$.

$$V(x) = \begin{cases} V_0, & \text{for } 0 \leq x \leq a; \\ 0, & \text{for } x < 0 \text{ and } a < x; \end{cases} \quad \text{(A.1)}$$

Imagine, then, a beam of particles incident from the left $(x < 0)$, all of them with energy $E < V_0$. Classically these particles will all be reflected and none will traverse to the right side of the barrier $(x > a)$. The general solutions to the SE are,

$$\psi_1(x) = Ae^{ik_1 x} + Be^{-ik_1 x}, \qquad x < 0$$

$$\psi_2(x) = Ce^{-\alpha x} + De^{\alpha x}, \qquad 0 < x < a \qquad \text{(A.2)}$$

$$\psi_3(x) = Fe^{ik_1 x} + Ge^{-ik_1 x}, \qquad x > a$$

where $k_1 = \sqrt{2mE}/\hbar$ and $\alpha = \sqrt{2m(V_0 - E)}/\hbar$. The first and third solutions, ψ_1 and ψ_2 in (A.2) are oscillatory under all conditions since $k_1^2 \geq 0$, always. The second solution, ψ_2, can be either oscillatory or a real exponential function. In our case of interest, $E < V_0$ $(\alpha > 0)$, ψ_2 involves real exponentials

only. Since we restricted the beam to come from the left, we can set G=0. Furthermore the remaining five (A, B, C, D, F) unknown constants can be reduced to only one (A) by applying the continuity conditions on ψ and $d\psi/dx$. And A will be determined by the initial conditions, particle density in this case. I will leave the intermediate steps to the reader. The important result is that the wave function decays exponentially in the classically forbidden region and at $x = a$, $\psi \neq 0$. The continuity of ψ ensures that the amplitude of the oscillatory solution, ψ_3, for $x > a$ will not have zero amplitude. This means that there is a nonzero probability that the particle can be found on the right side of the barrier. This phenomenon is known as *tunneling* or *barrier penetration.*

Appendix B

Analysis of Relaxation Decay using a Convolution of Exponentials

We assume that each molecule in a Mn_{12}-tBuAc crystal decays exponentially, but that the decay rate for each molecule is different:

$$M_i = M_0 e^{-\Gamma_i t} \tag{B.1}$$

We also assume that the probability that a given molecule will decay with Γ is given by a Gaussian distribution

$$\frac{1}{\sigma\sqrt{2\pi}} e^{-\frac{(\Gamma-\tilde{\Gamma})^2}{2\sigma^2}}, \tag{B.2}$$

centered about $\tilde{\Gamma}$, and where σ is the standard deviation. The total magnetization becomes

$$M = \frac{M_0}{\sigma\sqrt{2\pi}} \int_0^{+\infty} e^{-\Gamma t} e^{-\frac{(\Gamma-\tilde{\Gamma})^2}{2\sigma^2}} d\Gamma. \tag{B.3}$$

As long as σ is small compared to Γ, we can change the lower limit of the integral to $-\infty$. Gaussian integrals are easier to evaluate over the entire real line. This is a good approximation since we would expect that the number of

molecules relaxing with Γ too close to zero should be negligible, and we should expect the number of molecules with exponentially *increasing* magnetization to be zero. The data is fit to

$$M = \frac{M_0}{\sigma\sqrt{2\pi}} \int_{-\infty}^{+\infty} e^{-\Gamma t} e^{-\frac{(\Gamma-\tilde{\Gamma})^2}{2\sigma^2}} d\Gamma + c, \tag{B.4}$$

where there are four fitting parameters: M_0, σ, c and $\tilde{\Gamma}$. This is not an easy function to fit but after some adjustments, Mathematica was able to do it[1]. A fitting code for this function can be found in appendix D. The function in (B.4) generates a better fit, but the residuals are also skewed (Fig. B.1). The fourth fitting parameter is the probable reason for the improvement in the fit. We were not successful in this kind of fit because small adjustments in the σ parameter, compensated for the fitted value of $\tilde{\Gamma}$ (see exponent in Eq. (B.4)). After many frustrated attempts to reproduce consistent fitting parameters, for different initial guesses of σ, we decided to abandon this model.
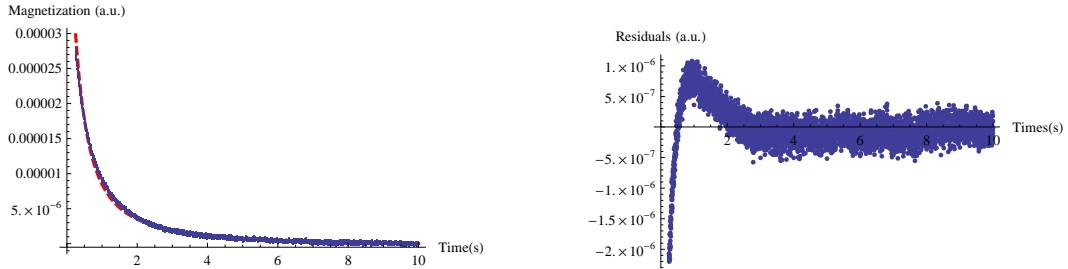
Figure B.1: Fit for convolution of exponentials function (dashed line) for the relaxation of magnetization on-resonance (left) and residuals(right) – 3 K, 6000 Oe transverse-field.

---

[1]Thanks to Andy Anderson for helping with the code.

Appendix C

Number of All Possible Paths: Proof by *Strong* Induction

Let n be the number of nodes and N be the number of all the possible paths. If $n = 2$, there is only one possible path. This will be our base case. The inductive hypothesis is that for all $n \leq k$, $N = 2^{n-2}$. If we add another node, the number of paths becomes

$$2^{k-2} + 2^{k-3} + 2^{k-4} + \cdots 2^{k-(k-1)} + 1 + 1.$$

The first term appears as a result of adding an extra node to all paths that previously existed (k^{th} case). The second term appears as a result of adding a node to all paths existent in the $k - 1$ case. The penultimate term $(+1)$ is due to adding a node to the base case and the last term $(+1)$ is the case of a transition going through all nodes. After some manipulation the sum becomes

$$2^{k-2}\left(1 + \frac{1}{2} + \cdots + \frac{1}{2^{k-2}}\right) + 1$$

$$= 1 + 2^{k-2}\frac{\left(1 - \left(\frac{1}{2}\right)^{k-2+1}\right)}{1 - \frac{1}{2}}$$

$$= 2^{k-1}, \quad \text{(C.1)}$$

which completes the proof[1].

---

[1]Thanks to Ben Dickman for pointing out the simplicity of the proof and making me do it.

Appendix D

Mathematica Code for Exponential Fit and Convolution of Exponentials Fit

```
Needs["NonlinearRegression`"]
```

Parameters

```
initialAngle = 177.5;
finalAngle = 186.5;
angleStep = .15;
field = 6000;
plotTime = 10;
InitialParTime = 1;
TotalTime = 10;

skip = .25;

CentralAngle = 182;
filePrefix =

  "C :\ Our Documents\ Eduardo\ Relaxation Experiments\ Mn12-tBuAc\ Sample1 6-07-2007\ DC

    Relaxation\3.0K \ After Sample moved\ Lock -in acquisition\ System

    test\ DATA\ Mn12tBuAc 20mV  37Hz  1ms T=3.00 H =6000 theta= ";

outputFolder = "C :\ Our Documents\ Eduardo\ test";
```

Calibration

$$\text{Simplify}\left[\text{Normal}\left[\text{Series}\left[\left(1 + \text{Erf}\left[\frac{\left(-\frac{s^2}{y} + \Gamma\right)\big/ s}{\sqrt{2}}\right]\right), \{y, 0, 5\}, \text{Assumptions} \to \{y > 0, -2 s^2 y \Gamma + y^2 \Gamma^2 < 0, s > 0\}\right]\right]\right]$$

$$\frac{e^{-\frac{\left(\frac{s^2}{y} + \Gamma\right)^2}{2 s^2}} \sqrt{\frac{2}{\pi}} \, y \left(s^8 + y^4 \Gamma^4 + s^2 y^3 \Gamma^2 \, (-6 y + \Gamma) + s^6 y \, (-y + \Gamma) + s^4 y^2 \left(3 y^2 - 3 y \Gamma + \Gamma^2\right)\right)}{s^9}$$

$$\text{SuperFunction}[y\_, \Gamma\_, s\_] := \text{Piecewise}\left[\left\{\left\{\frac{e^{-\frac{\left(-\frac{s^2}{y} + \Gamma\right)^2}{2 s^2}} \sqrt{\frac{2}{\pi}} \, y \left(s^8 + y^4 \Gamma^4 + s^2 y^3 \Gamma^2 \left(-6 y + \Gamma\right) + s^6 y \, (-y + \Gamma) + s^4 y^2 \left(3 y^2 - 3 y \Gamma + \Gamma^2\right)\right)}{s^9}\right.\right.\right.,$$

$$\left.1 + \text{Erf}\left[\frac{\left(-\frac{s^2}{y} + \Gamma\right)\big/ s}{\sqrt{2}}\right] < 2 * 10^{-14}\right\},$$

$$\left\{1 + \text{Erf}\left[\frac{\left(-\frac{s^2}{y} + \Gamma\right)\big/ s}{\sqrt{2}}\right], 1 + \text{Erf}\left[\frac{\left(-\frac{s^2}{y} + \Gamma\right)\big/ s}{\sqrt{2}}\right] \geq 2 * 10^{-14}\right\}\right\}\right]$$

$$\text{Plot}\left[\left\{1 + \text{Erf}\left[\frac{\left(-\frac{s^2}{y} + \Gamma\right)\Big/s}{\sqrt{2}}\right]\right\} \text{ /. } \{\Gamma \to 1.14, \, s \to .251\}\right\}, \, \{y, \, .019, \, .020\}, \, \text{PlotRange} \to \text{All}\right]$$
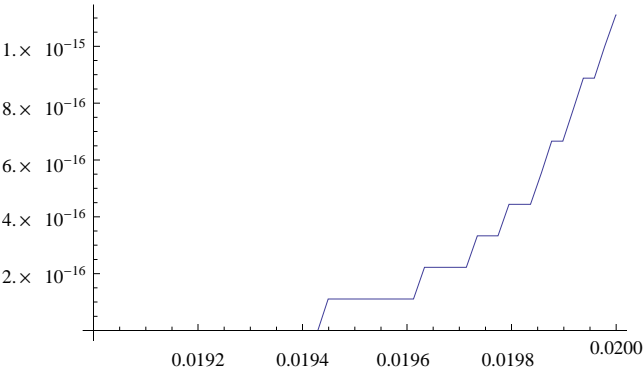
```
Plot[{SuperFunction[y, 1.14, .251]}, {y, .019, .0207}, PlotRange → All]
```

$$\texttt{Plot}\left[\left\{1 + \texttt{Erf}\left[\frac{\left(-\frac{s^2}{y} + \Gamma\right)\Big/s}{\sqrt{2}}\right] \Big/. \{\Gamma \to 1.14, s \to .251\}, \texttt{SuperFunction}[y, 1.14, .251]\right\},\right.$$

$$\left.\{y, .019, .02\}, \texttt{PlotRange} \to \texttt{All}\right]$$
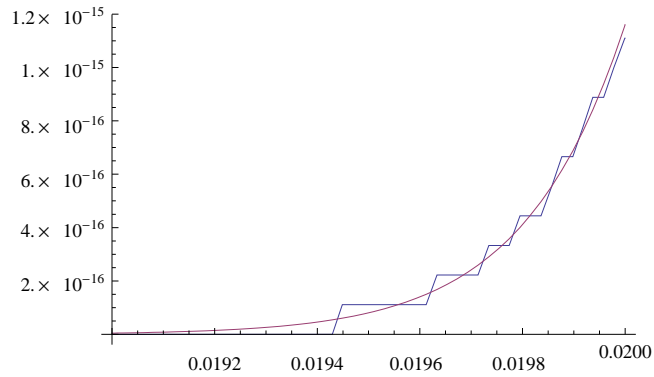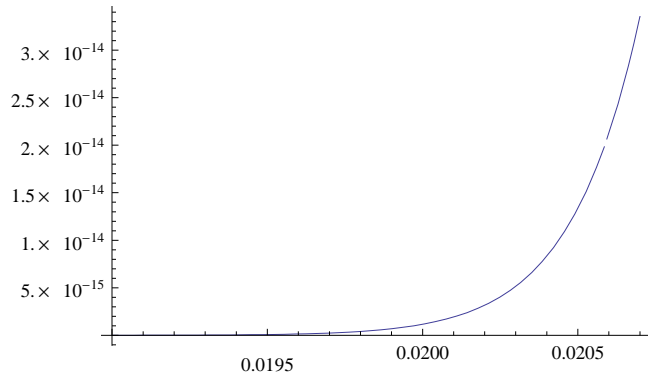
Set

$$\texttt{length} = \frac{\left(\texttt{finalAngle} - \texttt{initialAngle}\right)}{\texttt{angleStep}} + 1;$$

```
DataPoints = Table[0, {length + 1}, {9}];
```

$$\texttt{DataPoints}[[1]] = \left\{\texttt{" Angle" , " a" , " error" ,}\right.$$

$$\left.\texttt{" Relaxation Rate (1/s)" , " error" , " c" , " error" , " sigma" , " error"}\right\};$$

Run

$$\texttt{For}\left[\texttt{i = 0, i < length, i++,}\right.$$

```
 angle = initialAngle + i * angleStep;
 angleString = ToString[SetAccuracy[angle, 3]];
```

$$\texttt{Data = Import}\left[\texttt{filePrefix <> angleString <> " .txt" , " Table"}\right];$$

```
 Data = Drop[Data, 1];
```

$$\texttt{ExpFit = FindFit}\left[\right.$$

```
Table[{Data[[n]][[1]], Data[[n]][[2]]}, {n, 1, 512 * (InitialParTime + skip)}], {a Exp[-Γ*x] /
                                                                                       √(2*π)  *

  Exp[s²x²/2] * √(π/2) * Normal[Series[ (1 + Erf[ (√(1/s²) (-s² x + Γ)) / √2 ]), {x, Γ/s, 5}]] },

  {{a, Data[[1]][[2]]}, Γ, c, s}, x, MaxIterations → 1000];
ExpFit2 = FindFit[Table[{Data[[n]][[1]], Data[[n]][[2]]}, {n, 1, 512 * TotalTime}],

  {a Exp[-Γ*x]/1 + c}, {{a, Data[[1]][[2]]}, {Γ, .01}, c}, x, MaxIterations → 1000];
Print[" Exponential at " <> angleString];
Print[Show[Plot[a Exp[-Γ*x]/1 + c /. ExpFit2,

  {x, skip, TotalTime}, PlotRange → All, PlotStyle → {Red, Dashed, Thick }],

  ListPlot[Table[{Data[[n]][[1]], Data[[n]][[2]]}, {n, 512 * skip, 512 * TotalTime}],

  PlotRange → All, PlotStyle → PointSize[0.003]], AxesOrigin → {0, -5 * 10^-7}]];
residualsExp = Apply[Function[{x, y}, Evaluate[{x, y - (a Exp[-Γ*x]/1 + c) /. ExpFit2}]],

  Table[{Data[[n]][[1]], Data[[n]][[2]]}, {n, 512 * skip, 512 * TotalTime}], 1];
Export[" C :\ Data\ Exp" <> angleString <> " .pdf" , Show[Plot[a Exp[-Γ*x]/1 + c /. ExpFit2,

  {x, skip, TotalTime}, PlotRange → All, PlotStyle → {Red, Dashed, Thick }],

  ListPlot[Table[{Data[[n]][[1]], Data[[n]][[2]]}, {n, 512 * skip, 512 * TotalTime}],

  PlotRange → All, PlotStyle → PointSize[0.003]],

  AxesOrigin → {0, -5 * 10^-7}, AxesLabel → {" Time(s)" , " Magnetization (a.u.)" }]];
Print[ListPlot[residualsExp]];

Export[" C :\ Data\ ExpRes" <> angleString <> " .pdf" ,

  ListPlot[residualsExp, AxesOrigin → {0, 0}, AxesLabel → {" Time(s)" , " Residuals (a.u.)" }]];
aInit = a /. ExpFit;
ΓInit = Γ /. ExpFit;
sInit = ΓInit / 5;
FIT =
  NonlinearRegress[Table[{Data[[n]][[1]], Data[[n]][[2]]}, {n, 512 * skip, 512 * TotalTime}],

  a Exp[-Γ*x]/√(2*π) * Exp[s²x²/2] * (√(π/2) (SuperFunction[1/x, Γ, s ]))/1 + c,

  {{a, aInit}, {Γ, ΓInit}, {c, 1}, {s, sInit}}, x, Gradient → " FiniteDifference" ,
```

```mathematica
     MaxIterations → 10 000, RegressionReport → ParameterTable, PrecisionGoal → ∞];

DataPoints[[i + 2]] = {angle, FIT[[1]][[2]][[1]][[1]][[1]],
  FIT[[1]][[2]][[1]][[1]][[2]], FIT[[1]][[2]][[1]][[2]][[1]],
  FIT[[1]][[2]][[1]][[2]][[2]], FIT[[1]][[2]][[1]][[3]][[1]], FIT[[1]][[2]][[1]][[3]][[2]],
  FIT[[1]][[2]][[1]][[4]][[1]], FIT[[1]][[2]][[1]][[4]][[2]]};
Print[angleString];
Print[aInit];
Print[FIT[[1]][[2]][[1]][[1]][[1]] + FIT[[1]][[2]][[1]][[3]][[1]]];
```

$$\text{Print}\left[\text{Show}\left[\text{Plot}\left[\left(a\,\frac{\text{Exp}[-\Gamma * x]}{\sqrt{2 * \pi}} * \text{Exp}\left[\frac{s^2 x^2}{2}\right] * \frac{\sqrt{\frac{\pi}{2}}\,\left(\text{SuperFunction}[1/x,\ \Gamma,\ s\ ]\right)}{1} + c\right) /.\right.\right.\right.$$

```mathematica
   {a → FIT[[1]][[2]][[1]][[1]][[1]], Γ → FIT[[1]][[2]][[1]][[2]][[1]],
    c → FIT[[1]][[2]][[1]][[3]][[1]], s → FIT[[1]][[2]][[1]][[4]][[1]]},
  {x, skip, plotTime}, PlotStyle → {Red, Dashed, Thick }, PlotRange → All],
  ListPlot[Table[{Data[[n]][[1]], Data[[n]][[2]]}, {n, 512 * skip, 512 * 10}],
  PlotStyle → PointSize[0.001]], PlotRange → All, AxesOrigin → {0, -5 * 10^-7}]];

Export[" C :\ Data\ Conv " <> angleString <> " .pdf" ,
```

$$\text{Show}\left[\text{Plot}\left[\left(a\,\frac{\text{Exp}[-\Gamma * x]}{\sqrt{2 * \pi}} * \text{Exp}\left[\frac{s^2 x^2}{2}\right] * \frac{\sqrt{\frac{\pi}{2}}\,\left(\text{SuperFunction}[1/x,\ \Gamma,\ s\ ]\right)}{1} + c\right) /.\right.\right.$$

```mathematica
   {a → FIT[[1]][[2]][[1]][[1]][[1]], Γ → FIT[[1]][[2]][[1]][[2]][[1]],
    c → FIT[[1]][[2]][[1]][[3]][[1]], s → FIT[[1]][[2]][[1]][[4]][[1]]},
  {x, skip, plotTime}, PlotStyle → {Red, Dashed, Thick }, PlotRange → All],
  ListPlot[Table[{Data[[n]][[1]], Data[[n]][[2]]}, {n, 512 * skip, 512 * 10}],
  PlotStyle → PointSize[0.001]], PlotRange → All,
  AxesOrigin → {0, -5 * 10^-7}, AxesLabel → {" Time(s)" , " Magnetization (a.u.)" }]];

residuals = Apply[Function[{x, y}, Evaluate[
```

$$\left\{x,\ y - \left(a\,\frac{\text{Exp}[-\Gamma * x]}{\sqrt{2 * \pi}} * \text{Exp}\left[\frac{s^2 x^2}{2}\right] * \frac{1}{1}\sqrt{\frac{\pi}{2}}\,(\text{SuperFunction}[1/x,\ \Gamma,\ s])\ + c\right) /.\right.$$

```mathematica
     {a → FIT[[1]][[2]][[1]][[1]][[1]], Γ → FIT[[1]][[2]][[1]][[2]][[1]],
      c → FIT[[1]][[2]][[1]][[3]][[1]], s → FIT[[1]][[2]][[1]][[4]][[1]]}}],
  Table[{Data[[n]][[1]], Data[[n]][[2]]}, {n, 512 * skip, 512 * 10}], 1];
Print[ListPlot[residuals, PlotRange → All, AxesOrigin → {0, 0}]];

Export[" C :\ Data\ ConvRes" <> angleString <> " .pdf" , ListPlot[residuals,
  PlotRange → All, AxesOrigin → {0, 0}, AxesLabel → {" Times(s)" , " Residuals (a.u.)" }]];
```

```
Export[" C :\ Our Documents\ Eduardo" <> " \ H =" <>
    ToString[field] <> " Oe test 2 minus 1s" <> " .txt" , DataPoints, " TSV " ];
```

Appendix E

Mathematica Code for Longitudinal-Field Dependent Relaxation Rate of Magnetization

```mathematica
Clear[T, g0, g02]

T = 3

3

precision = 24;
S = 10;
s = 10;
d = SetPrecision[0.55, precision];
b = SetPrecision[1.17 * 10 ^ -3, precision];
d = SetPrecision[d, precision];
a = 0.000015 * 0;
c = -2.9 * 10 ^ (-5);
c = SetPrecision[c, precision];
e = 0.046;
e = SetPrecision[e, precision];
theta = 90 / 180 * Pi;
theta = SetPrecision[theta, precision];
phi = 90 / 180 * Pi;
phi = SetPrecision[phi, precision];
g = 2;
Mb = 5.788 * 10 ^ (-9);

Kb = 8.617 * 10 ^ (-5);
hbar = 6.582 * 10 ^ (-16);
T2 = 0.55 * 10 ^ -10;

H1 = 1.3 / Sqrt[T2 / 0.85 / 10 ^ -10];

ν = 117.566;

pht = (H1 ^ 2 * g ^ 2 * Mb ^ 2 * T2) / (2 * hbar ^ 2)

p = 1.92 * 10 ^ (3);

Cs = 1400;

ph1 = (g0 ^ 2 * (1.602 * 10 ^ (-19)) * Kb ^ 5) / (48 * Pi * p * Cs ^ 5 * hbar ^ 4);

ph2 = (g02 ^ 2 * (1.602 * 10 ^ (-19)) * Kb ^ 5) / (32 * Pi * p * Cs ^ 5 * hbar ^ 4);
Msat = 1192 / 10 ^ 4;
Aloop = 60 * 200 * (10 ^ -6) ^ 2;
g0 = 2.60;
g02 = 0;


Deltafunc[i_, j_] := If[i == j , 1, 0];

Sz = Table[i * Deltafunc[i, j ], {i, -s, s}, {j , -s, s}];

Sx = 1 / 2 * Table[Sqrt[(s - i) * (s + i + 1)] * Deltafunc[j , i + 1] +

    Sqrt[(s + i) * (s - i + 1)] * Deltafunc[j , i - 1], {i, -s, s}, {j , -s, s}];

Sy = 1 / (2 i ) * Table[Sqrt[(s - i) * (s + i + 1)] * Deltafunc[j , i + 1] -

    Sqrt[(s + i) * (s - i + 1)] * Deltafunc[j , i - 1], {i, -s, s}, {j , -s, s}];
Splus = Sx + I * Sy;
Sminus = Sx - I * Sy;
Splusz = Splus.Sz ;
```

```
Szplus = Sz .Splus;
Sminusz = Sminus.Sz ;
Szminus = Sz .Sminus;
Splus2 = Splus.Splus;
Sminus2 = Sminus.Sminus;
Sn = (Sz * Cos[theta] + Sx * Sin[theta] * Cos[phi] + Sy * Sin[theta] * Sin[phi]);

cmatrix = MatrixPower[Sx + I * Sy, 4] + MatrixPower[Sx - I * Sy, 4];
ematrix = MatrixPower[Sx, 2] - MatrixPower[Sy, 2];
```

22 216.6

```
Hmin = 1000;

Hmax = 10 000;

Hstep = 400;

HzMin = 4000;

HzMax = 5500;

HzStep = 20;

Timing[

 Do[

  H0[Hz_] := SetPrecision[-d * Sz ^2 - b * Sz ^4 - g * (Mb/Kb) * Hz * Sz -

     g * (Mb/Kb) * Sin[theta] * H * (Sx * Cos[phi] + Sy * Sin[phi]), precision];
egsyst = Transpose[Table[Eigensystem[H0[Hz ]], {Hz , HzMin, HzMax, HzStep}]];
Do[Evalue[Hz , i] = Chop[egsyst[[1, (Hz - HzMin)/HzStep + 1, i]]],
   {Hz , HzMin, HzMax, HzStep}, {i, 1, 2 * s + 1}];
Do[Estate[Hz , i] = Chop[egsyst[[2, (Hz - HzMin)/HzStep + 1, i]]],
   {Hz , HzMin, HzMax, HzStep}, {i, 1, 2 * s + 1}];
Do[

    Sxelement[Hz , i, k ] = Abs[(Conjugate[Estate[Hz , i]].Sx.Estate[Hz , k ])]^2;

    S1element[Hz , i, k ] = Abs[(Conjugate[Estate[Hz , i]].(Splusz + Szplus).Estate[Hz , k ])]^

      2 + Abs[(Conjugate[Estate[Hz , i]].(Sminusz + Szminus).Estate[Hz , k ])]^2;

    S2element[Hz , i, k ] = Abs[(Conjugate[Estate[Hz , i]].Sminus2.Estate[Hz , k ])]^2 +

     Abs[(Conjugate[Estate[Hz , i]].Splus2.Estate[Hz , k ])]^2;

   Boltz [Hz , i, k ] = Exp[((Evalue[Hz , k ] - Evalue[Hz , i]))/T],

   {i, 1, 2 * s + 1}, {k , 1, 2 * s + 1}, {Hz , HzMin, HzMax, HzStep}

  ];
ph2 = 0;
Do[Rate[Hz ] = SetPrecision[
```

```mathematica
    Transpose[
      Table[
        If[
          i == j ,
          Sum[
            If[k == i, 0, -(((ph1 * S1element[Hz , i, k ] * ((Evalue[Hz , k ] - Evalue[Hz , i]) ^ 3)) *
                  ((1 / (Boltz [Hz , i, k ] - 1)))) + ((ph2 * S2element[Hz , i, k ] * ((Evalue[Hz , k ] -
                      Evalue[Hz , i]) ^ 3)) * ((1 / (Boltz [Hz , i, k ] - 1)))))], {k , 1, 2 * s + 1}
          ],
          ((ph1 * S1element[Hz , i, j ] * ((Evalue[Hz , j ] - Evalue[Hz , i]) ^ 3)) *
              ((1 / (Boltz [Hz , i, j ] - 1)))) + ((ph2 * S2element[Hz , i, j ] *
                ((Evalue[Hz , j ] - Evalue[Hz , i]) ^ 3)) * ((1 / (Boltz [Hz , i, j ] - 1))))
        ]
        , {i, 1, 2 * s + 1}, {j , 1, 2 * s + 1}
      ]
    ], precision
  ], {Hz , HzMin, HzMax, HzStep}
];

  Export[" C :\ Data\ N=1 relaxation vs Hz  T=" <> ToString[T] <> "  HT=" <> ToString[H ] <>
    " .txt" , Table[{Hz , SetPrecision[Sort[Abs[Eigenvalues[Rate[Hz ]]]][[2]], precision]},
    {Hz , HzMin, HzMax, HzStep}], " TSV " ];
Relaxation = ListLogPlot[{Table[{Hz , SetPrecision[Sort[Abs[Eigenvalues[Rate[Hz ]]]][[2]],
      precision]}, {Hz , HzMin, HzMax, HzStep}]}, PlotRange → All,
    LabelStyle → Directive[FontSize → 24], AxesOrigin → {0, .001}, AxesLabel →
     {Style[" Hz   (Oe)" , FontSize → 28, Bold], Style[" Γ (1/s)" , FontSize → 28, Bold]}];
  Export[" C :\ Data\ Figures\ N=1 Mn12-tBuAc relaxation vs Hz  HT=" <>
    ToString[H ] <> "  T=" <> ToString[T] <> " .JPEG" , Relaxation, ImageSize → 500]
  , {H , Hmin, Hmax, Hstep}
 ]
]
```

{5511.39, Null }

Appendix F

Mathematica Code for Transverse-Field Dependent Relaxation Rate of Magnetization and Path Diagrams

```
<< Combinatorica`

Clear[T, g0, g02]

T = 3

3

precision = 24;
S = 10;
s = 10;
d = SetPrecision[0.55, precision];
b = SetPrecision[1.17 * 10 ^ -3, precision];
d = SetPrecision[d, precision];
a = 0.000015 * 0;
c = -2.9 * 10 ^ (-5);
c = SetPrecision[c, precision];
e = 0.046;
e = SetPrecision[e, precision];
theta = 91 / 180 * Pi;
theta = SetPrecision[theta, precision];
phi = 90 / 180 * Pi;
phi = SetPrecision[phi, precision];
g = 2;
Mb = 5.788 * 10 ^ (-9);

Kb = 8.617 * 10 ^ (-5);
hbar = 6.582 * 10 ^ (-16);
T2 = 0.55 * 10 ^ -10;

H1 = 1.3 / Sqrt[T2 / 0.85 / 10 ^ -10];

ν = 117.566;

pht = (H1 ^ 2 * g ^ 2 * Mb ^ 2 * T2) / (2 * hbar ^ 2)

p = 1.92 * 10 ^ (3);

Cs = 1400;

ph1 = (g0 ^ 2 * (1.602 * 10 ^ (-19)) * Kb ^ 5) / (48 * Pi * p * Cs ^ 5 * hbar ^ 4);

ph2 = (g02 ^ 2 * (1.602 * 10 ^ (-19)) * Kb ^ 5) / (32 * Pi * p * Cs ^ 5 * hbar ^ 4);

Msat = 1192 / 10 ^ 4;

Aloop = 60 * 200 * (10 ^ -6) ^ 2;

g0 = 2.60;

g02 = 0;


Deltafunc[i_, j_] := If[i == j, 1, 0];

Sz = Table[i * Deltafunc[i, j], {i, -s, s}, {j, -s, s}];

Sx = 1 / 2 * Table[Sqrt[(s - i) * (s + i + 1)] * Deltafunc[j, i + 1] +

    Sqrt[(s + i) * (s - i + 1)] * Deltafunc[j, i - 1], {i, -s, s}, {j, -s, s}];

Sy = 1 / (2 i) * Table[Sqrt[(s - i) * (s + i + 1)] * Deltafunc[j, i + 1] -

    Sqrt[(s + i) * (s - i + 1)] * Deltafunc[j, i - 1], {i, -s, s}, {j, -s, s}];

Splus = Sx + I * Sy;
```

```mathematica
Sminus = Sx - I * Sy;
Splusz  = Splus.Sz ;
Szplus = Sz .Splus;
Sminusz  = Sminus.Sz ;
Szminus = Sz .Sminus;
Splus2 = Splus.Splus;
Sminus2 = Sminus.Sminus;
Sn = (Sz * Cos[theta] + Sx * Sin[theta] * Cos[phi] + Sy * Sin[theta] * Sin[phi]);

cmatrix = MatrixPower[Sx + I * Sy, 4] + MatrixPower[Sx - I * Sy, 4];
ematrix = MatrixPower[Sx, 2] - MatrixPower[Sy, 2];
```

22 216.6

```mathematica
Hmin = 500;

Hmax = 20 000;

Hstep = 100;

Hz  = -5;

H0[H_] := SetPrecision[-d * Sz ^ 2 - b * Sz ^ 4 - g * (Mb / Kb) * Hz * Sz -
    g * (Mb / Kb) * Sin[theta] * H * (Sx * Cos[phi] + Sy * Sin[phi]), precision]

Timing[egsyst = Transpose[Table[Eigensystem[H0[H ]], {H , Hmin, Hmax, Hstep}]];]
```

{16.1535, Null }

```mathematica
Do[Evalue[H , i] = Chop[egsyst[[1, (H - Hmin) / Hstep + 1, i]]],
   {H , Hmin, Hmax, Hstep}, {i, 1, 2 * s + 1}];
Do[Estate[H , i] = Chop[egsyst[[2, (H - Hmin) / Hstep + 1, i]]],
   {H , Hmin, Hmax, Hstep}, {i, 1, 2 * s + 1}];
```

EIGENVALUES

```mathematica
Do[{OEval[H , i] = Sort[Table[Evalue[H , x], {x, 1, 2 s + 1}]][[2 * s + 2 - i]]},
  {H , Hmin, Hmax, Hstep}, {i, 1, 2 * s + 1}]

Do[L[i] = Table[{H , OEval[H , i]}, {H , Hmin, Hmax, Hstep}], {i, 1, 2 * s + 1}]
```

```
Timing[
 Do[
   Sxelement[H , i, k ] = Abs[(Conjugate[Estate[H , i]].Sx.Estate[H , k ])]^2;
   S1element[H , i, k ] = Abs[(Conjugate[Estate[H , i]].(Splusz + Szplus).Estate[H , k ])]^2 +
     Abs[(Conjugate[Estate[H , i]].(Sminusz + Szminus).Estate[H , k ])]^2;
   S2element[H , i, k ] = Abs[(Conjugate[Estate[H , i]].Sminus2.Estate[H , k ])]^2 +
     Abs[(Conjugate[Estate[H , i]].Splus2.Estate[H , k ])]^2;
   Boltz [H , i, k ] = Exp[((Evalue[H , k ] - Evalue[H , i])) / T],
   {i, 1, 2 * s + 1}, {k , 1, 2 * s + 1}, {H , Hmin, Hmax, Hstep}
  ];
]
```

{335.367, Null}

ph2 = 0

0

```
Timing[
 Do[Rate[H ] = SetPrecision[
    Transpose[
     Table[
      If[
       i == j ,
       Sum[
        If[k  == i, 0, -(((ph1 * S1element[H , i, k ] * ((Evalue[H , k ] - Evalue[H , i]) ^ 3)) *
                ((1 / (Boltz [H , i, k ] - 1)))) + ((ph2 * S2element[H , i, k ] * ((Evalue[H , k ] -
                  Evalue[H , i]) ^ 3)) * ((1 / (Boltz [H , i, k ] - 1)))))], {k , 1, 2 * s + 1}
        ],
        ((ph1 * S1element[H , i, j ] * ((Evalue[H , j ] - Evalue[H , i]) ^ 3)) *
           ((1 / (Boltz [H , i, j ] - 1)))) + ((ph2 * S2element[H , i, j ] *
            ((Evalue[H , j ] - Evalue[H , i]) ^ 3)) * ((1 / (Boltz [H , i, j ] - 1))))
       ]
       , {i, 1, 2 * s + 1}, {j , 1, 2 * s + 1}
      ]
     ], precision
    ], {H , Hmin, Hmax, Hstep}
   ]
 ]
{5.49217, Null }
```

Rates

```
RelaxationPlot =
 ListLogPlot[{Table[{H , SetPrecision[Sort[Abs[Eigenvalues[Rate[H ]]]][[2]], precision]},
    {H , Hmin, Hmax, Hstep}]}, PlotRange → {{0, Hmax}, All},
  LabelStyle → Directive[FontSize → 24], AxesOrigin → {0, .001},
  AxesLabel → {Style[" HT  (Oe)" , FontSize → 28, Bold], Style[" Γ  (1/s)" , FontSize → 28, Bold]}]
```
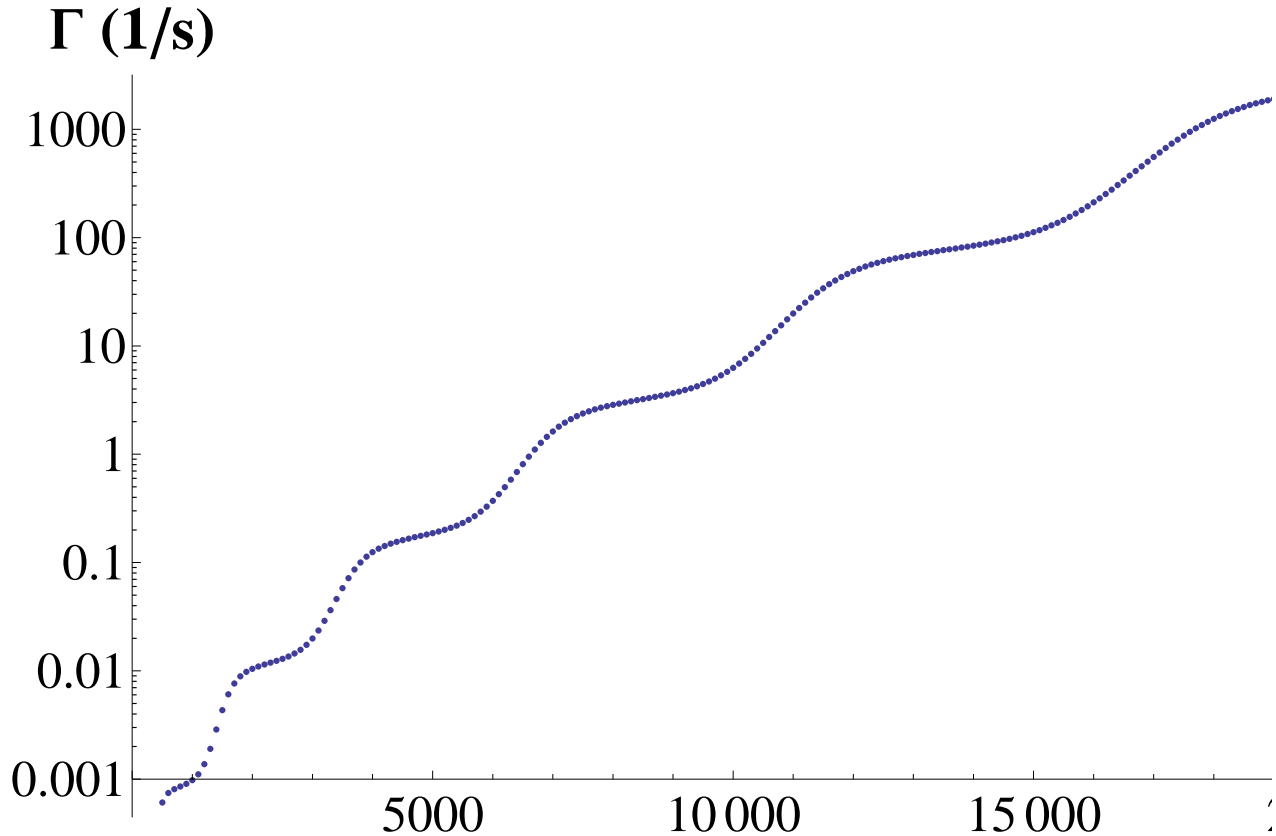


```
Export[" /home/class08/edasilvaneto08/Relaxation vs HT T=" <> ToString[T] <>
   " Hz =" <> ToString[Hz ] <> " .tiff" , RelaxationPlot, ImageSize → 50];

Export[" /home/class08/edasilvaneto08/relaxation vs HT T=" <>
   ToString[T] <> " Hz =" <> ToString[Hz ] <> " .txt" ,
  Table[{H , SetPrecision[Sort[Abs[Eigenvalues[Rate[H ]]]][[2]], precision]},
   {H , Hmin, Hmax, Hstep}], " TSV " ];
```

SUPER RUN

```
Timing[
 Do[
```

```mathematica
tmax = (1 / SetPrecision[Sort[Abs[Eigenvalues[Rate[H ]]]][[2]], precision]) * 15;
Alleqns = Rate[H ].{p1[t], p2[t], p3[t], p4[t], p5[t], p6[t], p7[t], p8[t], p9[t], p10[t],
    p11[t], p12[t], p13[t], p14[t], p15[t], p16[t], p17[t], p18[t], p19[t], p20[t], p21[t]};
eqs = {p1'[t] == Part[Alleqns, 1], p2'[t] == Part[Alleqns, 2], p3'[t] == Part[Alleqns, 3],
    p4'[t] == Part[Alleqns, 4], p5'[t] == Part[Alleqns, 5], p6'[t] == Part[Alleqns, 6],
    p7'[t] == Part[Alleqns, 7], p8'[t] == Part[Alleqns, 8], p9'[t] == Part[Alleqns, 9],
    p10'[t] == Part[Alleqns, 10], p11'[t] == Part[Alleqns, 11], p12'[t] == Part[Alleqns, 12],
    p13'[t] == Part[Alleqns, 13], p14'[t] == Part[Alleqns, 14], p15'[t] == Part[Alleqns, 15],
    p16'[t] == Part[Alleqns, 16], p17'[t] == Part[Alleqns, 17], p18'[t] == Part[Alleqns, 18],
    p19'[t] == Part[Alleqns, 19], p20'[t] == Part[Alleqns, 20], p21'[t] == Part[Alleqns, 21],
    p1[0] == 0, p2[0] == 1, p3[0] == 0, p4[0] == 0, p5[0] == 0, p6[0] == 0, p7[0] == 0,
    p8[0] == 0, p9[0] == 0, p10[0] == 0, p11[0] == 0, p12[0] == 0, p13[0] == 0, p14[0] == 0,
    p15[0] == 0, p16[0] == 0, p17[0] == 0, p18[0] == 0, p19[0] == 0, p20[0] == 0, p21[0] == 0};
sol = NDSolve[eqs, {p1, p2, p3, p4, p5, p6, p7, p8, p9, p10, p11, p12, p13, p14, p15, p16, p17,
    p18, p19, p20, p21}, {t, 0, tmax}, MaxSteps → 100 000, WorkingPrecision → precision];
Magnetization[T, t_] = (((Conjugate[Estate[H , 1]].Sz .Estate[H , 1]) * p1[t]) +
    ((Conjugate[Estate[H , 2]].Sz .Estate[H , 2]) * p2[t]) +
    ((Conjugate[Estate[H , 3]].Sz .Estate[H , 3]) * p3[t]) +
    ((Conjugate[Estate[H , 4]].Sz .Estate[H , 4]) * p4[t]) +
    ((Conjugate[Estate[H , 5]].Sz .Estate[H , 5]) * p5[t]) +
    ((Conjugate[Estate[H , 6]].Sz .Estate[H , 6]) * p6[t]) +
    ((Conjugate[Estate[H , 7]].Sz .Estate[H , 7]) * p7[t]) +
    ((Conjugate[Estate[H , 8]].Sz .Estate[H , 8]) * p8[t]) +
    ((Conjugate[Estate[H , 9]].Sz .Estate[H , 9]) * p9[t]) +
    ((Conjugate[Estate[H , 10]].Sz .Estate[H , 10]) * p10[t]) +
    ((Conjugate[Estate[H , 11]].Sz .Estate[H , 11]) * p11[t]) +
    ((Conjugate[Estate[H , 12]].Sz .Estate[H , 12]) * p12[t]) +
    ((Conjugate[Estate[H , 13]].Sz .Estate[H , 13]) * p13[t]) +
    ((Conjugate[Estate[H , 14]].Sz .Estate[H , 14]) * p14[t]) +
    ((Conjugate[Estate[H , 15]].Sz .Estate[H , 15]) * p15[t]) +
    ((Conjugate[Estate[H , 16]].Sz .Estate[H , 16]) * p16[t]) +
    ((Conjugate[Estate[H , 17]].Sz .Estate[H , 17]) * p17[t]) +
```

```
    ((Conjugate[Estate[H , 18]].Sz .Estate[H , 18]) *p18[t]) +

    ((Conjugate[Estate[H , 19]].Sz .Estate[H , 19]) *p19[t]) +

    ((Conjugate[Estate[H , 20]].Sz .Estate[H , 20]) *p20[t]) +

    ((Conjugate[Estate[H , 21]].Sz .Estate[H , 21]) *p21[t])) /. sol;

DMagnetization[T, t_] = (((Conjugate[Estate[H , 1]].Sz .Estate[H , 1]) *p1'[t]) +

    ((Conjugate[Estate[H , 2]].Sz .Estate[H , 2]) *p2'[t]) +

    ((Conjugate[Estate[H , 3]].Sz .Estate[H , 3]) *p3'[t]) +

    ((Conjugate[Estate[H , 4]].Sz .Estate[H , 4]) *p4'[t]) +

    ((Conjugate[Estate[H , 5]].Sz .Estate[H , 5]) *p5'[t]) +

    ((Conjugate[Estate[H , 6]].Sz .Estate[H , 6]) *p6'[t]) +

    ((Conjugate[Estate[H , 7]].Sz .Estate[H , 7]) *p7'[t]) +

    ((Conjugate[Estate[H , 8]].Sz .Estate[H , 8]) *p8'[t]) +

    ((Conjugate[Estate[H , 9]].Sz .Estate[H , 9]) *p9'[t]) +

    ((Conjugate[Estate[H , 10]].Sz .Estate[H , 10]) *p10'[t]) +

    ((Conjugate[Estate[H , 11]].Sz .Estate[H , 11]) *p11'[t]) +

    ((Conjugate[Estate[H , 12]].Sz .Estate[H , 12]) *p12'[t]) +

    ((Conjugate[Estate[H , 13]].Sz .Estate[H , 13]) *p13'[t]) +

    ((Conjugate[Estate[H , 14]].Sz .Estate[H , 14]) *p14'[t]) +

    ((Conjugate[Estate[H , 15]].Sz .Estate[H , 15]) *p15'[t]) +

    ((Conjugate[Estate[H , 16]].Sz .Estate[H , 16]) *p16'[t]) +

    ((Conjugate[Estate[H , 17]].Sz .Estate[H , 17]) *p17'[t]) +

    ((Conjugate[Estate[H , 18]].Sz .Estate[H , 18]) *p18'[t]) +

    ((Conjugate[Estate[H , 19]].Sz .Estate[H , 19]) *p19'[t]) +

    ((Conjugate[Estate[H , 20]].Sz .Estate[H , 20]) *p20'[t]) +

    ((Conjugate[Estate[H , 21]].Sz .Estate[H , 21]) *p21'[t])) /. sol;
pop[1, t_] = Part[p1[t] /. sol, 1];
pop[2, t_] = Part[p2[t] /. sol, 1];
pop[3, t_] = Part[p3[t] /. sol, 1];
pop[4, t_] = Part[p4[t] /. sol, 1];
pop[5, t_] = Part[p5[t] /. sol, 1];
pop[6, t_] = Part[p6[t] /. sol, 1];
pop[7, t_] = Part[p7[t] /. sol, 1];
```

```
pop[8, t_] = Part[p8[t] /. sol, 1];
pop[9, t_] = Part[p9[t] /. sol, 1];
pop[10, t_] = Part[p10[t] /. sol, 1];
pop[11, t_] = Part[p11[t] /. sol, 1];
pop[12, t_] = Part[p12[t] /. sol, 1];
pop[13, t_] = Part[p13[t] /. sol, 1];
pop[14, t_] = Part[p14[t] /. sol, 1];
pop[15, t_] = Part[p15[t] /. sol, 1];
pop[16, t_] = Part[p16[t] /. sol, 1];
pop[17, t_] = Part[p17[t] /. sol, 1];
pop[18, t_] = Part[p18[t] /. sol, 1];
pop[19, t_] = Part[p19[t] /. sol, 1];
pop[20, t_] = Part[p20[t] /. sol, 1];
pop[21, t_] = Part[p21[t] /. sol, 1];
Do[
 JC [i, j , t_] = SetPrecision[(pop[i, t]) * Part[Rate[H ], j , i] -
     (pop[j , t]) * Part[Rate[H ], i, j], (precision + 8)], {i, 1, (2 * s) + 1}, {j , 1, (2 * s) + 1}
 ];

 number = FindRoot[Magnetization[T, t] - (s / Exp[1]), {t, 0.0000007}];
 upperBound = 7 * number[[1]][[2]];
 CurrentMatrix = SetPrecision[
   Table[
    -JC [i, j , upperBound] / DMagnetization[T, upperBound]
    , {i, 1, 2 * s + 1}, {j , 1, 2 * s + 1}
    ], (precision + 10)
   ];
 Do[If[
   Conjugate[Estate[H , i]].Sz .Estate[H , i] ≥ 0.2,
   Elevel[i] =
    Show[
     {
      Plot[Re[Conjugate[Estate[H , i]].H0[H ].Estate[H , i]], {x, -4, -2}],
      Graphics[
       Text[
        Style[
         SetPrecision[Conjugate[Estate[H , i]].Sz .Estate[H , i], 3], FontSize → 12, Bold],
         {-6, Re[Conjugate[Estate[H , i]].H0[H ].Estate[H , i]]}
        ]
       ]
```

```
        }
      ];
    , Null];
  If[Conjugate[Estate[H , i]].Sz .Estate[H , i] ≤ -0.2,
    Elevel[i] =
      Show[
        {
          Plot[Re[Conjugate[Estate[H , i]].H0[H ].Estate[H , i]], {x, 2, 4}],
          Graphics[
            Text[
              Style[
                SetPrecision[Conjugate[Estate[H , i]].Sz .Estate[H , i], 3], FontSize → 12, Bold],
              {6, Re[Conjugate[Estate[H , i]].H0[H ].Estate[H , i]]}
              ]
            ]
          }
        ];
    , Null];
  If[0.2 ≥ Conjugate[Estate[H , i]].Sz .Estate[H , i] ≥ -0.2,
    Elevel[i] =
      Show[
        {
          Plot[Re[Conjugate[Estate[H , i]].H0[H ].Estate[H , i]], {x, -1, 1}],
          Graphics[
            Text[
              Style[
                SetPrecision[Conjugate[Estate[H , i]].Sz .Estate[H , i], 3], FontSize → 12, Bold],
              {6, Re[Conjugate[Estate[H , i]].H0[H ].Estate[H , i]]}
              ]
            ]
          }
        ];
    , Null],
  {i, 1, 2 * s + 1}
  ];
```

```mathematica
MinCurrent = 0.0025;

MaxCurrent = 0.055;

k  = 1;

L1 = {};

L2 = {};

MinSz  = 0;

MaxSz  = 0;

TopIndex = 0;

Do[

 If[

  Part[CurrentMatrix, i, j , 1] ≥  MinCurrent,

  {

   f[Conjugate[Estate[H , i]].Sz .Estate[H , i]] = i;

   f[Conjugate[Estate[H , j ]].Sz .Estate[H , j ]] = j ;

   If[Conjugate[Estate[H , i]].Sz .Estate[H , i] > 0 &&

     Conjugate[Estate[H , j ]].Sz .Estate[H , j ] < 0,

    {

     If[Conjugate[Estate[H , i]].Sz .Estate[H , i] > MaxSz ,

      {

       MaxSz  = Conjugate[Estate[H , i]].Sz .Estate[H , i];

      }

      , Null];

     If[Conjugate[Estate[H , j ]].Sz .Estate[H , j ] < MinSz ,

      {

       MinSz  = Conjugate[Estate[H , j ]].Sz .Estate[H , j ];

      }

      , Null];

    },

    Null

   ];

   If[MemberQ[L2, i],

    Null,

    {If[Conjugate[Estate[H , i]].Sz .Estate[H , i] ≤ MaxSz  &&

       Conjugate[Estate[H , i]].Sz .Estate[H , i] > 0,

      {

       L2 = Append[L2, i];

       L1 = Append[L1, Conjugate[Estate[H , i]].Sz .Estate[H , i]];
```

```
        }
       ];
     }
   ];
   If[MemberQ[L2, j],
    Null,
    {If[Conjugate[Estate[H , j]].Sz .Estate[H , j] ≥ MinSz &&
        Conjugate[Estate[H , j]].Sz .Estate[H , j] < 0,
       {
        L2 = Append[L2, j];
        L1 = Append[L1, Conjugate[Estate[H , j]].Sz .Estate[H , j]];
       }
      ];
    }
   ];
   If[Conjugate[Estate[H , i]].Sz .Estate[H , i] ≥ 0.2,
    x1 = -4 + (k / 15),
    If[Conjugate[Estate[H , i]].Sz .Estate[H , i] ≤ -0.2,
      x1 = 4 - ((k + 1) / 15),
      {
       x1 = (-1)^TopIndex ((TopIndex) / 15);
       TopIndex = TopIndex + 1;
      }
     ];
   ];
   If[Conjugate[Estate[H , j]].Sz .Estate[H , j] ≥ 0.2,
    x2 = -4 + ((k + 1) / 15),
    If[Conjugate[Estate[H , j]].Sz .Estate[H , j] ≤ -0.2,
      x2 = 4 - ((k ) / 15),
      {
       x2 = (-1)^TopIndex ((TopIndex) / 15);
       TopIndex = TopIndex + 1;
      }
     ];
```

```mathematica
      ];
      DrawArrow[i, j] = True;
      CurrentArrow[k] =
       Graphics[{Thick , Dashed, Hue[Log[Part[CurrentMatrix, i, j , 1] / (MinCurrent - 0.001)] /
            Log[MaxCurrent / (MinCurrent - 0.001)]],
          {Arrowheads → Large, Arrow[{{x1, Re[Conjugate[Estate[H , i]].H0[H ].Estate[H , i]]},
             {x2, Re[Conjugate[Estate[H , j ]].H0[H ].Estate[H , j ]]}}]}}];

      maxIndex = k ;
      k ++
     }
     , DrawArrow[i, j] = False;
    ]
    , {i, 1, 2 * s + 1}, {j , 1, 2 * s + 1}
   ];

L1 = Sort[L1, Greater];
SuperL = {};
  LTemp = {};
For[k  = 2, k  ≤ Length[L1], k ++,
   {
     LTemp = KSubsets[L1, k ];
     For[n = 1, n ≤ Length[LTemp], n++,
      If[
       MemberQ[Part[LTemp, n], Part[L1, 1]] && MemberQ[Part[LTemp, n], Part[L1, Length[L1]]],
        SuperL = Append[SuperL, Part[LTemp, n]];
        , Null]
     ];
    }
   ];
SuperL2 = {};
  For[k  = 1, k  ≤ Length[SuperL], k ++,
    {
     LTemp = Part[SuperL, k ];
     LTemp2 = {};
     For[n = 1, n ≤ Length[LTemp], n++,
      LTemp2 = Append[LTemp2, f[Part[LTemp, n]]]
     ];
```

```
      SuperL2 = Append[SuperL2, LTemp2]
     }
   ];
For[n = 1, n ≤ Length[L2], n++,
    {
      Normalization[Part[L2, n]] = 0;
      For[k = 1, k ≤ 2 * s + 1, k ++,
       {
         If[Part[CurrentMatrix, Part[L2, n], k , 1] > 0,
           Normalization[Part[L2, n]] =
            Normalization[Part[L2, n]] + Part[CurrentMatrix, Part[L2, n], k , 1]
         ];
       }
      ]
    }
   ];
For[k = 1, k ≤ Length[SuperL2], k ++,
    {
      ProdCurrent[k ] = 1;
      LTemp = Part[SuperL2, k ];
      For[n = 1, n < Length[LTemp], n++,
       {
         ProdCurrent[k ] =

            ProdCurrent[k ] *  Part [CurrentMatrix, Part [LTemp, n], Part [LTemp, n + 1], 1]
                               ─────────────────────────────────────────────────────────
                                           Normalization[Part [LTemp, n]]
       }
      ];
    }
   ];
For[k = 1, k ≤ Length[SuperL2], k ++,
    {If[ProdCurrent[k ] == Max[Table[ProdCurrent[k ], {k , 1, Length[SuperL2]}]],
      MostProbIndex = k , Null]
    }
   ];
```

```
MostProbPath[H ] = Part[SuperL2, MostProbIndex];

  MostProbPathSz [H ] = Table[Conjugate[Estate[H , Part[MostProbPath[H ], i]]].
      Sz .Estate[H , Part[MostProbPath[H ], i]], {i, 1, Length[MostProbPath[H ]]}];
BarrierTop[H ] = Max[Table[Re[Conjugate[Estate[H , Part[MostProbPath[H ], i]]].H0[H ].
      Estate[H , Part[MostProbPath[H ], i]]], {i, 1, Length[MostProbPath[H ]]}]];
  LowestTransitionLevel[H ] = Min[Table[Re[Conjugate[Estate[H , Part[MostProbPath[H ], i]]].
      H0[H ].Estate[H , Part[MostProbPath[H ], i]]], {i, 1, Length[MostProbPath[H ]]}]];
BarrierHeight[H ] = BarrierTop[H ] - Re[Conjugate[Estate[H , 1]].H0[H ].Estate[H , 1]];
ScaleFactor = 400;
  Legend = Show[Table[Graphics[{Thickness[.09],
      Hue[Log[x / (MinCurrent - 0.001)] / Log[MaxCurrent / (MinCurrent - 0.001)]],
      Line[{{8, -70 + ScaleFactor * x}, {8.5, -70 + ScaleFactor * x}}]]}],
    {x, MinCurrent, MaxCurrent, (MaxCurrent - MinCurrent) / 10}]];
  For[n = 1, n ≤ Length[MostProbPath[H ]], n++,
   {i = Part[MostProbPath[H ], n];
    If[
     Conjugate[Estate[H , i]].Sz .Estate[H , i] ≥ 0.2,
     MostProbCircle[n] = Graphics[{Red, Thick , Dashed,
        Circle[{-5, Re[Conjugate[Estate[H , i]].H0[H ].Estate[H , i]]}, 2]}];
     , Null];
    If[Conjugate[Estate[H , i]].Sz .Estate[H , i] ≤ -0.2,
     MostProbCircle[n] = Graphics[{Red, Thick , Dashed,
        Circle[{5, Re[Conjugate[Estate[H , i]].H0[H ].Estate[H , i]]}, 2]}];
     , Null];
    If[0.2 ≥ Conjugate[Estate[H , i]].Sz .Estate[H , i] ≥ -0.2,
     MostProbCircle[n] = Graphics[{Red, Thick , Dashed,
        Circle[{0, Re[Conjugate[Estate[H , i]].H0[H ].Estate[H , i]]}, 2]}];
     , Null]
   }
  ];
  CircIndex2 = 0;
  For[n = 1, n ≤ 2 s + 1, n++,
   {
    If[Conjugate[Estate[H , n]].Sz .Estate[H , n] > MaxSz ,
```

```mathematica
    CircIndex2 = CircIndex2 + 1;

    MostProbCircle2[CircIndex2] = Graphics[{Red, Thick , Dashed,
      Circle[{-5, Re[Conjugate[Estate[H , n]].H0[H ].Estate[H , n]]}, 2]}];
    , Null];
   If[Conjugate[Estate[H , n]].Sz .Estate[H , n] < MinSz ,
    CircIndex2 = CircIndex2 + 1;

    MostProbCircle2[CircIndex2] = Graphics[{Red, Thick , Dashed,
      Circle[{5, Re[Conjugate[Estate[H , n]].H0[H ].Estate[H , n]]}, 2]}];
    , Null];
  }
  ];

 Circles = Show[Table[MostProbCircle[n], {n, 1, Length[MostProbPath[H ]]}]];

 Circles2 = Show[Table[MostProbCircle2[n], {n, 1, CircIndex2}]];

 CurrentDiagram[H ] =
  Show[
   {
    Circles2, Circles, Legend, Table[CurrentArrow[k ], {k , 1, maxIndex}],

    Show[Table[{Elevel[i]}, {i, 1, 2*s + 1}], PlotRange → All]
   },
   Axes → {False, True}, AspectRatio → 1.5,
   PlotLabel → Style[H , Large, Bold], PlotRange → {-70, 5}
  ];

 Export[" /home/class08/edasilvaneto08/Figures/Mn12-tBuAc Current Diagam T=3 Hz =" <>

   ToString[Hz ] <> "  HT=" <> ToString[H ] <> " .JPEG" , CurrentDiagram[H ], ImageSize → 500];

 , {H , Hmin, Hmax, Hstep}
 ]
 ]

ListPlot[{Table[{H , BarrierHeight[H ]}, {H , Hmin, Hmax, Hstep}]}, PlotRange → All]
```
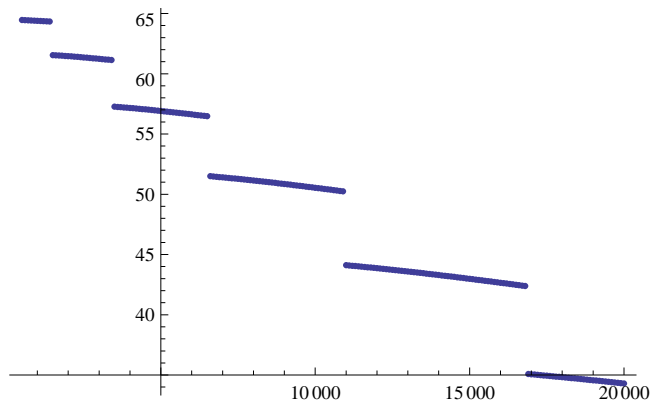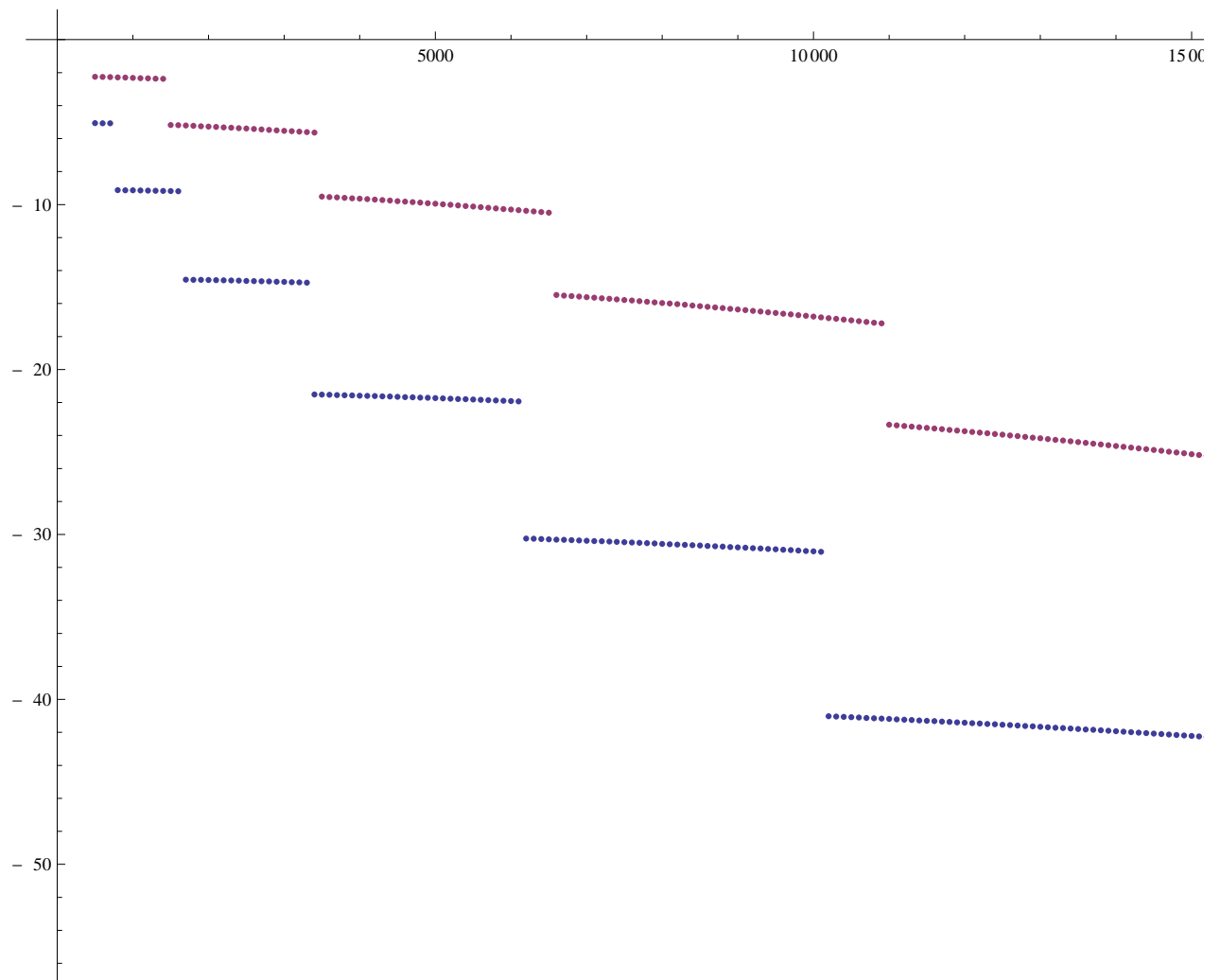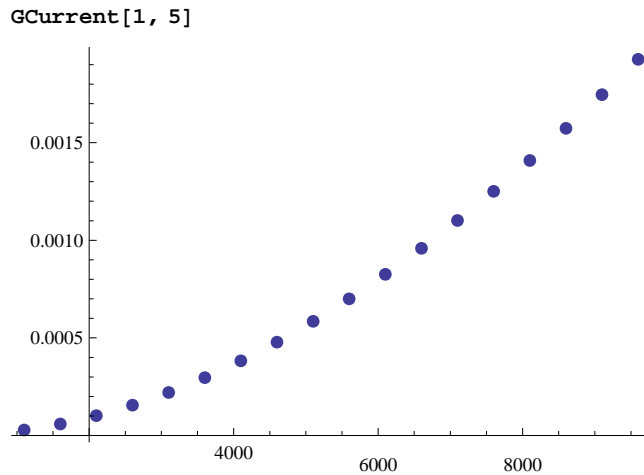
```
ListPlot[{Table[{H , LowestTransitionLevel[H ]}, {H , Hmin, Hmax, Hstep}],
  Table[{H , BarrierTop[H ]}, {H , Hmin, Hmax, Hstep}]}]
```


ALL GRAPHS

```
Do[GCurrent[i, j ] =
  ListPlot[Table[{H , Part[CurrentMatrix[H ], i, j , 1]}, {H , Hmin, Hmax, Hstep}],
    PlotStyle → PointSize[.02], PlotRange → All]
 , {H , Hmin, Hmax, Hstep}, {i, 1, 2 * s + 1}, {j , 1, 2 * s + 1}]
```

GCurrent[1, 5]


```
Do[Print[{i, j }];
 Print[GCurrent[i, j]],
 {i, 1, 2 * s + 1}, {j , 1, 2 * s + 1}
]
```

Make Video

```
Timing[
  Export[" /home/class08/edasilvaneto08/Videos/Current Diagams Hz =" <>
    ToString[Hz ] <> "  T=" <> ToString[T] <> " .avi" ,
   Table[CurrentDiagram[H ] , {H , Hmin, Hmax, Hstep}], ImageSize → 500, " FrameRate" → 2]
 ];

Do[HClassical[H , x_] = -d * (s * Cos[x]) ^ 2 - b * (s * Cos[x]) ^ 4 -
    g * (Mb / Kb) * (Hz  * s * Cos[x] * Cos[phi] + H  * s * Sin[x] * Sin[phi]), {H , Hmin, Hmax, Hstep}];

Do[ClassicalBarrier[H ] = Part[FindMaximum[HClassical[H , x], {x, Pi / 2}], 1] -
    Part[FindMinimum[HClassical[H , x], {x, 0}], 1], {H , Hmin, Hmax, Hstep}];

ListPlot[{Table[{H , BarrierHeight[H ]}, {H , Hmin, Hmax, Hstep}],
  Table[{H , ClassicalBarrier[H ]}, {H , Hmin, Hmax, Hstep}]}, PlotRange → All]
```

```
Export[" /home/class08/edasilvaneto08/Barrier Height T=" <> ToString[T] <> "  Hz =" <>
    ToString[Hz ] <> " .txt" , Table[{H , BarrierHeight[H ]}, {H , Hmin, Hmax, Hstep}], " TSV " ];
Export[" /home/class08/edasilvaneto08/Classical Barrier Height T=" <>
    ToString[T] <> "  Hz =" <> ToString[Hz ] <> " .txt" ,
  Table[{H , ClassicalBarrier[H ]}, {H , Hmin, Hmax, Hstep}], " TSV " ];
```

Bibliography

[1] K. Blum, *Density Matrix Theory and Applications* Physics of Atoms and Molecules, 2nd ed. (Plenum Press, New York, 1996).

[2] J. R. Friedman and H. Siyuan, editors, *Exploring the Quantum/Classical Frontier: Recent Advances in Macroscopic Quantum Phenomena* (Nova Science Publishers, 2003).

[3] S. Hill *et al.*, Polyhedron **24**, 2284 (2005).

[4] W. Wernsdorfer, M. Murugesu, and G. Christou, Phys. Rev. B **96** (2006).

[5] T. Lis, Acta Crystallogr. B **36**, 2042 (1980).

[6] I. Mirebeau *et al.*, Phys. Rev. Lett. **83**, 628 (1999).

[7] A. L. Barra, D. Gatteschi, and R. Sessoli, Phys. Rev. B **56**, 8192 (1997).

[8] J. Friedman, M. Sarachik, J. Tejada, and R. Ziolo, Phys. Rev. Lett. **76**, 3830 (1996).

[9] J. M. Hernandez *et al.*, Phys. Rev. B **55**, 5858 (1997).

[10] K. M. Mertes, *Distributions of Tunnel Splittings in Quantum Tunneling of Magnetization in the Single Molecule Magnet, Mn12-acetate*, PhD thesis, City College of the City University of New York, 2002.

[11] K. M. Mertes *et al.*, Phys. Rev. Lett. **87**, 227205 (2001).

[12] E. M. Chudnovsky and D. A. Garanin, Phys. Rev. Lett. **87** (2001).

[13] A. Cornia *et al.*, Phys. Rev. Lett. **89** (2002).

[14] I. Chiorescu, R. Giraud, A. G. M. Jansen, A. Caneschi, and B. Barbara, Phys. Rev. Lett. **85**, 4807 (2000).

[15] J. R. Friedman, *Resonant Magnetization Tunneling in High-Spin Molecules*, PhD thesis, City University of New York , 1996.

[16] J. R. Friedman, Phys. Rev. B **57**, 10291 (1998).

[17] D. A. Garanin and E. M. Chudnovsky, Phys. Rev. B **56**, 11102 (1997).

[18] E. M. Chudnovsky and D. A. Garanin, Phys. Rev. Lett. **79**, 4469 (1997).

[19] M. Foss-Feig, *Ground State Tunnel Splitting in Mn12 Acetate* (Senior Thesis, Amherst College, 2006).

[20] E. M. Chudnovsky and J. Tejada, *Macroscopic Quantum Tunneling of the Magnetic Moment* Cambridge Studies in Magnetism (Cambridge University Press, 1998).

[21] D. A. Garanin, J. Phys. A **64** (1991).

[22] E. M. Chudnovsky and J. Tejada, *Lectures on Magnetism* (Rinton Press, 2006).

[23] M. N. Leuenberger and D. Loss, Phys. Rev. B **61**, 1286 (2000).

[24] M. N. Leuenberger and D. Loss, Europhysics Letters **46**, 692 (1999).

[25] R. P. Feynman, *Statistical Mechanics* (Westview Press, 1972).

[26] E. M. Chudnovsky and D. A. Garanin, Europhysics Letters **52**, 245 (2000).

[27] M. N. Leuenberger and D. Loss, Europhysics Letters **52**, 247 (2000).

[28] M. Bal *et al.*, Europhysics Letters **82** (2008).

[29] J. Villain, F. Hartman-Boutron, R. Sessoli, and A. Rettori, Europhysics Letters **27(2)**, 159 (1994).

[30] A. Abragam and B. Bleaney, *Electron Paramagnetic Resonance of Transition Ions* (Dover, 1970).